Dissertation
submitted to the
Combined Faculties of the Natural Sciences and Mathematics
of the Ruperto-Carola-University of Heidelberg, Germany
for the degree of
Doctor of Natural Sciences

Put forward by

M. Sc. Daniil Gelfand
born in: Gomel
Oral examination: 22.07.2014

Lattice Theory
of Nonequilibrium
Fermion Production

Referees:	**Prof. Dr. Jürgen Berges** **Prof. Dr. Luca Amendola**

Zusammenfassung

In dieser Arbeit untersuchen wir die Erzeugung fermionischer Teilchen außerhalb des Gleichgewichts mittels moderner Gittermethoden. Die vorgestellten Anwendungen reichen vom Preheating nach der kosmologischen Inflation im frühen Universum über Prä-Thermalisierungsdynamik in Schwerionenkollisionen bis hin zur Paarerzeugung und Stringbrechung in einem niedrigdimensionalen Modell der Quantenchromodynamik.

In Instabilitäten aufweisenden skalaren Modellen beobachten wir eine stark erhöhte Fermionproduktion in Anwesenheit bosonischer Überbesetzung. Als mögliche Szenarien fürs Preheating nach der Inflation untersuchen wir parametriche Resonanz und tachyonische Instabilität. Wir finden, dass sowohl die qualitativen als auch die quantitativen Eigenschaften der resultierenden Fermionverteilung weitgehend von einem effektiven Kopplungsparameter bestimmt werden.

Um Fermionen in drei räumlichen Dimensionen simulieren zu können, wenden wir einen effizienten, stochastischen Gitter-Algorithmus an, welchen wir durch einen Vergleich mit exacten Gitterrechnungen und mit auf einer Kopplungsentwicklung basierten funktionalen Methode verifizieren.

Im massiven Schwinger-Modell analysieren wir die Erzeugung von Fermion/Antifermion Paaren durch homogene und inhomogene elektrische Felder und beobachten den Aufbau von Strings zwischen den Ladungen. Nachfolgend studieren wir die Dynamik der Stringbrechung und beschreiben einen Zwei-Phasen-Prozess, welcher aus der anfänglichen Teilchenproduktion sowie der folgenden Ladungsseparation und Abschirmung besteht.

In Quantenchromodynamik liegt unser Fokus auf den Eigenschaften des Quarksektors während der turbulenten bosonischen Energiekaskade sowie auf der Isotropisierung der Quarks und Gluonen, ausgehend von unterschiedlichen Anfangsbedngungen.

Abstract

In this thesis we investigate non-equilibrium production of fermionic particles using modern lattice techniques. The presented applications range from preheating after inflation in the early Universe cosmology to pre-thermalization dynamics in heavy-ion collisions as well as pair production and string breaking in a lower-dimensional model of quantum chromodynamics.

Strong enhancement of fermion production in the presence of overoccupied bosons is observed in scalar models undergoing instabilities. Both parametric resonance and tachyonic instability are considered as scenarios for preheating after inflation. The qualitative and quantitative features of the resulting fermion distribution are found to depend largely on an effective coupling parameter.

In order to simulate fermions in three spatial dimensions we apply a stochastic low-cost lattice algorithm, which we verify by comparison with an exact lattice approach and with a functional method based on a coupling expansion.

In the massive Schwinger model, we analyse the creation of fermion/anti-fermion pairs from homogeneous and inhomogeneous electric fields and observe string formation between charges. As a follow-up we study the dynamics of string breaking and establish a two-stage process, consisting of the initial particle production followed by subsequent charge separation and screening.

In quantum chromodynamics, our focus lies on the properties of the quark sector during turbulent bosonic energy cascade as well as on the isotropization of quarks and gluons starting from different initial conditions.

Contents

Chapter 1.

Introduction

Modern physics is a success story. On length scales ranging from billions of light years to fractions of an attometer, general theory of relativity and the Standard Model of particle physics provide an almost complete description of the laws of nature. Extraordinary experimental effort is being made to push our observational limits even further and test existing theoretical models in new and extreme regimes. Two of such front lines of modern physics have enjoyed a rising attention during the last years, from theoreticians and experimentalists alike. These are on the one hand the investigations of strongly interacting nuclear matter and its main properties, while on the other hand it is the early history of our Universe from the Big Bang to the emission of the cosmic microwave background (CMB) radiation.

In cosmology a detailed analysis of the angular distribution of the CMB and its polarization pattern has become possible due to new satellite missions, foremost the Planck space observatory, and ground based instruments like BICEP (Background Imaging of Cosmic Extragalactic Polarization). They could be able to verify the proposed inflationary phase during the early time periods after Big Bang or even shed some light onto microscopic origins of inflation. For theoreticians, some of the major challenges lie in determining the shape of the potential for the inflaton field and establishing a connection between various epochs in the cosmological time evolution, e.g. the transition from the inflationary phase to the process of primordial nucleosynthesis.

In high-energy nuclear physics we find a rather different picture, there the focus of the scientific community has shifted towards improved understanding of macroscopic and long range properties of quantum chromodynamics (QCD), the microscopic theory of strong interactions. These properties include the confinement of colour charges and in particular the exploration of the phase diagram of QCD. Both topics are deeply interconnected, because one of the most striking features of the presumed phase diagram is the appearance of a deconfined phase. In this thermodynamic regime of high temperatures and pressures the constituents of strong interacting matter, quarks and gluon, dominate a state of matter named quark-gluon plasma (QGP). The main experimental tools employed for studies of the QCD phase diagram are the relativistic heavy-ion colliders at CERN and Brookhaven National Laboratory, LHC (Large Hadron Collider) and RHIC (Relativistic Heavy Ion Collider). In these facilities atomic nuclei are smashed into each other in order to create a hyper-dense and ultra-hot medium. From the subsequent particle shower information about the behaviour of the fireball in time and as a function of collision energy is extracted.

Remarkably, studies of cosmology after the inflationary phase and of QCD matter shortly after a heavy-ion collision have a lot in common [1, 2]. Most importantly the fact that in both situations we are considering physical systems which have been pushed into a non-equilibrium state initially. To be specific, in inflation it is the rapid expansion and in heavy-ion collisions the initial impact, which brings out of equilibrium processes into play. Another similarity is that ultimately the matter and radiation produced after inflation as well as the remnants of the QCD fireball apparently approach thermal equilibrium. In cosmology this is implied in particular by models of subsequent nucleosynthesis [3], which correctly [1] describe the abundances of chemical elements created in the early Universe. For heavy-ion collisions the thermalization is indicated by the successfully applied description of the fireball evolution by means of relativistic hydrodynamics [5], a framework assuming local thermal equilibrium. However, the path towards thermal equilibrium remains unclear for heavy-ions and inflationary cosmology alike.

If we want to make theoretical predictions for the outcome of both scenarios, then we are forced to solve the corresponding initial value problems and study their time evolution in the framework of non-equilibrium quantum field theory [6]. Originally, the development of quantum field theory was driven by the requirement to calculate cross-sections and decay rates for processes occurring in vacuum at vanishing temperature. The most prominent example is surely the perturbation theory, a coupling expansion around free field solutions. Tools designed for studying thermodynamics of quantum fields have been developed somewhat later. From the point of view of computational complexity these are already a step harder than standard vacuum techniques. Unfortunately, the methods of quantum field theory applicable to non-equilibrium situations are even more involved. Their development is still an ongoing research topic in which tremendous progress has been made during the last years.

In the course of this work we will present some of these methods, with an emphasis on real-time lattice simulations. Having contributed to the development of lattice techniques specifically designed to study time evolution of fermionic fields in out-of-equilibrium situations [7], we will concentrate on the topic of fermion production in three different applications: the post-inflationary epoch, for the early stages of heavy-ion collisions and from ultra-intense laser beams.

We proceed as follows: In the next section we will briefly describe cosmological inflation and the subsequent phase of preheating. Afterwards, a short description of dynamics and theoretical challenges in relativistic heavy-ion collisions will follow. An introduction to non-equilibrium quantum field theory and typical applications is given in Chap. 2. In Chap. 3 the relevant methods for this work applied to non-equilibrium problems

---

[1] Up to the isotope Lithium-7, the so-called Lithium problem [4].

in quantum field theory are presented. A detailed description of fermions on a real-time lattice can be found in Chap. 4. Chap. 5 consists of results obtained in scalar theories with fermions relevant for both QCD dynamics (especially Sec. 5.1) and preheating after inflation (Sec. 5.2), together with associated discussions. Fermion production in gauge theories is the topic in Chap. 6, there we will start from pair production in lower dimensional models of QCD (Sec. 6.1), proceed with a detailed study of string breaking (Sec. 6.2) and finally arrive at the topic of quark production in a non-Abelian gauge theory (Sec. 6.3). We will conclude and give a short outlook on future projects in Chap. 7.

Our results from Sec. 5.1 have been obtained in collaboration with Jürgen Berges and Dénes Sexty and already published in

J. Berges, D. Gelfand and D. Sexty, Phys. Rev. D **89** *(2014) 025001.*

Investigations done in Secs. 6.1 and 6.2 have been lead by Florian Hebenstreit. He undertook the implementation of our cooperatively developed application of fermion lattice techniques for Abelian gauge theories. The results are contained in the following publications:

F. Hebenstreit, J. Berges, and D. Gelfand, Phys. Rev. D **87** *(2013) 105006.*

F. Hebenstreit, J. Berges, and D. Gelfand, Phys. Rev. Lett. **111** *(2013) 201601.*

Forthcoming publications about the studies presented in Secs. 5.2 and 6.3 of this thesis are in progress.

1.1. Preheating after inflation

Inflation is a proposed period in the early history of our Universe after the Big Bang. It is marked by an exponential growth of distances and length scales, parametrized by the scale factor $a(t)$, such that distances at later times $d(t)$ are given by $d(t) = a(t)d_0$. This concept of an expanding geometry should be considered in the context of a Friedmann-Robertson-Walker (FRW) metric

$$ds^2 = dt^2 - a^2(t)\left[\frac{dr^2}{1 - Kr^2} + r^2 d\theta^2 + r^2 \sin^2\theta d\varphi^2\right], \tag{1.1}$$

describing a homogeneous and isotropic universe. This particular form of metric is formulated here in spherical coordinates with K parametrizing the curvature of space.

Inflation was introduced [8, 9] in order to explain some of the key cosmological observations which stood in conflict with the standard Hot Big Bang scenario. These are the high degree of spatial flatness found in our Universe as well as the homogeneity and isotropy that are observed on large scales. Inflation solves this puzzle with its faster than the speed of light growth of $a(t)$, pushing causally connected patches of space far away from each other. In this way, measuring strong similarities between spatial regions which are separated by distances larger than the age of the Universe today poses no contradiction to the principles of relativity. Additionally, inflation paradigm also delivers the seeds for subsequent structure formation, by stretching the tiny vacuum fluctuations of the inflaton field into macroscopic scales. These original vacuum fluctuations are ultimately responsible for the primordial density perturbations, which for their part created the inhomogeneities in the CMB, our so far best observational window to the early Universe [10].

One of the strengths of inflationary paradigm is its simplicity. To realize an inflationary stage in a microscopic theory one requires a classical homogeneous inflaton field $\phi(t)$ moving in a potential $V(\phi)$ in such a way that its potential energy exceeds its kinetic energy, $V \ll T$. This can be easily understood from Friedmann equations, which are the equations of motion of gravitation for the special case of the FRW metric (1.1):

$$\begin{aligned} H^2 &= \frac{8\pi}{3M_{\mathrm{Pl}}^2}\mathcal{E} - \frac{K}{a^2}\,, && (1.2)\\ \frac{\ddot{a}}{a} &= -\frac{4\pi}{3M_{\mathrm{Pl}}^2}\left(\mathcal{E}+3P\right)\,, && (1.3)\end{aligned}$$

where we introduced the Hubble parameter $H = \frac{\dot{a}}{a}$, Planck mass M_{Pl}, the energy density $\mathcal{E}$ and the pressure P. The dots will be used here and in all other parts of this thesis to signify a partial derivative w.r.t. time. These equations can be solved for a given equation of state, connecting the pressure to the energy density of a physical system. Typical equations of state are $P = \mathcal{E}/3$ for radiation and $P = 0$ for cold, non-relativistic matter. For our classical homogeneous field the energy density is the sum of kinetic and potential energies, $\frac{1}{2}\dot{\phi}^2 + V(\phi)$, while the pressure is their difference, $\frac{1}{2}\dot{\phi}^2 + V(\phi)$. Considering a case in which the potential energy dominates, we arrive at a new equation of state, $P = -\mathcal{E}$. Plugging this relation into the Friedmann equations we arrive at the inflationary solution of an exponentially increasing scale factor, $a(t) = e^{Ht}$.

How does the requirement $V \ll T$ influence the time evolution of the classical field? Or, conversely, how should a classical field behave in order to trigger inflation? The answer to these questions lies in the equation of motion for the field itself

$$\ddot{\phi} + 3H\dot{\phi} + \frac{\partial V}{\partial \phi} = 0\,. \tag{1.4}$$

Here $3H\dot{\phi}$ acts like a friction term in classical mechanics, causing the field $\phi(t)$ to roll slowly towards the minimum of its potential, keeping the kinetic energy small compared to the potential energy $V(\phi)$. From the equations presented here one can formulate formal slow-roll conditions [11], constraining the shape of the potential.

What happens when a system undergoes inflationary expansion? The contribution of the curvature to the first Friedmann equation, K/a^2, diminishes very fast, making the Hubble factor H a function of just the energy density. The latter can in general be decomposed into contributions coming from the field itself as well as the matter and the radiation components. Obviously, at the start of an inflationary period the classical field should dominate the total equation of state. But how will the mixture of energy contributions change during the expansion? The energy density of the homogeneous field has the remarkable property to stay constant, $\dot{\mathcal{E}}_\phi = 0$, because the field fills the whole spatial volume by definition. Cold non-relativistic matter, often referred to as dust, is diluted by an expanding metric. Its contribution to the energy density is inversely proportional to the total volume, $\mathcal{E}_m = a^{-3}$. For all ultra-relativistic particles, summarized under the category of radiation, the dilution is accompanied by the red-shift, resulting in an even more rapidly declining energy density $\mathcal{E}_r = a^{-4}$.

These facts mean that when the potential energy becomes smaller than the kinetic term (in other words when slow-roll conditions are violated) and the period of exponential growth terminates, the energy content of the now exponentially enlarged Universe is completely dominated by the classical inflaton field ϕ. Particles or radiation which may have been present before the inflation become absolutely negligible. Since our present Universe contains a significant amount of matter (including dark matter) and radiation a process of particle creation from the inflaton field must have taken place after the inflationary phase. The process of energy transfer from the inflaton field to massive and massless particles at the end of inflation is called reheating. The name already implies that at the end of reheating a thermally equilibrated state of matter is formed, characterized by the so-called reheating temperature. A reason for the assumption of thermalization is the success of primordial or Big Bang nucleosynthesis [3]. This theory describes the abundances of light elements starting from temperatures on the MeV scale in a framework of nuclear reactions occurring in an expanding thermal medium [12].

Contrary to older models of reheating, in which the energy transfer was handled by comparably slow perturbative decay of the inflaton field [13], modern understanding implies that first a nonperturbatively fast process lead to a rapid creation of particles [14, 15, 16, 17, 18]. Later on, scattering processes should evolve the originally nonthermal particle distribution towards thermal equilibrium. The first, nonperturbative phase of reheating, has been called preheating after inflation. It is assumed that during this early stage the inflaton field undergoes a non-equilibrium instability, with parametric resonance and tachyonic instability being the two most favoured candidates [14]. In Sec. 2.2 we will discuss the general properties of these preheating scenarios.

These instabilities are known to lead to exponential growth of inflaton occupation numbers in long wavelength modes on time scales much shorter than the asymptotic thermal equilibration time. This is followed by a turbulent phase with different universal scaling regimes for nonperturbative long wavelength modes [19] and perturbative higher momenta [20].

Conventionally, the phenomenon of preheating is described using classical approximations for the bosonic inflaton field [16]. Their validity for macroscopic occupation numbers has been verified explicitly in quantum field theory [17]. Much less is known about fermion dynamics in the nonperturbative regime of high Bose occupation numbers. Since identical fermions cannot occupy the same state, their quantum nature is highly relevant and a consistent quantum theory of fermion production after inflation is of crucial importance.

So far, preheating dynamics with fermions has been mainly investigated based on semiclassical descriptions using the Dirac equation with coupling to a homogeneous inflaton field [21]. Also backreaction of fermions onto inflaton dynamics has been included. Further inclusion of quantum corrections is complicated by a secular perturbative time evolution which becomes rapidly invalid.

In an earlier work [7], we consistently included quantum corrections to next-to-leading order (NLO) in the Yukawa coupling between the inflaton field and massless fermions in the framework of a two-particle irreducible (2PI) effective action. Even for weak couplings this turned out to change semiclassical or leading-order (LO) results so dramatically that we considered a complementary nonperturbative method for comparison. It is based on lattice simulations following the techniques of Ref. [22], which we will present here in Sec. 4.1. This method treats the fermions exactly, but the inflaton dynamics remains classical-statistical. In 3 + 1 dimensions this is computationally expensive and became feasible with the implementation of ”low-cost” fermion algorithms [23], discussed in Sec. 4.2. Remarkably, higher-order corrections turned out to leave the NLO results practically unchanged for the considered range of weak couplings. In this thesis, we will extend our investigations and present new insights into fermion production during preheating.

1.2. Thermalization and string breaking in QCD

Quantum chromodynamics is the quantum field theory of strong interaction, which is responsible for binding of quarks and gluons into hadrons and the existence of atomic nuclei. Most of the mass constituting the currently observable ”non-dark” matter in the Universe is generated by strong interactions. As a theoretical concept, QCD has been thoroughly tested in many collider experiments [24], revealing a rich spectrum of bound states including baryons and mesons. Studies of jets in deep inelastic scattering (DIS) [25] allowed the detection of the microscopic degrees of freedom in QCD, quarks and gluons. The fact that these particles are not directly detectable sheds light on one of the two most exciting properties of QCD, the confinement. It manifests itself as a linearly rising potential between colour charges, preventing any isolation of quarks or gluons from each other. The strong interaction between a pair of these particles creates a tube-formed gluonic field configuration, also known as a QCD string. The energy content of this string is proportional to its length, thus increasing the energy cost for separation of two charges proportional to their distance.

Many model calculations consider the simplified scenario of a confining potential between external colour charges. The string formation between an external static quark and an antiquark is an important manifestation of the physics of confinement in QCD. In general, in theories with dynamical fundamental charges the confining string can break because of the creation of charge-anticharge pairs which screen the static sources [26, 27, 28, 29, 30, 31]. In particular, quantum electrodynamics (QED) in one spatial dimension shares the nonperturbative phenomenon of string breaking by dynamical fermion-antifermion pair creation with strong interactions in three dimensions. In QCD, the separation of a quark/anti-quark pair beyond a critical distance ultimately leads to creation of another pair, enabling two mesonic bound states to be formed.

Our current understanding of string breaking mainly concerns static properties obtained from equilibrium lattice Monte Carlo simulations. These equilibrium calculations can be based on a Euclidean formulation, where the time variable is analytically continued to imaginary values. However, in real time this phenomenon can be a process far from equilibrium with a hierarchy of time scales, which is not amenable to a Euclidean formulation. Recently, the prospect of constructing quantum simulators for gauge theories with fermions using ultra-cold atoms in an optical lattice [32, 33, 34] boosted the interest in the real-time dynamics of string breaking. First computations in this context concentrate on quantum link models [32, 35] and it is an important task to extend these investigations to QED and QCD.

The other exciting property of QCD is the asymptotic freedom [36]. By this we mean the weakening of the gauge coupling of QCD at short distances and high energies. A consequence of asymptotic freedom is that at high energies and momenta (usually several GeV) one can use perturbation theory for QCD calculations. On the other hand, long range and low energy effects like confinement naturally require non-perturbative treatment.

For the thermal behaviour of strongly interacting matter, asymptotic freedom implies that at high temperatures quarks and gluons are liberated from their hadronic bound states. Above this deconfinement phase transition, a new state of matter is formed, the quark-gluon plasma. Theoretically, the deconfinement transition at vanishing chemical potential has been calculated to be a cross-over and to occur in the region of $T = 150 - 160 MeV$ by several groups [37]. This was done by applying Euclidean lattice Monte-Carlo simulations, an ab-initio non-perturbative approach for numerical calculations in thermal equilibrium, to QCD. Switching on the chemical potential, the cross-over phase transition is predicted to become of the first order by running through a critical point first. However, these predictions have been obtained in less rigorous effective models [38, 39, 40]. Lattice Monte-Carlo simulations fail in this parameter region because of the famous sign problem

[41].

The best way to experimentally probe the phase diagram of QCD are studies of matter produced by colliding heavy ions at different collision energies. Such relativistic heavy-ion collider experiments are currently taken place at RHIC (BNL) and LHC (CERN). In future similar facilities will operate at FAIR (GSI) in Darmstadt. These experiments have provided strong evidence for the existence of QGP [42, 43], while the search for the critical point of QCD is still ongoing [44]. The observation that relativistic hydrodynamics is capable of describing the space-time evolution of QGP for a significant period of time has let to the suggestion, that this exotic state of matter behaves as an almost perfect fluid due to strong interactions between its constituents, quarks and gluons [45].

Our current understanding of heavy-ion collisions [1] divides their time evolution into four subsequent phases:

1. Initial collisions of partons inside of overlapping ions. Happens on proper time scales of $\tau \sim 0.1 fm/c$. Generation of initial conditions for the following time evolution.

2. Non-equilibrium time evolution of quarks and gluons ultimately leading to a (at least) partially thermalized state. May be characterized by plasma instabilities and non-thermal fixed-points. Lasts up to $\tau \sim 1 fm/c$ and the establishment of QGP.

3. Longer period of fireball expansion describable by relativistic viscous hydrodynamics. The system is believed to proceed from the QGP phase to a gas of hadrons by crossing a phase transition, incorporated into hydrodynamical calculations by a change in the equation of state. Ends at $\tau \sim 10 fm/c$ with kinetic freeze-out, releasing a tremendous number of baryons and mesons.

4. Free streaming of isolated particles to the detectors, happens on entirely different time scales of $\tau \sim 1 m/c$.

The knowledge about the details of heavy-ion collisions is based on the detection of particles emitted by the fireball. For our investigations focused on the second, pre-equilibrium phase, electromagnetic observables are especially relevant. The reason is that they are emitted during the whole time evolution, while hadrons mostly capture the physics at freeze-out (end of the third stage). Unfortunately, existing facilities can only measure particle multiplicities integrated over the entire lifetime of a collision, severely constraining experimental capabilities for time resolution of undergoing processes.

For the initial phase of heavy-ion collisions, the colliding partons can be described in the limit of weak gauge couplings in the ”Colour Glass Condensate” (CGC) framework [46]. It results in a non-equilibrium state of QCD matter dominated by coherent classical colour fields and gluonic overoccupation of the long-wavelength modes. We will refer to these findings for the case of defining our initial conditions at the beginning of QCD time evolution.

Current understanding of the second, pre-equilibrium phase, concentrates on the existence of plasma instabilities and universal turbulent fixed-points in an anisotropically expanding, weakly-coupled system [47, 48, 49, 50, 51, 52, 53, 54]. Many studies have considered the non-expanding (at a fixed spatial volume) dynamics of non-Abelian gauge fields far from equilibrium [55, 56, 57, 58, 59]. Less is known for the dynamics of quarks [60, 61] and for more realistic values of the gauge coupling [62]. In this work, our focus rests on quark production and gluon dynamics in non-expanding scenarios. Of course, further going studies will also incorporate the longitudinal expansion. An additional difficulty lies in the uncertainty about the degree of anisotropy and other deviations from thermal equilibrium, which can be reconciled with subsequent hydrodynamical descriptions and experimental data [63]. For this purpose, a deepened understanding of the non-equilibrium dynamics during early evolution of the strongly interacting fireball is a necessary requirement for an interpretation of heavy-ion collisions as probes of the QCD phase diagram.

Chapter 2.

Non-equilibrium Quantum Field Theory

In the following chapter key aspects of quantum fields out of equilibrium are discussed. We present the formalism and tools which can be employed to describe the time evolution of such many-particle systems. Important applications for the chosen formalism include studies of quantum fields undergoing instabilities (2.2.1), the evolution towards thermal equilibrium (thermalization) and the existence of metastable nonthermal fixed points (2.2.2).

2.1. General formalism

The central part of every quantum theory is its inherently probabilistic nature which allows us to precisely calculate probabilities but limits the predictive power for single events. This is why quantum field theory relies on statistical treatment of quantum fields and focuses on determination of correlation functions and their properties. An object containing information about all of the correlation functions is the density operator $\rho_D(t)$, known also as the density matrix. Any expectation value or any n-point function $O(t)$ can in principle be extracted from it by taking

$$\langle O(t) \rangle = \mathrm{Tr}\left[\rho_D(t) O\right] . \tag{2.1}$$

To allow an interpretation of $\rho_D(t)$ as a probability distribution we impose a normalization condition $\mathrm{Tr}\left[\rho_D(t)\right] = 1$ on the density operator at all times. The time evolution of $\rho_D(t)$ itself is governed by the von-Neumann equation

$$i \frac{\partial \rho_D(t)}{\partial t} = \left[H(t), \rho_D(t)\right] , \tag{2.2}$$

which is the quantum generalization of the classical-statistical Liouville equation and consists primarily of the commutator [1] between the density operator and the Hamiltonian

---

[1] As usual the commutator is defined as $[A, B] = AB - BA$.

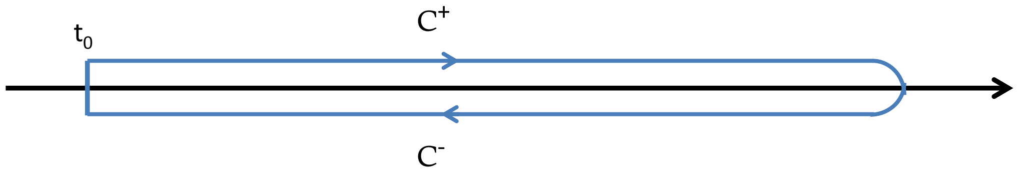

Figure 2.1.: Sketch of the closed time path contour with both positive and negative branches.

of the system. Here and in the following we use natural units with $\hbar = c = k_B = 1$ and the metric tensor $g_{\mu\nu} = diag(1, -1, -1, -1)$. Space-time variables are denoted by $x = (t, \mathbf{x})$, while in cases where four-momentum $p = (p^0, p^j)$ is defined we use $x = (x^0, x^j)$ as well for clarity. Performing actual computations in the operator formalism turns out to be impractical for our purposes. To tackle the time evolution in quantum field theory more efficiently we apply path integral quantization, enabling us to use c-numbers instead of operators. However before doing this we first introduce the concept of a closed time path (CTP) using unitary time evolution operators

$$U(t, t_0) = \hat{T} \exp^{i\int_{t_0}^{t} dt' H(t')}, \tag{2.3}$$

where $\hat{T}$ and H are time ordering and Hamilton operators respectively. Some of the important properties of this object are $U(t_0, t')U(t', t_1) = U(t_0, t_1)$ and $U(t, t) = 1$. Now we can formally solve Eq. (2.2)

$$\rho_D(t) = U(t, t_0)\rho_D(t_0)U(t_0, t), \tag{2.4}$$

such that Eq. (2.1) becomes

$$\langle O(t)\rangle = \mathrm{Tr}\left[\rho_D(t_0)U(t_0, t)OU(t, t_0)\right]. \tag{2.5}$$

What changes is that instead of determining $\rho_D(t)$ we can now evolve the operator itself first forwards and then backwards in time along the CTP and make the statistical average according to the initial density matrix $\rho_D(t_0)$. A graphical sketch of the new time ordering is presented in Fig. 2.1.

2.1.1. Generating functional for correlation functions

In this subsection we introduce the path integral representation of non-equilibrium quantum ensembles by considering the simplified case of a one-component scalar bosonic field theory. At first we consider the standard generating functional (corresponding to the partition function in a purely statistical framework)

$$Z[J,R] = \int \mathcal{D}\varphi \exp\left[iS[\varphi] + \int_x J(x)\varphi(x) + \frac{1}{2}\int_{x,y} \varphi(x)R(x,y)\varphi(y) \right] , \tag{2.6}$$

which depends on linear and quadratic sources $J(x)$ and $R(x,y)$. To extract correlation functions it is more convenient to use the connected generating functional $W[J,R]$ defined by $Z[J,R] = \exp[iW[J,R]]$. By making functional derivatives of $W[J,R]$ with respect to sources we are able to extract correlation functions like the one-point function $\phi(x)$ and the two-point function (propagator) $G(x,y)$:

$$\frac{\delta W[J,R]}{\delta J(x)} = \phi(x) \; , \; \frac{\delta W[J,R]}{\delta R(x,y)} = \frac{1}{2}\left(G(x,y) + \phi(x)\phi(y)\right) . \tag{2.7}$$

For initial value problems the generating functional has to be modified in order to incorporate the initial density operator ρ_D as well as the closed time path C. The resulting path integral [6]

$$\begin{aligned} Z[J,R,\rho_D] \;\; = \;\; & \int [d\varphi_0^1][d\varphi_0^2]\langle\varphi_0^1|\rho_D(t_0)|\varphi_0^2\rangle \int\limits_{\varphi_0^1}^{\varphi_0^2} \mathcal{D}\varphi \, \times \\ & \times \exp\left[iS_C[\varphi] + \int\limits_{x,C} J(x)\varphi(x) + \frac{1}{2}\int\limits_{x,y,C} \varphi(x)R(x,y)\varphi(y) \right] , \end{aligned} \tag{2.8}$$

consists of a functional integral over fluctuating fields on both time branches which are initially distributed according to $\rho_D(t_0)$. This density operator is not restricted to any particular form, making the here presented path integral formulation a very general tool capable of describing initial conditions ranging from the lowest energy state of a theory, the vacuum, to the thermal state of maximized entropy at a given temperature, by considering the corresponding density operator. For systems in thermal equilibrium the density operator is given by $\rho_{D,eq} \sim e^{-H/T}$ with the Hamilton operator H and the temperature T. In this case, the density operator can be included into the path integral by extending the time integration along the imaginary time axis from 0 to $-i/T$, which is an efficient way to dynamically construct $\rho_{D,eq}$ [6].

So far we have seen that the major step involved in tackling general non-equilibrium systems with path integrals is the time evolution of the fields forwards and backwards along the closed time path. For many practical purposes this procedure is replaced by going back to a simple time integration but simultaneously doubling the number of fields, introducing φ_+ and φ_- fields. These degrees of freedom represent fluctuating quantum fields on the positive C^+ and negative C^- time branches respectively (see Fig. 2.1). To clearly separate between classical-statistical fluctuations on one side and genuine quantum fluctuations on the other side a basis transformation is applied:

$$\begin{pmatrix} \bar{\varphi} \\ \tilde{\varphi} \end{pmatrix} = \begin{pmatrix} \frac{1}{2} & \frac{1}{2} \\ 1 & -1 \end{pmatrix} \times \begin{pmatrix} \varphi_+ \\ \varphi_- \end{pmatrix} . \tag{2.9}$$

The new field $\bar{\varphi}$ represents the average of the original fields while the field $\tilde{\varphi}$ stands for the difference between them. The new path integral

$$Z[J,R,\rho_D] = \int [d\bar{\varphi}_0][d\tilde{\varphi}_0]\langle\bar{\varphi}_0+\tilde{\varphi}_0/2|\rho_D(t_0)|\bar{\varphi}_0-\tilde{\varphi}_0/2\rangle \int\limits_{\bar{\varphi}_0,\tilde{\varphi}_0} \mathcal{D}\bar{\varphi}\mathcal{D}\tilde{\varphi} \exp\left[i\mathcal{S}[\bar{\varphi},\tilde{\varphi}] + sources\right] , \tag{2.10}$$

where the sources were omitted for simplicity, will be used in the following subsection to clarify the difference between quantum and statistical effects.

2.1.2. Quantum vs. classical-statistical field theory

The generating functional introduced in Eq. (2.10) contains field fluctuations of both quantum and classical-statistical origin. To disentangle both types of fluctuations we consider as an example a simple scalar bosonic toy model, specified by its action

$$S[\varphi] = \int\limits_x \frac{1}{2}\partial_\mu\varphi\partial^\mu\varphi - \frac{1}{2}m^2\varphi^2 - \frac{\lambda}{4}\varphi^4 , \tag{2.11}$$

with integration running over the whole space but only the forward time branch C^+ from t_0 to t. In a classical theory this action leads to an equation of motion for the fields

$$\left(\Box_x + m^2 + \lambda\varphi_{\mathrm{cl}}^2(x)\right)\varphi_{\mathrm{cl}}(x) = 0 . \tag{2.12}$$

It can be expressed in terms of a functional Fourier transform:

$$\int \mathcal{D}\varphi\mathcal{D}\chi \exp\left[i\int\limits_x \chi\left(\Box_x + m^2 + \lambda\varphi^2\right)\varphi + sources\right] . \tag{2.13}$$

Here the functional integration over auxiliary field χ is employed as a representation of the Delta functional $\delta[\left(\Box_x + m^2 + \lambda\varphi^2(x)\right)\varphi(x)]$. Its role is to constrain the subsequent φ integration to trajectories which are a solution of the classical equation of motion (2.12). To make the comparison with quantum fields more visible we associate in the following χ with $\tilde{\varphi}$ and φ with $\bar{\varphi}$. What is still missing are the initial conditions. We include them via $\rho_W[\bar{\varphi}_0, \dot{\bar{\varphi}}_0]$, a Wigner transform of $\rho_D[\bar{\varphi}_0 + \tilde{\varphi}_0/2, \bar{\varphi}_0 - \tilde{\varphi}_0/2]$. In the end, and after dropping boundary terms, the classical-statistical partition function is given by

$$Z_{\mathrm{cl}}[J,R] = \int [d\bar{\varphi}_0][d\dot{\bar{\varphi}}_0]\rho_W[\bar{\varphi}_0, \dot{\bar{\varphi}}_0] \int \mathcal{D}\bar{\varphi}\mathcal{D}\tilde{\varphi} \exp\left[i\int\limits_x \tilde{\varphi}\left(\Box_x + m^2 + \lambda\bar{\varphi}^2\right)\bar{\varphi} + sources\right] . \tag{2.14}$$

Therefore, the action in the path integral reads

$$S[\bar{\varphi},\tilde{\varphi}] = \int_x \tilde{\varphi}\left(\Box + m^2\right)\bar{\varphi} - \lambda\tilde{\varphi}\bar{\varphi}^3 \,. \tag{2.15}$$

On the other hand, for a quantum field theory on the closed time path action (2.11) would be $S_{\pm}[\varphi_+,\varphi_-] = S[\varphi_+] - S[\varphi_-]$, while in terms of $\bar{\varphi}$ and $\tilde{\varphi}$ we obtain

$$S[\bar{\varphi},\tilde{\varphi}] = \int_x \tilde{\varphi}\left(\Box + m^2\right)\bar{\varphi} - \lambda\tilde{\varphi}\bar{\varphi}^3 - \frac{\lambda}{4}\tilde{\varphi}^3\bar{\varphi} \,, \tag{2.16}$$

where we used that $\varphi_+ = \bar{\varphi} + \tilde{\varphi}/2$ and $\varphi_- = \bar{\varphi} - \tilde{\varphi}/2$. Comparing Eqns. (2.15) and (2.16) we observe that, assuming identical initial conditions, quantum and classical-statistical theories are almost the same. Indeed the only difference is the additional interaction term in the action:

$$\Delta S_{\mathrm{qm}}[\bar{\varphi},\tilde{\varphi}] = \int_x \frac{\lambda}{4}\tilde{\varphi}^3\bar{\varphi} \,, \tag{2.17}$$

which is missing in a classical-statistical framework. In a general bosonic theory (describing fields with integer spin) the terms of purely quantum origin are terms nonlinear in the difference field $\tilde{\varphi}$. As a consequence treating a system in a classical-statistical approximation means ignoring these contributions to the path integral [64, 65, 66]. Such a procedure should be understood as an expansion of $S[\bar{\varphi},\tilde{\varphi}]$ in $\tilde{\varphi}$ truncated at linear order. For practical applications it is more convenient to judge the applicability of this truncation based on correlation functions, especially two-point functions. It turns out that quantum fluctuations are negligible as long as $|\langle\bar{\varphi}(x)\bar{\varphi}(y)\rangle|^2 \gg |\langle\bar{\varphi}(x)\tilde{\varphi}(y)\rangle - \langle\tilde{\varphi}(x)\bar{\varphi}(y)\rangle|^2$ or, in terms of the original fields [64, 65]:

$$F(x,y) = \frac{1}{2}\langle\{\varphi(x),\varphi(y)\}\rangle \gg i\langle[\varphi(x),\varphi(y)]\rangle = \rho(x,y) \,. \tag{2.18}$$

Here we introduced the spectral function $\rho(x,y)$ and the statistical function $F(x,y)$. The former contains information about the spectrum of a theory while the latter tells us how strongly each of the available states is populated. For systems in which classical macroscopic fields are present the classicality condition is slightly modified to

$$|F(x,y) + \phi(x)\phi(y)|^2 \gg |\rho(x,y)|^2 \,. \tag{2.19}$$

In cases in which we are able to define a (quasi-)particle number in momentum space, $n(t,p)$, the criterion for the validity of the classical-statistical approximation simplifies to $n(t,p) \geq 1$.

Stated differently, this concerns the large field or large occupancy limit, which is relevant for important phenomena such as non-equilibrium instabilities, particle creation from large coherent fields or wave turbulence. The description breaks down once the typical field occupancies become of order unity. In particular, this is the case in thermal equilibrium. For an introductory review see Ref. [6].

Finishing our discussion we should note that the initial density operator itself in general also includes quantum effects, making it possible to evolve a quantum system in time solely with statistical methods. For purely Gaussian bosonic systems, e.g. free non-interacting theories, such time evolution would be trivial and exact, as long as the initial conditions are a known eigenstate of the theory. In our work we will take advantage of this issue and start our time evolution of interacting systems with initial conditions based on analytically known Gaussian eigenstates of non-interacting theories.

2.2. Applications

Having laid out the basic ingredients and properties of non-equilibrium quantum field theory in the previous section, we now focus on its typical applications. Of course there is a great amount of possible transient time-dependent states of matter, however the attention of the scientific community is to a large extent concentrated on some very specific challenges. In principle they can be sorted into three distinct categories:

1. Fast time evolution of unstable states going along with changes of the major properties of a particular system, e.g. particle content, typical energy scale, pressure, temperature etc. Such processes are often triggered by either a change in external parameters or a symmetry explicitly broken by initial conditions. In the next subsection we will discuss different initial conditions leading to exponentially growing modes (instabilities), a classical example of fast non-equilibrium physics.

2. Approach towards and small deviations from thermal equilibrium. The latter topic is usually considered under the assumptions of linear response theory and/or expansions around equilibrium, e.g. in hydrodynamics. For larger deviations from equilibrium, the questions of thermalization time and the final temperature of a medium become increasingly important. Interestingly, complete or partial thermalization of a closed quantum system is itself a controversial research topic acquiring great interest from both experimentalists and theoreticians. Here we will discuss thermalization primarily in the contexts of cosmology and heavy-ion collisions.

3. Finally there is a possibility that a system arrives at a nonthermal fixed point. This concept implies that time evolution drives a medium from an initial state not directly towards thermal equilibrium but first to a different nonthermal attractor. Of course a trajectory has to begin sufficiently far from the thermal state in order to be drown to the alternative fixed point. In driven macro- and microscopic systems there is a plethora of such phenomena, most prominent examples being lasers and

turbulence. In closed systems such fixed points are inherently unstable, since finally every statistical ensemble will maximize entropy and equilibrate. However, before it happens the medium can remain in the nonthermal state for arbitrarily long periods of time, an effect occurring e.g. in glasses.

2.2.1. Instabilities and vacuum decay

Instabilities in quantum field theory arise when correlation functions exhibit exponential growth over a finite period of time. In the following we will concentrate on one- and two-point functions and present scalar and plasma instabilities relevant for this work. We will also mention vacuum decay in gauge theories by Schwinger pair production.

Parametric resonance

The phenomenon of parametric resonance is well known from classical physics, where it appears when the length of an oscillating pendulum varies periodically in time. If the external frequency matches the internal frequency of the pendulum the amplitude starts to grow exponentially and finally the pendulum makes a loop. It is striking that such a simple scenario from classical mechanics can, at least at leading order in the amplitude, be exactly matched into an initial value problem in quantum field theory [14, 16, 17]. To make this transition, we first come back to our simple scalar bosonic model in Eq. (2.11) with the potential $V = \frac{1}{2}m^2\varphi^2 + \frac{\lambda}{4}\varphi^4$ and consider only the one-point function (also referred to as a macroscopic field) $\phi(t) = \langle\varphi\rangle$ and the statistical two-point function $F(x, y)$, which encodes the magnitude of field fluctuations. The mapping between the two physical situations connects the external frequency of the change in the pendulum length in classical mechanics to the periodically oscillating macroscopic field. To trigger these oscillations, the field has to be initialized with a sufficiently high amplitude (Fig. 2.2), otherwise the signal of parametric resonance would be suppressed w.r.t. vacuum fluctuations. The unstable pendulum amplitude in classical mechanics is correspondingly identified with quadratic field fluctuations $F(x, y)$. In a purely Gaussian state these fluctuations can be directly interpreted as particle numbers. Hence the overshooting of the pendulum translates into exponentially enhanced particle production in quantum field theory.

Of course this rapid growth of fluctuations cannot be sustained for infinitely long periods of time. The linear approximation of the full dynamics breaks down as soon as the amplitude of fluctuations ceases to be negligible in comparison to the macroscopic field. At this point, non-linear effects come into play. They first change the growth pattern of fluctuations and ultimately stabilize the system. In this work, we will consider the impact of parametric resonance on fermion production in the context of preheating after inflation. For this purpose, the macroscopic field driving the instability is the inflaton field, while the unstable modes translate into inflaton excitations.

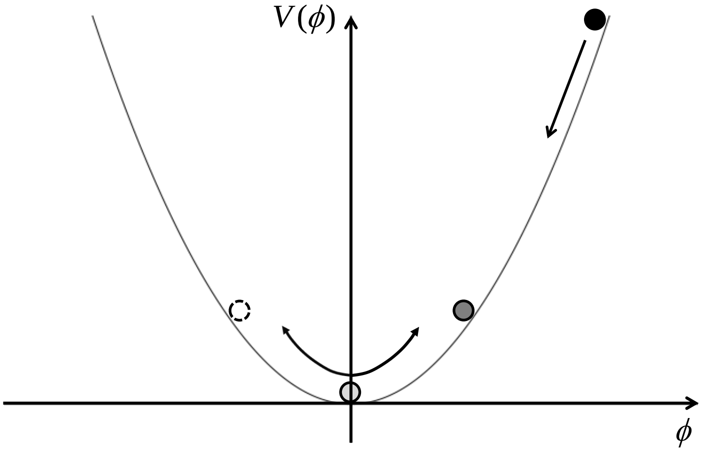

Figure 2.2.: Sketch of initial conditions for parametric resonance, the field begins at a high value and performs damped oscillations in the convex potential.

Spinodal decomposition

The second instability relevant for our studies is the spinodal decomposition, also known as tachyonic instability in cosmological context. It manifests itself as a consequence of a double well potential with two global minima and an unstable local maximum. Such potentials arise naturally during phase transitions in which matter in a symmetric phase is cooled down and exhibits symmetry breaking. Tachyonic instabilities are also a popular model for preheating after inflation, especially if one considers more than one scalar field. In such models one field is responsible for slow-roll during inflation while the second ”waterfall” field plays the dominant part in preheating by exhibiting a tachyonic instability after the first field reached its potential minimum.

To realize spinodal decomposition in our model from Eq. (2.11), the potential has to change its form by switching the sign in front of the mass term, $V = -\frac{1}{2}m^2\varphi^2 + \frac{\lambda}{4}\varphi^4$, a process often called ”quench”. In contrast to parametric resonance here the macroscopic field starts in the local maximum at $\phi = 0$, where it becomes unstable against small perturbations after the quench (Fig. 2.3). However, the main effect is the instability of low-momentum scalar fluctuations. Instead of usual plain-wave solutions $\exp \pm i\omega_p t$, where $\omega_p = \sqrt{|\mathbf{p}|^2 - m^2}$ is the dispersion relation, these excitations exhibit exponentially damped and growing solutions $e^{\pm\gamma_p t}$ with $\gamma_p = \sqrt{m^2 - |\mathbf{p}|^2}$. So in the linear regime all modes with momenta lower than the mass will be amplified. In the non-linear regime a pattern similar to the one known from parametric resonance arises, leading to secondary growth of higher momentum modes and finally to saturation [67].

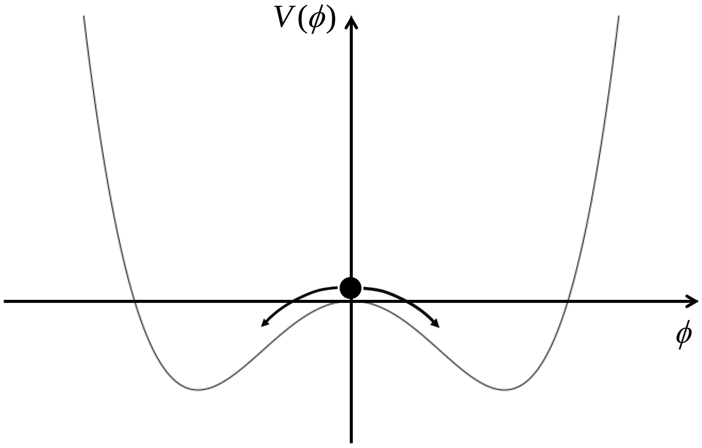

Figure 2.3.: Sketch of initial conditions for spinodal decomposition, the region around the origin becomes concave making the original vacuum unstable.

Schwinger mechanism

It has already been pointed out in the early days of quantum physics that the vacuum of quantum electrodynamics (QED) becomes unstable against the formation of many-body states in the presence of strong external electromagnetic fields. This manifests itself as the creation of electron-positron pairs by the Schwinger mechanism [68, 69, 70]. Nevertheless, this fundamental quantum effect has not been experimentally observed so far as it has not been possible to generate the required electromagnetic field strengths in a laboratory. However, due to the rapid development of laser technology during the last decades, an experimental verification of electron-positron pair production in the focus of high-intensity laser pulses comes into reach.

Vacuum pair production in an applied uniform electric field of strength E_0 may be viewed as a quantum process in which virtual electron-positron dipoles can be separated to become real pairs once they gain the binding energy of $2m$. For this homogeneous scenario without any backreaction of produced fermions onto the original field, the pair production rate per volume has been determined analytically by Schwinger:

$$\Gamma_{Schwinger} = \frac{(eE_0)^2}{4\pi^3} \sum_{n=1}^{\infty} \frac{1}{n^2} \exp\left(-\frac{n\pi m^2}{eE_0}\right) . \tag{2.20}$$

Here n is the number of pairs which tunnel simultaneously from the vacuum and e is the coupling of QED. This linear regime of pair production is strongly modified as soon as the backreaction becomes sizeable and begins to damp the homogeneous field, thus reducing the effective production rate. However, there will be strong spatial and temporal inhomogeneities of the electromagnetic field in realistic situations as envisaged in upcoming high-intensity laser experiments. Thus numerical studies of Schwinger pair production which go beyond the homogeneous case and naturally incorporate inhomogeneities become necessary. It is important to emphasize that Schwinger pair production is not limited to QED but is expected to occur in other gauge theories as well, particularly in QCD. In the context of heavy-ion collisions, this mechanism is believed to contribute to the decay of flux-tubes. These are gauge field configurations appearing in the framework of Color Glass Condensate (CGC) containing coherent chromoelectric fiels in longitudinal direction. Clearly such field configurations could decay via Schwinger mechanism making studies of this effect relevant for an even wider range of physical phenomena.

Nielsen-Olesen plasma instability

In non-abelian gauge theories various instability types are known, mostly arising from anisotropies in initial conditions. One of them is the magnetic Nielsen-Olesen instability generated by the presence of a homogeneous chromomagnetic field. Such field configurations with the field chosen to point in one spatial and one colour direction,

$$B_i^a = \delta^{1a}\delta_{zi}B\,, \tag{2.21}$$

change the dispersion relation of gluonic excitations. Their low-momentum modes become exponentially enhanced with a typical growth rate of $\gamma_p = \sqrt{gB - p_z^2}$, with g being the gauge coupling. In analogy to spinodal decomposition there is a typical scale, here $\sqrt{gB}$, separating stable and unstable regions of phase space. Since enabled through initial anisotropy, this instability will tend to bring the system closer to the isotropic state [71, 72]. In 6.3 we will provide more details for initializing Nielsen-Olesen instabilities in SU(2) gauge theory and show how the isotropization emerges numerically.

2.2.2. Nonthermal fixed points and thermalization

All of the instability mechanisms described in previous subsections have something in common, namely the fact that for a wide range of parameters they lead to a state of matter dominated by infrared fluctuations. This naturally happens since these are the modes that exponentially increase during both linear and non-linear phases of the particular instability, while high momentum modes can only be populated by slower scattering and coalescence processes. We call such infrared enhanced states "overpopulated" because their infrared dominance can be translated into high occupation numbers at low momenta, easily exceeding the occupancies of a thermalized system by orders of magnitude.

But how can we build any realistic expectations about the thermalized state? This can be achieved by exploiting one of the basic conservation laws valid for the systems studied in this work, the energy conservation. We are exclusively focused on closed, non-dissipative systems undergoing unitary time evolution. This means that the initial energy density is also the final energy density of the thermal state.

A caveat at this point lies in the fact that a perfectly unitary time evolution is reversible by construction, strictly prohibiting real thermalization since the entropy of such systems has to be conserved. Properties of matter in full thermal equilibrium should also be completely independent of any details of initial conditions, a memory loss which is technically impossible for the problems treated here. To circumvent these formal obstacles, we will apply a cruder definition of thermalization by comparing a finite set of correlation functions out of equilibrium with those computed in equilibrium. In fact we will concentrate on one- and two-point functions (Gaussian observables) in order to compare particle distributions, instead of comparing the whole probability distribution containing all n-point correlation functions.

What is the physical interpretation for measuring thermalization of only lower n-point correlators for matter undergoing unitary time evolution? One can talk in this context of an apparent thermalization during which lower n-point functions are being driven towards the equilibrium fixed point determined exclusively by conserved quantities, while all the details of the initial state are being preserved in higher correlators. Of course, this picture can only make sense as long as the contribution of all non-Gaussian correlators to the probability distribution is negligibly small w.r.t. the Gaussian part.

Comparison with thermal equilibrium on the level of (quasi-)particle distributions (constructed from Gaussian observables) is done by considering Bose-Einstein distribution for bosons, $n_{BE}(\omega_p) = N_b/(e^{(\omega_p-\mu_b)/T} - 1)$ and Fermi-Dirac distribution for fermions, $n_{FD}(\omega_p) = N_f/(e^{(\omega_p-\mu_f)/T} + 1)$. Here T is the temperature, $\mu_{b/f}$ the bosonic/fermionic chemical potential and ω_p the dispersion relation, while N_b and N_f stand for the number of degrees of freedom for bosons and fermions respectively. It is useful to mention at this point that the Bose-Einstein distribution in the classical limit of $(\omega_p - \mu) \ll T$ takes on the Rayleigh-Jeans form: $n_{RJ}(\omega_p) = N_b T/(\omega_p - \mu)$. A useful physical system to compare with is that of a non-interacting gas of massless bosonic and fermionic particles without any chemical potentials. In this simple case we can analytically determine the integrated energy density ε (Stefan-Boltzmann law):

$$\varepsilon = \frac{\pi^2}{30}\left(N_b + \frac{7}{8}N_f\right)T^4 \,. \tag{2.22}$$

Taking advantage of this relation, we are able to estimate the final temperature of a system just by means of its conserved energy density and counting the number of bosonic and fermionic degrees of freedom. E.g. for Dirac fermions $N_f = 4 \cdot \#flavours$, for photons $N_b = 2$, for $SU(N_c)$ gauge theory $N_b = 2(N_c^2 - 1)$ and for a $O(N)$ symmetric scalar model $N_b = N$.

Coming back to the bosonic overpopulation after instability, we realize that in order to reach thermal equilibrium, the system has to transport energy from low momenta to short length fluctuations. It was observed in previous studies of weakly coupled scalar and non-abelian gauge theories that in such cases a turbulent cascade emerges, accompanied by diverging time scales and self-similar scaling of statistical and spectral two-point functions $F(x, y)$ and $\rho(x, y)$ [73]. Switching from space-time to frequency-momentum regime by Wigner transformation, the equal-time scaling relations are

$$F(\omega, \mathbf{p}) = s^{2+\kappa} F(s^z \omega, s\mathbf{p}) \,, \rho(\omega, \mathbf{p}) = s^{2-\eta} F(s^z \omega, s\mathbf{p}) \,, \tag{2.23}$$

where momentum and frequency are defined w.r.t. relative coordinates $x - y$ and rescaled by an arbitrary number s. We introduced here the dynamical scaling exponent z, anomalous dimension η and scaling exponent κ. The latter governs the scaling behaviour of the particle number distribution $n(\mathbf{p}) \sim |\mathbf{p}|^{-\kappa}$. For a non-interacting or a weakly interacting theory the anomalous dimension is expected to vanish or be much smaller than one while the dynamical exponent z is mostly determined by the dispersion relation, making it one for a relativistic and two for a non-relativistic theory [73, 74].

So far studies of turbulence in non-expanding relativistic quantum field theories revealed a different behaviour for scalar and gauge fields. In $O(N)$ symmetric scalar field theories overpopulation has been shown to evolve towards a double cascade, consisting of an energy cascade towards the ultraviolet and an additional particle cascade to the infrared. The energy cascade takes place in the regime where $1/\lambda \gg n(\mathbf{p}) \gg 1$ and the corresponding exponent has been evaluated perturbatively to the value of $\kappa = 3/2$, in accordance with numerical simulations [58]. The particle cascade on the other side usually takes place where the occupation numbers are non-perturbatively high, $n(\mathbf{p}) \geq 1/\lambda$. In this region the scaling exponents have been determined using a $1/N$ expansion to next-to-leading order (NLO) for variable spatial dimensionality [73]:

$$\kappa = -\eta + z + d \,. \tag{2.24}$$

For three spatial dimensions $\kappa_{3d} = 4$. The reason for this nontrivial fixed point in the infrared momentum region is that inelastic scattering processes are suppressed compared to elastic scattering, so that the system is unable to get rid of the over-abundance of particles. This results in an inverse particle cascade, also known as strong turbulence, transporting particles towards the infrared. Finally these particles condense in the zero mode and contribute to the build-up of a transient non-equilibrium analogue of Bose-Einstein condensate. The condensate survives for parametrically long times before decaying via inelastic processes before the system equilibrates.

For gauge fields inelastic and elastic scattering are equally efficient, such that only a single cascade can be maintained. The value for critical exponent κ is $3/2$ for earlier and $4/3$ for late times. These values have been found numerically and are supported by the analysis of dominant matrix elements in the framework of Boltzmann equations [59, 58]. Earlier gauge dynamics, characterized by $\kappa = 3/2$, may be influenced by condensation of ultra-soft gluon modes, similar to the scalar case. However this remains a controversial proposal since any condensate would be a gauge dependent and thus unobservable quantity. A recent work [75] suggests that at even later times the critical exponent could become indistinguishable from the classical equilibrium, namely $\kappa = 1$.

Chapter 3.

Methods

In the previous chapter we introduced the basic concepts of non-equilibrium quantum field theory in the path integral formulation and named some physical applications relevant for this work. In the following we present some computational techniques and truncations which can be used to evaluate the path integral numerically and to compute the time evolution of correlation functions. First of all the method of classical-statistical lattice field theory will be explained, which is one of the central tools we use to obtain our results. Afterwards we focus on the two-particle irreducible effective action and Kadanoff-Baym equations of motion, also mentioning possible truncation schemes in this framework. Finally, we will shortly discuss kinetic theory, its derivation from the path integral approach and Boltzmann equations.

3.1. Lattice

There is a significant class of problems where the dynamics of bosonic quantum fields can be accurately mapped onto a classical-statistical system. This is the case whenever anti-commutator expectation values for bosonic fields are much larger than the corresponding commutators [64], as we have already stated in 2.1.2. This limit has been studied extensively for scalar field theories [16, 64, 20, 76, 74] as well as pure gauge theories [55, 56, 57, 58, 59, 47]. In this limit, observables can be obtained as ensemble averages of solutions of classical field equations. To motivate this numerically advantageous procedure, we go back to Eq. (2.14),

$$Z_{\mathrm{cl}} = \int [d\bar{\varphi}_0][d\dot{\bar{\varphi}}_0]\rho_W[\bar{\varphi}_0, \dot{\bar{\varphi}}_0] \int \mathcal{D}\bar{\varphi}\mathcal{D}\tilde{\varphi} \exp\left[i \int_x \tilde{\varphi} \left(\Box_x + m^2 + \lambda\bar{\varphi}^2 \right) \bar{\varphi} \right], \qquad (3.1)$$

and perform the integration over $\tilde{\varphi}$ analytically. By doing this, we make a step backwards from the path integral formulation towards the original classical formulation in terms of equations of motion for classical fields (see Eq. (2.12)). After this functional Fourier transform we arrive at an expression dominated by a Delta functional, here written for the computation of an expectation value (since we are usually interested in expectation values of an operator and not the generating functional itself):

$$\langle O \rangle = \int [d\varphi_0]\,[d\dot{\varphi}_0]\; W[\varphi_0, \dot{\varphi}_0] \int \mathcal{D}\varphi\; O(\varphi)\, \delta[\varphi - \varphi_{\rm cl}(\varphi_0, \dot{\varphi}_0)]\,. \qquad (3.2)$$

Here $\varphi_{\rm cl}(\varphi_0, \dot{\varphi}_0)$ is the solution of the classical field equation (2.12) with initial conditions φ_0 and $\dot{\varphi}_0$, later we will refer to it as a particular trajectory of the system. We consider canonical field variables at initial time t_0, i.e. $\varphi_0(x) = \varphi_{\rm cl}(t_0, \mathbf{x})$ and $\dot{\varphi}_0(x) = \partial_t \varphi_{\rm cl}(t, \mathbf{x})|_{t=t_0}$ for the classical field $\varphi_{\rm cl}(x)$. The values for the canonical field variables at initial time are distributed according to a normalized phase-space density functional $W[\varphi_0, \dot{\varphi}_0]$, such that the external functional integration in (3.2) are realized numerically by an arithmetic average over trajectories [64, 77]. Ensemble averages at initial time are taken to correspond to the respective quantum expectation values for the fields, emphasizing once more the crucial importance of quantum effects in the initial conditions.

One of the most important advantages of classical-statistical simulations is field values are available at every point in time and space, while most of the other methods are truncated to a sub-set of lower correlation functions. In particular, the evolution of all higher bosonic n-point correlation functions can be easily constructed by averaging over products of $\varphi_{\rm cl}$ and $\dot{\varphi}_{\rm cl}$ such as $\langle \varphi_{\rm cl}(x)\varphi_{\rm cl}(y)\varphi_{\rm cl}(z)\ldots\rangle$. In principle the results for these and all other observables have to be obtained after averaging over infinitely many trajectories. In practice the number of simulations needed to achieve convergence (up to the desired level of accuracy) is finite and can be further reduced by the volume average for spatially homogeneous ensembles.

Numerical simulations in the classical-statistical framework are carried out using a leap-frog algorithm[1] on a $d+1$ dimensional space-time lattice with a real time coordinate. The simulated spatial volume is $V = (Na_s)^d$ with spatial lattice spacing a_s and number of lattice points N in each direction, where periodic spatial boundary conditions are used. The momentum resolution is determined by N and a_s, with the highest possible lattice momentum proportional to $1/a_s$ and the lowest one to $1/(Na_s)$[2]. The time direction is discretized using a lattice spacing a_t and length $t_{\rm max} = N_t a_t$.[3]

First- and second-order derivatives on the lattice are discretized using symmetric finite

---

[1] This algorithm reduces computer memory requirements because only variables for the previous t_{i-1} and the current t_i timesteps are saved. The fields at the next timestep t_{i+1} are calculated from this two sets of information using equations of motion and immediately overwrite the fields at t_{i-1} in memory. Finally the memory addresses of the two sets of variables are switched, since for the next step t_i takes on the role previously played by t_{i-1}.

[2] On the lattice momentum integrals are replaced by sums: $\int \frac{d^3p}{(2\pi)^3} \longrightarrow \frac{1}{N^3 a_s^3} \sum_{\mathbf{p}}$.

[3] There is no (anti-)periodicity in real time employed, as is typically the case for Euclidean lattice formulations.

difference approximations

$$f'(x) = \frac{f(x+a_i) - f(x-a_i)}{2a_i}\,,$$
$$f''(x) = \frac{f(x+a_i) + f(x-a_i) - 2f(x)}{a_i^2}. \tag{3.3}$$

Here a_i with $i = s, t$ denotes either the spatial or temporal lattice spacing. For the calculation of second-order bosonic spatial derivatives an alternative higher-order discretization can be applied, which is slightly more accurate for larger lattice spacings:

$$f''(x) = \frac{16f(x+a_i) + 16f(x-a_i) - f(x+2a_i) - f(x-2a_i) - 30f(x)}{12a_i^2}\,. \tag{3.4}$$

To remain consistent with the lattice version of derivatives, it is necessary to define lattice momenta. This is achieved by applying discrete derivatives to plane-wave solutions (typically spanning the basis of solutions for free non-interacting fields), such as $\partial_x e^{ipx} = \left[(e^{ipa_s} - e^{-ipa_s})/(2a_s)\right] e^{ipx}$. The corresponding lattice momentum definitions are

$$\bar{p}_i = \frac{\sin(p_i a_s)}{a_s}\,, \qquad i = 1,2,3 \tag{3.5}$$

for a first order spatial derivative as appearing in a Dirac equation for fermions, or

$$\mathbf{p}^2_{\text{lat}} = \frac{1}{a_s^2}\sum_{i=1}^{3} 4\sin^2\left(\frac{p_i a_s}{2}\right) \tag{3.6}$$

for second-order spatial derivatives as ones appearing in a Klein-Gordon equation with $p_i = 2\pi n_i/(N a_s)$ and $n_i = 0, ..., N-1$. For scalar bosonic theories we can also use the higher-order discretization (3.4), which leads to

$$\mathbf{p}^2_{\text{lat}} = \frac{1}{a_s^2}\sum_{i=1}^{3}\left[2.5 - \frac{8}{3}\cos\left(p_i a_s\right) + \frac{1}{6}\cos\left(2p_i a_s\right)\right]. \tag{3.7}$$

Typically the stability of a leap-frog algorithm requires that temporal lattice spacings are significantly smaller than the spatial ones. In our simulations, this criterion is fulfilled by choosing $a_s/a_t \geq 20$.

3.2. Two-particle irreducible effective action

Classical-statistical lattice simulation techniques described in 2.1.2 and 3.1 provide a powerful tool for many nonequilibrium applications, they have been successfully used to describe instabilities [78, 17] and to explore properties of nonthermal fixed points in scalar and gauge theories [79, 80, 81, 82, 55, 56, 57, 58, 59, 47]. But despite all of these advantages there are still many problems lying out of the range of validity of classical-statistical methods. In particular the thermalization process inherently involves lowering of typical occupation numbers, down to the order of unity and below, invalidating basic assumptions of the lattice approach. Therefore it is often necessary to employ different techniques which have their strength where lattice simulations start to fail. An important tool for real-time problems in quantum field theory is the two-particle irreducible (2PI) effective action, a functional method sharing some similarities with Dyson-Schwinger equations. Here we will briefly introduce this approach, for a more thorough introduction and derivation we refer to [6] and references therein.

Let us start with the generating functional on the closed time-path (Eq. (2.8)) and the respective connected generating functional $W[J, R, \rho] = -i\ln(Z[J, R, \rho])$. Our first step is to switch functional variables from external sources $J(x)$ and $R(x, y)$ to internal correlation functions of the system. To achieve this, we perform a double Legendre transform w.r.t. to linear and bilinear sources:

$$\Gamma_{2PI}[\phi, G] = W - \int_x \underbrace{\frac{\delta W}{\delta J(x)}}_{=\phi(x)} J(x) - \int_{x,y} \underbrace{\frac{\delta W}{\delta R(x,y)}}_{=\frac{1}{2}(G(x,y)+\phi(x)\phi(y))} W(x,y)\,. \tag{3.8}$$

The resulting 2PI effective action depends on the macroscopic field $\phi(x)$ and the propagator $G(x, y)$, as defined in Eq. (2.7)[4]. Most importantly, the propagator here is a "dressed" two-point correlator of an interacting system and not the explicitly known bare propagator $G_0(x, y)$ as usually encountered in perturbation theory. For simplicity we assumed that the density operator is a Gaussian object and has been incorporated into linear and bilinear sources at initial time, although a procedure to incorporate non-Gaussian density operators in 2PI computations has also been developed [83]. The effective action for the non-interacting part of a bosonic theory is exactly given by

$$\Gamma^0_{2PI}[\phi, G] = S[\phi] + \frac{i}{2} Tr \ln G^{-1} + \frac{i}{2} G_0^{-1} G\,, \tag{3.9}$$

where we took advantage of a compact notation writing product of functions, logarithm and trace over all internal and space-time indices in the functional sense. Effective action for the non-interacting part of a fermionic system looks very similar

$$\Gamma^0_{2PI}[G_\psi] = -iTr \ln G_\psi^{-1} - iG_{0,\psi}^{-1} G_\psi\,, \tag{3.10}$$

the only major change being the absence of a purely classical part like $S[\phi]$ for bosons, since there is no macroscopic fermion field, $\langle\psi(x)\rangle = \langle\bar{\psi}(x)\rangle = 0$.

---

[4] If we had chosen to make a triple or even higher Legendre transform we would arrive at 3PI or even nPI effective action depending on n-point correlation functions. Such higher Legendre transforms may be relevant for certain quantum field theories.

For interacting theories the effective action is modified in two ways. A minor effect is the possibility that both bosonic and fermionic bare propagators may now depend on the macroscopic field ϕ. But the main difference comes from completely new terms in the effective action, $\Gamma_{2PI} = \Gamma^0_{2PI} + \Gamma_2$. In the full nonlinear theory Γ_2 would take into account interactions between quantum fields to all orders in any expansion, however for realistic applications we are forced to apply an appropriate expansion for every physical problem and truncate it at finite order. In the diagrammatic picture Γ_2 is a sum of closed loop diagrams, with lines being propagators, vertices being proportional to coupling constants and every closed loop associated with an integration over space-time or four-momentum. This picture is especially useful when considering a loop expansion, a coupling expansion in the number of loops in a Feynman graph. But contrary to standard perturbation theory, the lines in these graphs are not just bare but consistently dressed propagators, meaning that a single 2PI loop diagram resums infinitely many orders of perturbation theory. In the 2PI approach the number of loop diagrams at each order is significantly smaller than in perturbation theory or the 1PI effectve action approach [6], because only those diagrams which can not be separated by cutting two propagator lines are contributing. Another advantage of 2PI is the absence of secularities in the time evolution, a problem which prevents successful utilization of standard perturbative or 1PI expansions for real-time problems. Loop expansion of the 2PI effective action has been applied to bosonic and fermionic theories in and out of equilibrium [84, 85, 86], one of its early successes was the first numerical example of thermalization in quantum field theory [84].

Since many exciting problems in modern physics are posed for the regime of strong coupling or parametrically high occupation numbers, an alternative expansion scheme is required. The reason is that loop expansion breaks down whenever diagrams with many loops become more or equally important than those with few loops. This naturally occurs for couplings ≥ 1 or in regimes of bosonic overpopulation. In models with N either bosonic or fermionic fields interacting exclusively via quartic self-interaction, a non-perturbative $1/N$ expansion is available [78]. This expansion reorders processes as a series in the number of fields with leading order (LO) proportional to N^1, next-to-leading order (NLO) proportional to N^0, next-to-next-to-leading (NNLO) to N^{-1} etc. The leading order in these models is the collisionless meanfield or Hartree approximation, in which every particle interacts only with an averaged background field. In the case of a $O(N)$ theory the $1/N$ expansion has been efficiently resummed and after truncating at NLO compared to classical-statistical lattice simulations [74]. The comparison showed that for moderate number of fields ($N = 4$) the NLO $1/N$ results reproduce non-perturbative behaviour at strong coupling as well as parametrically strong fluctuations and exhibit good agreement with lattice simulations.

A core strength of the 2PI effective action approach is its thermodynamic consistence, meaning that in this method the energy conservation is preserved for all times up to the level of numerical accuracy[5]. The reason for this advantage is that all truncations are

---

[5] This fact also allows calculations of thermodynamic observables, e.g. pressure, in thermal equilibrium

made on the level of the effective action Γ_{2PI} and not just in equations of motion.

After choosing a certain truncation e.g. by using an expansion of Γ_2 in a small dimensionless parameter, we have to derive equations of motion from the now fixed form of effective action. Having a 2PI action which depends on bosonic and fermionic correlators in a symmetric phase ($\phi = 0$), we obtain equations of motion for them by

$$\frac{\delta\Gamma[\phi, G, G_\psi]}{\delta G(x,y)} = 0\,, \quad \frac{\delta\Gamma[\phi, G, G_\psi]}{\delta G_\psi(x,y)} = 0\,. \tag{3.11}$$

After this variation we get an analogue of Dyson-Schwinger equations presented here in a compact form with self-energies $\Sigma(x, y)$ and $\Sigma_\psi(x, y)$:

$$\begin{aligned} G^{-1}(x,y) &= G_0^{-1(x,y)} - \Sigma(x,y)\,, \quad \Sigma(x,y) = 2i\frac{\delta\Gamma_2}{\delta G(x,y)}\,, && (3.12) \\ G_\psi^{-1}(x,y) &= G_{0,\psi}^{-1}(x,y) - \Sigma_\psi(x,y)\,, \quad \Sigma_\psi(x,y) = -i\frac{\delta\Gamma_2}{\delta G_\psi(x,y)}\,. && (3.13) \end{aligned}$$

For real-time numerical computations we decompose the propagators and the self-energies into their local, statistical and spectral parts, here presented for the bosonic scalar toy model from 2.1.2:

$$G(x,y) = F(x,y) - \frac{i}{2}\rho(x,y)\,\mathrm{sgn}(x^0 - y^0)\,, \tag{3.14}$$

$$\Sigma(x,y) = \Sigma_{\mathrm{local}}(x)\delta(x-y) + \Sigma_F(x,y) - \frac{i}{2}\Sigma_\rho(x,y)\,\mathrm{sgn}(x^0 - y^0)\,. \tag{3.15}$$

Thus we arrive at the Kadanoff-Baym equations of motion for two-point functions:

$$\begin{aligned} \left[\Box_x + M^2(x)\right] F(x,y) &= -\int_0^{x^0} dz\,\Sigma_\rho(x,z)F(z,y) \\ &\quad + \int_0^{y^0} dz\,\Sigma_F(x,z)\rho(z,y)\,, \\ \left[\Box_x + M^2(x)\right] \rho(x,y) &= -\int_{y^0}^{x^0} dz\,\Sigma_\rho(x,z)\rho(z,y)\,. && (3.16) \end{aligned}$$

Here $M^2(x)$ is the local effective mass, changed by interactions at meanfield level due to tadpole contributions contained in the local part of the self-energy, $\Sigma_{\mathrm{local}}(x)\delta(x-y)$[6]. For

---

[86].

[6] There is also a contribution to the effective mass coming from symmetry breaking in scalar models.

gauge fields and fermions the right-hand side of these equations remains identical while the left-hand side changes according to the form of the inverse bare propagator in these theories. These Kadanoff-Baym equations of motion are very general, since every possible truncation scheme would only influence the self-energies on the right-hand side of the equations. For the case of a non-vanishing macroscopic field these equations are supplemented by an evolution equation for ϕ. The final set of equations is then usually Fourier transformed in relative spatial coordinates to spherical momentum space and discretized in time and absolute values of momentum using standard techniques.

A central property of Kadanoff-Baym equations is the occurrence of memory integrals on the right-hand side of Eq. (3.16): The integration runs over the whole history of the system. By the virtue of this memory effect we are able to take into account non-Markovian processes during the time evolution. However, this feature comes along with a massive computational drawback, namely the need to store the complete time history in computer memory. The consequence is that the amount of memory which 2PI computations require scales quadratically with the number of simulated timesteps, making studies of long time scales incredibly hard.

3.3. Kinetic theory

In the previous two sections we have covered two very distinct methods for real-time calculations in quantum field theory, both of them relied on a description in terms of quantum fields and their correlation functions. But for many applications a more accessible (but potentially less rigorous) approach is desirable. One of such methods will be introduced in this section.

Here we will cover the kinetic approach to non-equilibrium problems, designed for small deviations from thermal equilibrium and for dilute and weakly interacting gases of quantum (quasi-)particles with well-defined dispersion relations. The strongest simplification done in kinetic equations is the assumption that all of the relevant phenomena are included in a time and phase-space dependent particle distribution $n(x, p, t)$. This is equivalent to enforcing a Gaussian state at all times, in contrast to 2PI or lattice simulations. Another caveat lies in the fact that phase-spaces in quantum theories are not well defined. Uncertainty relations prevent spectators from exact and simultaneous determination of a particle's location and momentum. Nevertheless, one is able to formulate an equation of motion for a phase-space distribution which we will refer to as Boltzmann equation, although many scientist contributed to its development in the modern form. The general form of a Boltzmann equation is

$$\left[\frac{\partial}{\partial t} + \mathbf{v}\cdot\nabla_{\mathbf{x}} + \mathbf{F}\cdot\nabla_{\mathbf{p}}\right] n(x, p, t) = C[n(x, p, t)]\,, \tag{3.17}$$

where $\mathbf{v}$ is the velocity associated with a particle with momentum $\mathbf{p}$ and $\mathbf{F}$ a possible external force acting on it. The left-hand side of this equation consists of the time derivative, a drift term proportional to the spatial gradient and appearing only in inhomogeneous systems and a term describing the change of a particle's momentum due to an external force. Such interactions with external forces are especially relevant for particles moving in coherent Abelian and non-Abelian gauge fields, since their trajectories are modified by the Lorentz force (e.g. Vlasov equations [87]). The right-hand side is determined by the collision term $C[n(x, p, t)]$ describing inter-particle scattering processes in which the total energy and momentum of participants are conserved. There are two possible types of collision events, elastic and inelastic. The former additionally conserve the total number of particles while the latter change this quantity. A common notation for different scattering processes is $m \to n$, where m is the number of incoming and n of outgoing participants.

What is the typical explicit form of a collision integral? To give an example, we will explain here the structure of $C_{2\to2}[n(p, t)]$, an elastic process with few participants for a spatially homogeneous problem:

$$\begin{aligned} C_{2\to2}[n(p_1, t)] &= \int \frac{d^3p_2}{(2\pi)^3 2\omega_2} \frac{d^3p_3}{(2\pi)^3 2\omega_3} \frac{d^3p_4}{(2\pi)^3 2\omega_4} \frac{1}{2\omega_1} |M_{12\to34}|^2(p_1, p_2, p_3, p_4)(2\pi)^4 \times \\ &\quad \times \delta^4(p_1 + p_2 - p_3 - p_4)\, [n_1 n_2 (1 + n_3)(1 + n_4) - (1 + n_1)(1 + n_2) n_3 n_4] \,. \end{aligned} \tag{3.18}$$

Obviously energy and momentum conservation are enforced by the Delta function while the collision integral runs over all momenta of participants except for the external momentum p_1. The other parts include products of distribution functions for all involved momenta contributing to the quantum-statistical part of $C_{2\to2}[n(p, t)]$ and the matrix element $|M_{12\to34}|^2(p_1, p_2, p_3, p_4)$. The latter object holds the entire information about the vacuum cross-section of involved particles and is the only part that explicitly depends on the microscopic theory. E.g. the cross-section for 2 → 2 gluon scattering in QCD is fundamentally different from the 2 → 2 scattering in scalar field theories, nevertheless both processes can usually be described by an almost identical Boltzmann equation. So the typical procedure to set-up a Boltzmann computation is, besides choosing suitable initial conditions for $n(x, p, t)$, to identify important processes which have to be included and then to calculate or look up the corresponding matrix elements. One common way to obtain these matrix elements is by perturbative calculations up to a desired order in the coupling.

Another exciting feature of this Boltzmann equation lies in the fact that we can easily distinguish between terms which would dominate in the classical regime and those important for genuine quantum calculations. We already introduced a similar classification for quantum fields in 2.1.2 in order to establish the assumptions behind the classical-statistical approximation. Concentrating on the statistical part of Eq. (3.18), we are able to identify two types of contributions

$$\begin{aligned}\Big[n_1n_2(1+n_3)(1+n_4)-(1+n_1)(1+n_2)n_3n_4\Big] &= \Big[n_1n_2n_3+n_1n_2n_4-n_1n_3n_4-n_2n_3n_4\Big]_{\mathrm{cl}}+\\ &+\Big[n_1n_2-n_3n_4\Big]_{\mathrm{qm}}\,,\end{aligned} \tag{3.19}$$

those cubic and quadratic in powers of the distribution functions. If we remind ourselves that the classical-statistical limit is approached for $n \gg 1$, we come to the conclusion that in this limit only cubic terms would contribute to the scattering. As a consequence, achieving quantum thermalization would require to take into account cubic as well as quadratic terms[7].

Having covered some specifics of Boltzmann equations, we would like to finish this discussion by outlining the connection between 2PI effective action and kinetic theory [6]. We will show which assumptions are needed to derive the Boltzmann equation for particle distributions from the Kadanoff-Baym equations 3.16 for correlators [88]. Our first step is a Wigner transformation of $F(x,y)$ and $\rho(x,y)$ from x and y coordinates to relative $s = x-y$ and center $X = \frac{x+y}{2}$ coordinates. Afterwards, we subtract the Hermitian conjugate of 3.16 (in the new coordinates) from 3.16 itself and expand the result in gradients w.r.t. the center coordinates, ∂_X. Only the leading terms are kept. The lower limit of the memory integrals is sent to $-\infty$. Thus we assumed that initial conditions are defined in the remote past and that the time evolution is sufficiently slow to justify a gradient expansion. The latter assumption already gives us a hint that Boltzmann equations are not capable of describing fast processes like instabilities. Equations we get by these manipulations are already local in center time X^0:

$$2k^\mu\partial_{X^\mu}F(X,k) = \Sigma_\rho(X,k)F(X,k)-\Sigma_F(X,k)\rho(X,k)\,, \tag{3.20}$$

$$2k^\mu\partial_{X^\mu}\rho(X,k) = 0\,. \tag{3.21}$$

Here a Fourier transformation in relative coordinates s was performed so that k is the corresponding momentum. A nice benefit of starting from an action is visible at this point, since we are able to insert any set of formerly closed loop diagrams into spectral and statistical components of the self-energy, automatically generating perfectly consistent matrix elements and statistical factors. Additionally restricting ourselves to homogeneous problems, we may drop the dependence on the spatial center coordinates $\mathbf{X^j}$, realizing that the spectral function at this order in the gradient expansion is strictly static, $\partial_{X^0}\rho(X,k) = 0$. Now we are able to switch from describing dynamics of correlators to that of particle

---

[7] Here we discussed the limit of classical wave dynamics, the (long wavelength) infrared limit of every quantum theory. There exists also the opposite ultraviolet limit of classical (short wavelength) point-particles. In this limit the cubic terms are dropped in favour of the quadratic contributions, since in the ultraviolet $n \ll 1$.

numbers by the means of a generalized fluctuation-dissipation relation:

$$F(X^0, k) = \left[\frac{1}{2} + n(X^0, k)\right]\rho(k)\,. \tag{3.22}$$

In thermal equilibrium this relation would be exactly fulfilled and the distribution function would be the Bose-Einstein distribution. For the non-equilibrium case this generalized fluctuation-dissipation relation defines the time-dependent particle number. In order to arrive at a familiar form for Boltzmann equations, we need a few more steps. First, we assume a (quasi-)particle picture with on-shell energies for the in- and outcoming particles. This yields a specific form for the spectral function, typical for stable on-shell particles. The last step is to integrate out the relative frequency k^0, leaving an effective (momentum dependent) particle density $n(X^0, k)$. To summarize, we restate the assumptions required to derive a Boltzmann equation:

1. Gradient expansion to leading order.
2. Sending the initial time to the infinitely remote past.
3. Specific (quasi-)particle form of the spectral function.
4. Generalized fluctuation-dissipation relation.

Finally we remark that higher order truncations of the gradient expansion can be utilized to obtain kinetic equations beyond Boltzmann.

Chapter 4.

Lattice Fermions

So far our focus in the chapters on lattice techniques and the classical-statistical approximation in Secs. 2.1 and 3.1 lied on calculations in purely bosonic theories. Here we will extend this discussion towards including fermionic degrees of freedom in a non-perturbative fashion. For this sake we use our toy model from 2.11 and couple it to a quadratic fermion sector, $S[\varphi, \bar{\psi}, \psi] = S_B + S_F$ with

$$S_F[\varphi, \bar{\psi}, \psi] = \int\limits_{x,C} \bar{\psi} \left(i\,\partial_\mu \gamma^\mu - m \right) \psi - h\bar{\psi}\varphi\psi\,, \tag{4.1}$$

with the real-time contour C, and S_B remaining in the same form as in 2.11. The partition function without source terms is now given by

$$Z = \int [d\varphi_0][d\bar{\psi}_0][d\psi_0]\rho[\varphi_0, \bar{\psi}_0, \psi_0](t_0) \int \mathcal{D}\varphi\mathcal{D}\bar{\psi}\mathcal{D}\psi\; e^{iS_B[\varphi]+iS_F[\bar{\psi},\psi,\varphi]}\,. \tag{4.2}$$

We restrict ourselves to fermions appearing quadratically in the action because they resemble the fermionic contributions to the Standard Model, in particular both QCD and QED are quadratic in fermion fields. Additionally, we assume that also the initial density operator is quadratic in ψ and $\bar{\psi}$. However, this assumption is less strict and could be avoided by altering the time integration path.

Exploiting the rules for Gaussian Grassmann-valued integration, we integrate out fermions in the partition function and arrive at

$$Z = \int [d\varphi_0]\rho[\varphi_0](t_0) \int \mathcal{D}\varphi\; \det\!\left[i\,\partial_\mu\gamma^\mu - m - h\varphi\right]\, e^{iS_B[\varphi]}\,. \tag{4.3}$$

This procedure is similar to the one applied in Euclidean lattice QCD although the numerical implementation in real-time is different. For instance in the following sections the evaluation of the fermion determinant will be accomplished by solving Dirac-like equations of motion for two-point correlators [22].

After having integrated out fermion fields, we are left with a bosonic path integral albeit our new action has an additional nonlinear term

$$\det\left[i\,\partial_\mu\gamma^\mu - m - h\varphi\right]\, e^{iS_B[\varphi]} = e^{iS_B[\varphi]+\mathrm{Tr}\log\left[i\,\partial_\mu\gamma^\mu - m - h\varphi\right]} = e^{iS_B^{eff}[\varphi]}\,. \tag{4.4}$$

In spite of having now a rather complicated form of bosonic self-interaction, we can easily repeat all of the steps made in Sec. 2.1, especially the introduction of $\bar{\varphi}$ and $\tilde{\varphi}$ fields. Finally, to have a self-consistent description, we solve the new effective path integral using classical-statistical lattice simulations. Formally it corresponds to an expansion of $S_B^{eff}[\varphi]$ in powers of $\tilde{\varphi}$ up to the linear order. The approximation involved in ignoring infinitely many terms with higher powers of $\tilde{\varphi}$ remains the same as in 2.1.2 and is only valid for sufficiently high bosonic occupation numbers[66]. Comparing the emergent classical-statistical action to the one known from purely bosonic theory without the fermion determinant, we can immediately associate the additional terms linear in $\tilde{\varphi}$ with the backreaction of the fermionic sector onto the dynamics of bosons. For scalars, the corresponding equation of motion reads

$$\left(\Box_x + m^2\right)\varphi_{\mathrm{cl}}(x) + \frac{\lambda}{6}\varphi_{\mathrm{cl}}^3(x) = -J_\psi\,, \tag{4.5}$$

with the backreaction J_ψ. Its explicit form will be determined later in the course of this work for various physical models including those based on gauge symmetry.

4.1. Mode functions

We will describe two numerical methods for the time evolution of fermionic two-point correlation functions. In this section, we begin with a method that despite being computationally expensive is an exact solution without any additional approximations [22]. But before explaining in details the mode function approach let us first clarify which correlators are really required to describe time evolution of a mixed boson-fermion system. We begin with the equation of motion for classical-statistical scalar fields in our already introduced toy model with fermions

$$\left(\Box_x + m^2\right)\varphi_{\mathrm{cl}}(x) + \frac{\lambda}{6}\varphi_{\mathrm{cl}}^3(x) + h\langle\bar{\psi}(x)\psi(x)\rangle = 0\,. \tag{4.6}$$

Apparently the backreaction of fermions onto scalar dynamics is contained in $\langle\bar{\psi}\psi\rangle$. It turns out that this expectation value, which is nothing else but the local fermion mass density, can be written in terms of the statistical propagator $F_\psi(x,y) = \frac{1}{2}\langle[\psi(x),\bar{\psi}(y)]\rangle$ via

$$\langle\bar{\psi}(x)\psi(x)\rangle = -\mathrm{Tr}\left[\mathrm{F}_\psi(\mathrm{x},\mathrm{x})\right]\,, \tag{4.7}$$

where the trace runs over all possible internal degrees of freedom. Since statistical propagators encode the information about occupation numbers, their time evolution is of central interest for studies of particle production. Therefore, we will concentrate on the computation of $F_\psi(x,y)$. However, the method applied here could also be used to determine how the spectral propagator $\rho_\psi(x,y) = i\langle\{\psi(x),\bar{\psi}(y)\}\rangle$ evolves in time. Our starting point is the field operator $\psi(x)$, an object which is unobservable itself but which can be used to derive equations of motion for correlators. In presence of classical or classical-statistical bosonic fields the field operator fulfils the Dirac-like equation

$$\left[i\partial_{\mu,x}\gamma^\mu - h\varphi(x)\right]\psi(x) = 0\,, \tag{4.8}$$

which is the operator equation of motion from canonical quantization in the limit of classical (not operator-valued) bosonic fields. By multiplying from the right with $\bar{\psi}(y)$ we can continue to construct the evolution equation for the fermion commutator. Since the fermion fields only appear quadratically in the Lagrangian (giving rise to the linearity of Eq. (4.8)), one obtains a Dirac-like equation of motion for the expectation value $F_\psi(x,y)$:

$$\left[i\partial_{\mu,x}\gamma^\mu - h\varphi(x)\right]F_\psi(x,y) = 0\,. \tag{4.9}$$

To derive this result, we took advantage of the fact that the classical field $\varphi(x)$ as well as the derivative operator commute with fermion operators. The conjugate field $\bar{\psi}(y)$ also fulfils a similar equation of motion

$$-\,i\partial_{\mu,y}\bar{\psi}(y)\gamma^\mu - h\varphi(y)\bar{\psi}(y) = 0\,. \tag{4.10}$$

Multiplying this equation with $\psi(x)$ from the left completes the time evolution of $F_\psi(x,y)$ by determining the behaviour of y coordinates.

The starting point of the mode-function expansion is a Fourier expansion of the fermionic field operator,

$$\psi(t,\mathbf{x}) = \int\frac{d^3p}{(2\pi)^3}\sum_s\Big(b_s(\mathbf{p})\Phi^u_s(t,\mathbf{x},\mathbf{p}) + d^\dagger_s(\mathbf{p})\Phi^v_s(t,\mathbf{x},-\mathbf{p})\Big)\,. \tag{4.11}$$

The fermionic ladder operators $b_s(\mathbf{p})$ for particles and $d_s(\mathbf{p})$ for antiparticles are used here in the framework of canonical quantization, where the spinor index s runs from 1 to 2. These operators are characterized by their anti-commutators

$$\begin{aligned}\left\{b_s(\mathbf{p}), b^\dagger_{s'}(\mathbf{q})\right\} &= (2\pi)^3\delta_{ss'}\delta(\mathbf{p}-\mathbf{q})\,, &(4.12)\\ \left\{d_s(\mathbf{p}), d^\dagger_{s'}(\mathbf{q})\right\} &= (2\pi)^3\delta_{ss'}\delta(\mathbf{p}-\mathbf{q})\,, &(4.13)\end{aligned}$$

while all other possible anti-commutators (e.g. of the form $\{b,b\}$, $\{b^\dagger,b^\dagger\}$, $\{b^\dagger,d\}$ or $\{b,d^\dagger\}$), vanish. The expectation values for the non-vanishing commutators of the ladder operators are parametrized as

$$\begin{aligned}\left\langle\left[b_s(\mathbf{p}), b^\dagger_{s'}(\mathbf{q})\right]\right\rangle &= (2\pi)^3\delta_{ss'}\delta(\mathbf{p}-\mathbf{q})\,(1-2n^s_+(\mathbf{p}))\,, &(4.14)\\ \left\langle\left[d_s(\mathbf{p}), d^\dagger_{s'}(\mathbf{q})\right]\right\rangle &= (2\pi)^3\delta_{ss'}\delta(\mathbf{p}-\mathbf{q})\,(1-2n^s_-(\mathbf{p}))\,. &(4.15)\end{aligned}$$

Here $n_\pm^s(\mathbf{p})$ denote initial occupation numbers of particles and antiparticles of a given spin and spatial momentum. The central part of the expansion are the time-dependent mode-functions $\Phi_s^u(t,\mathbf{x},\mathbf{p})$ and $\Phi_s^v(t,\mathbf{x},\mathbf{p})$, which have to be initialized with

$$\Phi_s^u(t_0,\mathbf{x},\mathbf{p}) = u_s(\mathbf{p})e^{-i\mathbf{p}\mathbf{x}}\ , \quad \Phi_s^v(t_0,\mathbf{x},\mathbf{p}) = v_s(\mathbf{p})e^{-i\mathbf{p}\mathbf{x}}\,. \tag{4.16}$$

The eigenspinors $u_s(\mathbf{p})$ and $v_s(\mathbf{p})$ represent particle and antiparticle eigenstates of the Dirac operator. Substituting (4.11) into the equation of motion for $\psi(x)$ (Eq. (4.8)), one observes that every mode function has to satisfy

$$\left[i\partial_\mu\gamma^\mu - h\varphi(x)\right]\Phi_s^{u/v}(x,\mathbf{p}) = 0\,. \tag{4.17}$$

After the time evolution of $\Phi_s^{u/v}(x,\mathbf{p})$ has been calculated, observables can be constructed using the expansion (4.11). For the evaluation of the expectation values one has to use properties of the initial state such as

$$\left\langle b_i^\dagger(\mathbf{p})b_i(\mathbf{p})\right\rangle = n_i^u(t=0,\mathbf{p})\,, \qquad \langle b_s(\mathbf{p})\rangle = 0\,, \qquad \langle b_s^\dagger(\mathbf{p})\rangle = 0\,, \tag{4.18}$$

and similarly for d_i.

The statistical two-point function reads in terms of mode functions

$$\begin{aligned} F_\psi(x,y) &= \frac{1}{2}\int\frac{d^3p}{(2\pi)^3}\sum_s\Big(\left\langle b_ib_i^\dagger - b_i^\dagger b_i\right\rangle\Phi_s^u(x,\mathbf{p})\bar\Phi_s^u(y,\mathbf{p}) \\ &\quad +\left\langle d_i^\dagger d_i - d_id_i^\dagger\right\rangle\Phi_s^v(x,\mathbf{p})\bar\Phi_s^v(y,\mathbf{p})\Big) \\ &= \int\frac{d^3p}{(2\pi)^3}\sum_s\left(\frac{1}{2} - n_{in,s}^u(\mathbf{p})\right)\Phi_s^u(x,\mathbf{p})\bar\Phi_s^u(y,\mathbf{p}) \\ &\quad +\int\frac{d^3p}{(2\pi)^3}\sum_s\left(n_{in,s}^v(\mathbf{p}) - \frac{1}{2}\right)\Phi_s^v(x,\mathbf{p})\bar\Phi_s^v(y,\mathbf{p}). \end{aligned} \tag{4.19}$$

Here the subscript ”in” stresses the fact that the particle numbers appearing here are evaluated at the initial time. Similarly, we can also calculate the fermion contribution to the energy density of the system $\langle H_D(x)\rangle$ with the Dirac Hamiltonian $H_D = -i\gamma^0\gamma^i\partial_i + \gamma^0 m$ and any other observable $O(x)$ of interest by a summation over the mode functions: $\sum_i F_i\bar\Phi_i O(x)\Phi_i$, where the index i represents the momentum, spin and charge of the mode, the summation over the index i represents the momentum integral as well as the sum over spin and charge modes, and F_i depends on $n_{in,i}^u$ and $n_{in,i}^v$, similarly to (4.19).

The advantage of this method is that it is exact without further approximations and involves no additional ensemble average as needed for the male/female approach, which will be presented in the next section. The great disadvantage, which so far had limited its applicability to lower-dimensional systems, is the requirement to simulate a mode function for every possible combination of space and momentum. If implemented on a lattice, as is described in the following, the mode-function method leads to prohibitively high computational costs on bigger lattices.

4.2. Male/female fermions

In the following, we concentrate on a stochastic approach which is a low-cost alternative to the mode functions expansion introduced before. For a lattice computation in d spatial dimensions and N lattice sites in every direction there are in total N^{2d} mode functions that have to be simulated. This means that e.g. in three spatial dimensions the update of the fermionic spinor fields at every time step as well as the readout of quantities like energy or particle number are decelerated by the huge memory requirement (scaling like N^6) and the need for large loops over all momenta and grid points. The core idea of the male/female method is to reduce these difficulties by decreasing the amount of functions which are evolved in time [23]. In practice, instead of simulating all momenta at every point in space, we use a stochastic ensemble which should correctly reproduce the relevant elements of the full original ensemble consisting of mode functions. We start again with the initial field $\psi(t_0, \mathbf{x})$ at initial time $t = t_0$ and write it for isotropic and homogeneous initial conditions as

$$\psi(t_0, \mathbf{x}) = \int \frac{d^3p}{(2\pi)^3} \sum_s \left(b_s(\mathbf{p}) u_s(\mathbf{p}) e^{-i\mathbf{p}\mathbf{x}} + d_s^\dagger(\mathbf{p}) v_s(-\mathbf{p}) e^{i\mathbf{p}\mathbf{x}} \right). \tag{4.20}$$

Here $b_s(\mathbf{p})$ and $d_s(\mathbf{p})$ are the annihilation operators at initial time as defined in Sec. 4.1. In order to evaluate $F_\psi(x, y)$ without treating these operators explicitly, we utilize the ideas proposed in [23] to rewrite the statistical propagator using a stochastic approach in terms of so-called ”male” and ”female” spinor fields $\psi_M(x)$ and $\psi_F(x)$:

$$F_\psi(x, y) = \langle \psi_M(x) \bar{\psi}_F(y) \rangle_{\text{sto}} = \langle \psi_F(x) \bar{\psi}_M(y) \rangle_{\text{sto}}. \tag{4.21}$$

This procedure of expressing the time evolution of $F_\psi(x, y)$ in terms of $\psi_M(x)$ and $\psi_F(y)$, is applicable since the equations of motion for the fermions are linear [23, 7, 89, 90, 91], a property we already used to derive equations of motion for the statistical propagator in the last section. The last equation shows that the roles of ”male” and ”female” fields are interchangeable. The notation $\langle \ldots \rangle_{\text{sto}}$ emphasizes that in this case the average is performed with respect to a stochastic ensemble of male/female pairs. Additionally, one requires that both of the stochastic spinors obey the Dirac-like equation of motion in accordance to (4.8):

$$\left[i\partial_\mu \gamma^\mu - h\varphi_{\text{cl}}(x) \right] \psi_g(x) = 0. \tag{4.22}$$

The index g (gender) distinguishes here between M (male) and F (female) fields. To reproduce the initial configuration of $F_\psi(x, y)$ in terms of ψ_M and ψ_F the latter are initialized as

$$\psi_{M,F}(t_0, \mathbf{x}) = \int \frac{d^3p}{(2\pi)^3} \frac{e^{-i\mathbf{p}\mathbf{x}}}{\sqrt{2}} \sum_s \left(\xi_s(\mathbf{p}) u_s(\mathbf{p}) \pm \eta_s(\mathbf{p}) v_s(\mathbf{p}) \right). \tag{4.23}$$

So the only difference between ”male” and ”female” spinors is the sign in front of the antiparticle component. Here $\xi_s(\mathbf{p})$ and $\eta_s(\mathbf{p})$ are random numbers coming from a Gaussian distribution which are used to simulate the expectation values of products of the ladder operators $b_s(\mathbf{p})$ and $d_s(\mathbf{p})$. Their non-vanishing correlators are linked to initial occupation numbers

$$\begin{aligned} \langle \xi_s(\mathbf{p}) \xi^*_{s'}(\mathbf{q}) \rangle_{\text{sto}} &= (2\pi)^3 \delta_{ss'} \delta(\mathbf{p}-\mathbf{q}) \, (1 - 2n^s_+(\mathbf{p}))\,, \qquad (4.24) \\ \langle \eta_s(\mathbf{p}) \eta^*_{s'}(\mathbf{q}) \rangle_{\text{sto}} &= (2\pi)^3 \delta_{ss'} \delta(\mathbf{p}-\mathbf{q}) \, (1 - 2n^s_-(\mathbf{p}))\,. \qquad (4.25) \end{aligned}$$

To realize these correlations in a numerical simulation, one has to average over many pairs of ”male” and ”female” fields, but of course each of them has to be evolved in time separately. If the number of pairs is sufficiently large, the result will converge to the physical correlator. Later we will discuss how many male/female pairs are actually required in practice.

Bilinears such as $F_\psi(x,y)$ are computed by combining spinors of both genders. It is illustrative to compute the initial $F_\psi(x^0,y^0,\mathbf{p})|_{x^0=y^0=t_0}$ in terms of operator-valued fields $\psi(x)$ at initial time and the same quantity from ψ_M and ψ_F. Since both approaches are consistent, both calculations yield the same result, which reads for symmetric occupation numbers $n_\pm(\mathbf{p}) = n_\pm(-\mathbf{p})$:

$$F_\psi(x^0,y^0,\mathbf{p})|_{x^0=y^0=t_0} = \frac{1}{2}\sum_s \Big[(1-2n^s_+(\mathbf{p}))\, u_s(\mathbf{p})\bar{u}_s(\mathbf{p}) - (1-2n^s_-(\mathbf{p}))\, v_s(\mathbf{p})\bar{v}_s(\mathbf{p}) \Big]\,. \qquad (4.26)$$

4.3. Discretization

Lattice discretization of fermions is considerably more problematic than that of bosons. Here we will mention the cause of the inherent problems and describe some commonly applied solutions relevant for our applications. In real-time simulations the difference between bosonic and fermionic discretization lies in the order of derivatives appearing in the action. Instead of second-order for bosons we are now dealing with a symmetric first-order derivative. One should restrain from using forward or backward discretizations of the first-order derivatives inside the fermionic equations of motion because this would violate the hermiticity of the corresponding Hamiltonian. In 3.1 the finite difference approximations for derivatives have been listed together with the corresponding lattice momentum definitions. For fermionic degrees of freedom the straightforward discretization with

$$\psi'(x) = \frac{\psi(x+a_i) - \psi(x-a_i)}{2a_i} \qquad (4.27)$$

and corresponding lattice momenta $\bar{p}_i = \frac{\sin(p_i a_s)}{a_s}$ (remember, $p_i = 2\pi n_i/(Na_s)$ and $n_i = 0,\ldots,N-1$) is known to cause so-called fermion doublers [92]. This issue can be easily understood by looking at the free relativistic dispersion relation in terms of discretized fermionic momenta:

$$\omega_\psi(p_i) = \sqrt{m_\psi^2 + \sum_{i=1}^{3} \bar{p}_i^2} = \sqrt{m_\psi^2 + \frac{1}{a_s^2} \sum_{i=1}^{3} \sin^2(p_i a_s)}\,. \tag{4.28}$$

Setting for a moment all n_2 and n_3 to zero, we see that in the now one-dimensional dispersion relation the boundaries of our Brillouin zone would lie at $p_1 = \pi$ and $p_1 = -\pi$, representing positive and negative lattice momenta with the highest absolute value. Based on the one-dimensional continuum dispersion $\omega(p_1) = \sqrt{m_\psi^2 + p_1^2}$ we would expect that

$$\omega(p_1 = \pm\pi) > \omega(p_1 = 0) = m_\psi\,. \tag{4.29}$$

But because of the periodicity of $\bar{p}_i$ the discretized dispersion relation does not distinguish between $p_i = 0$ and $p_i = \pm\pi$, assigning all of them the lowest possible energy value

$$\omega_\psi(p_1 = \pm\pi) \overset{!}{=} \omega_\psi(p_1 = 0) = m_\psi\,. \tag{4.30}$$

The conclusion is that in a naive fermionic discretization particles with high lattice momenta receive low energy values, contrary to the behaviour in the continuum theory. In Fig. 4.1 the occurring situation is presented graphically. Since every energy minimum is associated with a pole in the fermion propagator, it becomes obvious that in every space-time direction the number of degrees of freedom is doubled such that in a numerical simulation we get 2^{d+1} fermions instead of intended one. Included in this counting are also the temporal doublers which arise in a similar manner because high frequency oscillations become associated to low energy values in this type of discretization. A way to address this problem, similar to the one commonly employed in Euclidean lattice gauge theory, is to introduce a spatial Wilson term W into the equation of motion (4.22):

$$\left[i\partial_\mu\gamma^\mu + W - h\varphi(x)\right]\psi_g(x) = 0\,. \tag{4.31}$$

A standard choice would be

$$W\psi_g(x) = \frac{r a_s}{2} \triangle_x \psi_g(x)\,, \tag{4.32}$$

where we set $r = 1$ from now on and use the following discretization of the Laplacian:

$$\triangle_x \psi_g(x) = \sum_{i=1}^{3} \frac{\psi_g(x + a_i) + \psi_g(x - a_i) - 2\psi_g(x)}{a_s^2}\,. \tag{4.33}$$

This leads to a momentum-dependent contribution to the fermionic dispersion relation:

$$\omega(\mathbf{p}) = \sqrt{m_\psi^2 + \bar{p}_i\bar{p}^i + a_s m_\psi \mathbf{p}_{\mathrm{lat}}^2 + \frac{a_s^2}{4}\mathbf{p}_{\mathrm{lat}}^4}\,. \tag{4.34}$$

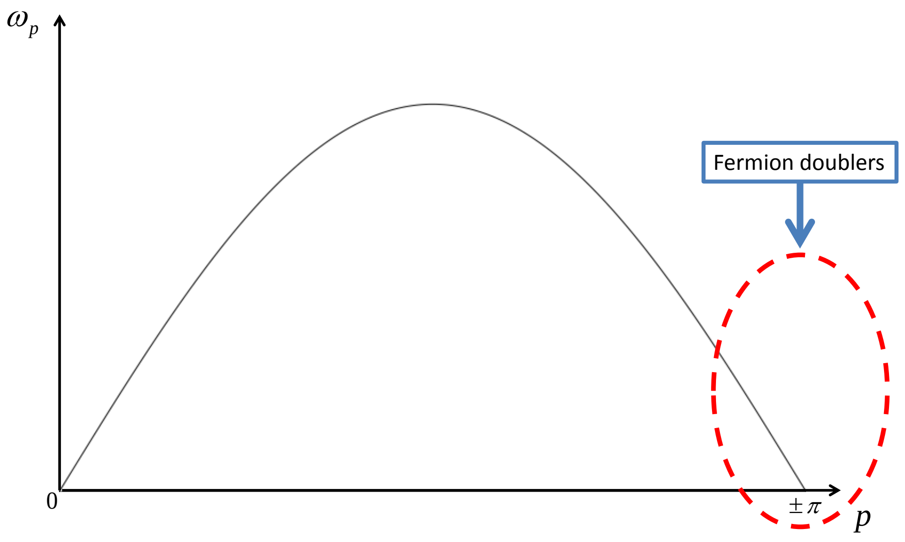

Figure 4.1.: Sketch of the lattice dispersion relation for naive fermion discretization.

This ensures that only low-momentum excitations show a low-energy dispersion relation [22, 7]. One observes that the additional contributions from the Wilson term vanish in the continuum limit $a_s \to 0$. However, we find that a faster approach to the continuum limit is achieved by replacing $W \to W_{PS}$ defined as

$$W_{PS}\psi_g(x) = i\gamma_5 \frac{ra_s}{2} \triangle_x \psi_g(x). \tag{4.35}$$

Here the subscript PS means pseudoscalar in contrast to the standard scalar Wilson term. The pseudoscalar Wilson term also leads to a (modified) momentum dependent contribution to the fermionic dispersion relation

$$\omega(\mathbf{p}) = \sqrt{m_\psi^2 + \bar{p}_i\bar{p}^i + \frac{a_s^2}{4}\mathbf{p}_{\text{lat}}^4}. \tag{4.36}$$

This illustrates that W_{PS} eliminates the $O(a_s)$ contribution to the dispersion relation, which will be particularly advantageous for our out-of-equilibrium setup where the effective fermion mass will be time-dependent.[1] Contrary to the scalar Wilson term, W_{PS} ensures in such cases that the only time-dependent contribution to the dispersion relation remains m_ψ^2. In App. C we give the lattice form of the Dirac eigenspinors corresponding to this additional term, they are used for all 3 + 1 dimensional computations presented in this work. We do not include a temporal Wilson term as this would turn a Dirac equation into a second order differential equation in time. The temporal doublers are avoided if only

---

[1] A related construction used in lattice gauge theory is known as twisted mass fermions [93].

the physical modes are initialized and if the temporal lattice spacing is chosen to be much smaller than the spatial lattice spacing $a_t \ll a_s$ [22, 23, 89, 90, 91].

Chapter 5.

Scalar Bosons with Fermions

In this chapter, we will start our investigations of fermion production from two distinct instability scenarios in scalar bosonic theories. At first, we study the real-time dynamics of fermions coupled to scalar fields in a linear sigma model, which is often employed in the context of preheating after inflation or as a low-energy effective model for quantum chromodynamics. We find a dramatic amplification of fermion production in the presence of highly occupied bosonic quanta for weak as well as strong couplings. For this, we consider the range of validity of different methods: lattice simulations with male/female fermions [23], the mode functions approach [22] and the quantum 2PI effective action [85] with its associated kinetic theory. For strongly coupled fermions we find a rapid approach to a Fermi-Dirac distribution with time-dependent temperature and chemical potential parameters, while the bosons are still far from equilibrium.

In the second study, we concentrate on tachyonic preheating in a model with Yukawa interactions between fermions and scalar fields. We make an explicit comparison with previously obtained analytic predictions for production of fermions with dynamically generated mass and show that bosonic fluctuations drastically increase the number of particles produced during the first stages of (p)reheating. Our numerical results indicate that leading order approximations fail to capture the effects responsible for production of massive fermions even at moderate values of the effective coupling. We discuss the features of emergent particle distributions and comment on the relevance of these results for cosmological applications.

5.1. Amplified fermion production from bosonic overpopulation

We start with the presentation of our results for fermion production from instabilities in a 3 + 1 dimensional scalar linear-sigma model. Taking advantage of various computational we discuss their range of applicability in detail. As our main result, we confirm the dramatic amplification of fermion production in the presence of highly occupied bosons that was first pointed out in Ref. [7]. This amplification is discussed in terms of the emerging effective coupling ξ while the results are extended to the strong coupling regime.

It turns out that the efficient male/female lattice approach accurately converges to the exact mode functions result for the available lattice sizes. Our study shows the strength of the male/female method to address physical questions for large volumes [7, 94, 95, 89, 90, 91], where the mode function approach becomes computationally intractable. For weak couplings, we find that the lattice simulation results agree well with those obtained from the quantum 2PI effective action, emphasizing the ability of the lattice approach to describe genuine quantum phenomena.

Applying an improved lattice discretization with a pseudoscalar Wilson term, we accurately resolve for the first time the high-momentum behavior of particle number distributions. For weak couplings this reveals a power-law behavior above a characteristic momentum. For strongly coupled fermions, we find a rapid approach to a quasi-thermal Fermi-Dirac distribution with time-dependent temperature and chemical potential parameters. Remarkably, this happens while the bosons are still showing turbulent behavior far from equilibrium.

We proceed as follows: In Sec. 5.1.1 and 5.1.2 we describe the model we use to simulate fermion production and elaborate on details of our lattice formulation, our choice of initial conditions and renormalization procedure. In Sec. 5.1.3 we demonstrate the convergence of the male/female method towards the exact mode functions results. In Sec. 5.1.4 consequences of neglecting higher-order quantum fluctuations as well as details of our 2PI implementation are discussed. Moreover, we present numerical evidence for applicability of 2PI and the degree of agreement between 2PI and lattice simulations. In Sec. 5.1.5 and 5.1.6 we finally arrive at our results for fermion production from parametric resonance at strong and weak coupling. We summarize and conclude in Sec. 5.1.7.

5.1.1. Model and initial conditions

We consider a relativistic quantum field theory of coupled bosonic and fermionic degrees of freedom. It describes a generic linear sigma model for a $N_s = 4$ component scalar field $(\sigma, \vec{\pi})$ with self-coupling λ. The scalars interact via a Yukawa coupling g with $N_f = 2$ flavors of massless Dirac fermions ψ_i with flavor index i. The Lagrangian density is given by

$$\begin{aligned} \mathcal{L} &= \frac{1}{2}\left(\partial_\mu\sigma\,\partial^\mu\sigma + \partial_\mu\vec{\pi}\,\partial^\mu\vec{\pi}\right) - \frac{1}{2}m^2\left(\sigma^2 + \vec{\pi}^2\right) \\ &- \frac{\lambda}{4!N_s}\left(\sigma^2 + \vec{\pi}^2\right)^2 + \bar{\psi}\left(i\,\partial_\mu\gamma^\mu\right)\psi - \frac{g}{N_f}\bar{\psi}\left(\sigma + i\gamma_5\vec{\tau}\cdot\vec{\pi}\right)\psi, \end{aligned} \tag{5.1}$$

with Dirac matrices γ^μ ($\mu = 0, \ldots, 3$), $\gamma^5 = \gamma_5 = i\gamma^0\gamma^1\gamma^2\gamma^3$ and $\bar{\psi} \equiv \psi^\dagger\gamma^0$. We denote here the Pauli matrices by $\vec{\tau}$.

The equal-time anti-commutation relations for the fermions are encoded in the spectral function

$$\rho_{\psi,ij}(x,y) \equiv i\langle\{\psi_i(x), \bar{\psi}_j(y)\}\rangle \tag{5.2}$$

as

$$\gamma^0 \rho_{\psi,ij}(x,y)|_{x^0=y^0} = i\delta(\mathbf{x}-\mathbf{y})\,\delta_{ij} \tag{5.3}$$

with $\{A, B\} \equiv AB + BA$. Correspondingly, the boson commutation relations are encoded in

$$\rho_\sigma(x,y) \equiv i\langle[\sigma(x), \sigma(y)]\rangle \tag{5.4}$$

with

$$\partial_{x^0}\rho_\sigma(x,y)|_{x^0=y^0} = \delta(\mathbf{x}-\mathbf{y}) \tag{5.5}$$

for $[A, B] \equiv AB - BA$. Equivalently, one can define spectral functions for the $\vec{\pi}$ fields, with vanishing commutators between different fields. The brackets $\langle A\rangle \equiv \mathrm{tr}(\varrho_0 A)$ denote the trace over a normalized initial density matrix ϱ_0, which specifies the initial conditions at time t_0. Here we will choose Gaussian initial conditions, where ϱ_0 is completely determined by one- and two-point correlation functions at t_0. This class of initial conditions will allow us to study, in particular, particle production from non-equilibrium instabilities as will be discussed below. We emphasize that a choice of initial conditions does not represent an approximation to the dynamics and irreducible higher n-point correlation functions will build up for times larger than t_0 because of the interactions in (5.1). We restrict ourselves to spatially homogeneous initial conditions such that we can Fourier transform with respect to spatial variables. With $\langle\psi_i(x)\rangle = 0$ the one-point function for the σ-field

$$\phi(x^0) \equiv \langle\sigma(x)\rangle \tag{5.6}$$

at initial time is specified by an initial field amplitude ϕ_0 as

$$\phi(t_0) = \phi_0 \quad , \quad \partial_{x^0}\phi(x^0)|_{x^0=t_0} = 0\,. \tag{5.7}$$

For the initial $\vec{\pi}$ fields we take

$$\langle\vec{\pi}(x)\rangle|_{x^0=t_0} = 0 \quad , \quad \langle\partial_{x^0}\vec{\pi}(x)\rangle|_{x^0=t_0} = 0\,. \tag{5.8}$$

It remains to specify the two-point correlation functions. Apart from the above spectral functions, whose initial conditions are fixed by the equal-time relations at initial time, we also have to give the respective commutator expectation values for the fermions and anti-commutators for the bosons. These so-called statistical two-point functions are [6]

$$F_{\psi,ij}(x,y) \equiv \frac{1}{2}\langle[\psi_i(x), \bar{\psi}_j(y)]\rangle\,, \tag{5.9}$$

$$F_\sigma(x,y) = \frac{1}{2}\langle\{\sigma(x), \sigma(y)\}\rangle - \langle\sigma(x)\rangle\langle\sigma(y)\rangle \tag{5.10}$$

and, similarly, the anti-commutator expectation value $F_\pi(x,y)$ for each of the $\vec{\pi}$ components. Their spatial Fourier modes at initial time are chosen as

$$F_{\psi,ij}(x^0,y^0,\mathbf{p})|_{x^0=y^0=t_0} = \frac{m_\psi - \not{p}}{\omega_\psi(\mathbf{p})}\left(\frac{1}{2} - n_\psi(\mathbf{p})\right)\delta_{ij}\,. \tag{5.11}$$

with $\omega_\psi(\mathbf{p}) = \sqrt{m_\psi^2 + \mathbf{p}^2}$. Here the effective fermion mass m_ψ is given by $g\phi_0/2$ at initial time and $n_\psi(\mathbf{p}) = 0$ for vacuum initial conditions. For the initial boson correlators we take

$$\begin{aligned} F_\sigma(x^0,y^0,\mathbf{p})|_{x^0=y^0=t_0} &= \frac{1}{\omega(\mathbf{p})}\left(\frac{1}{2} + n(\mathbf{p})\right), \\ \partial_{x^0} F_\sigma(x^0,y^0,\mathbf{p})|_{x^0=y^0=t_0} &= 0\,, \\ \partial_{x^0}\partial_{y^0} F_\sigma(x^0,y^0,\mathbf{p})|_{x^0=y^0=t_0} &= \omega(\mathbf{p})\left(\frac{1}{2} + n(\mathbf{p})\right) \end{aligned} \tag{5.12}$$

with $\omega(\mathbf{p}) = \sqrt{m^2 + \mathbf{p}^2}$ and $n(\mathbf{p}) = 0$. We choose the same initial conditions for F_σ and for F_π. Initial two-point functions involving different fields are taken to vanish. The above completely specifies the initial value problem for our model.

To extract information about particle numbers from numerical simulations it is convenient to define bosonic and fermionic effective particle numbers, both of which are in general not conserved for an interacting system out of equilibrium.[1] For bosons the particle number is associated to the equal-time statistical propagator $F_\sigma(t,t,\mathbf{p})$ and quasi-particle energy $\epsilon_\sigma(t,\mathbf{p})$ according to [6]

$$\begin{aligned} \epsilon_\sigma(t,\mathbf{p}) &= \sqrt{\frac{\partial_t\partial_{t'}F_\sigma(t,t',\mathbf{p})\,|_{t=t'}}{F_\sigma(t,t,\mathbf{p})}}\,, \\ n_\sigma(t,\mathbf{p}) &= F_\sigma(t,t,\mathbf{p})\epsilon_\sigma(t,\mathbf{p}) - \frac{1}{2} \end{aligned} \tag{5.13}$$

and equivalently for the $\vec{\pi}$ fields. Plugging the above initial values into these definitions confirms that the vacuum we start from contains no particles according to this definition.

To discuss properties of $F_\psi(t,\mathbf{p})$, we consider its scalar, pseudoscalar and vector components:

$$F_S(t,\mathbf{p}) = \frac{1}{4}\mathrm{Tr}\left(F_\psi(t,t,\mathbf{p})\right)\,, \tag{5.14}$$

$$F_V^i(t,\mathbf{p}) = \frac{1}{4}\mathrm{Tr}\left(\gamma^i F_\psi(t,t,\mathbf{p})\right)\,, \tag{5.15}$$

---

[1] Of course, there is no unique definition of particle number in an interacting theory if the number is not conserved. It is also nowhere needed in our calculations and only used for interpretation of the results. We use standard definitions that are typically employed to connect to discussions in the context of Boltzmann equations.

$$F_{PS}(t,\mathbf{p}) = \frac{1}{4}\mathrm{Tr}\left(\gamma_5 F_\psi(t,t,\mathbf{p})\right) , \tag{5.16}$$

where the trace acts in Dirac space. The flavour indices are omitted here, because we restrict ourselves to initial conditions which are diagonal in flavour space and thus consider only flavour-averaged quantities. Each of these quantities can be used to define an effective particle number, enabling us to construct $n_\psi(t,\mathbf{p})$ from different combinations of $F_S(t,\mathbf{p})$, $F_{PS}(t,\mathbf{p})$ and $F_V^i(t,\mathbf{p})$. Here we follow [7, 85, 96] and employ

$$n_\psi(t,\mathbf{p}) = \frac{1}{2} - \frac{p_i F_V^i(t,\mathbf{p}) + m_\psi(t,\mathbf{p}) F_S(t,\mathbf{p})}{\sqrt{\mathbf{p}^2 + m_\psi^2(t,\mathbf{p})}} . \tag{5.17}$$

The time dependence of the effective fermion mass results from the dynamical macroscopic field $\phi(t)$.

5.1.2. Real-time lattice approach

Fermions are never largely occupied and are, in this respect, genuinely quantum. However, fermions appear quadratically in the Lagrangian (5.1) as is also the case for theories like quantum chromodynamics or electrodynamics.[2] Therefore, their dynamics can be solved without further approximations for given classical bosonic field configuration.

The procedure is to integrate out the fermions from the path integral to get the classical evolution equation for the bosons. This equation then depends on the fermion currents, represented by fermion two-point correlation functions. The evolution for these fermion correlation functions is obtained from the original Lagrangian, where the fermion fields appear quadratically. This gives a Dirac-like equation for the fermion correlation functions, which is coupled to inhomogeneous classical Bose fields. The description is very suitable for initial value problems and, below, we will find that it accurately describes the quantum dynamics including loop corrections for very non-trivial situations where the latter can be computed using 2PI effective action techniques.

The above model (5.1) leads to the equations of motion

$$\left(\Box_x + m^2\right)\sigma_{\mathrm{cl}}(x) + \frac{\lambda}{4!}\left(\sigma_{\mathrm{cl}}^2 + \vec{\pi}_{\mathrm{cl}}^2\right)\sigma_{\mathrm{cl}}(x) - \frac{g}{2}\mathrm{Tr}\left(F_\psi(x,x)\right) = 0 \tag{5.18}$$

and

$$\left(\Box_x + m^2\right)\vec{\pi}_{\mathrm{cl}}(x) + \frac{\lambda}{4!}\left(\sigma_{\mathrm{cl}}^2 + \vec{\pi}_{\mathrm{cl}}^2\right)\vec{\pi}_{\mathrm{cl}}(x) - \frac{ig}{2}\mathrm{Tr}\left(F_\psi(x,x)\gamma_5\right) = 0 \tag{5.19}$$

for classical bosonic fields $\sigma_{\mathrm{cl}}(x)$ and $\vec{\pi}_{\mathrm{cl}}(x)$. Here the trace acts in flavour and Dirac space. These evolution equations depend on the fermion two-point correlator (5.9). For

---

[2] For all practical purposes, it can always be achieved that the fermions appear quadratically in the Lagrangian at the expense of introducing extra bosonic field degrees of freedom.

given classical bosonic fields, the equation of motion for the spinor field $\psi_i(x)$ reads:

$$\left[i\partial_\mu \gamma^\mu - \frac{g}{2} \left(\sigma_{\mathrm{cl}}(x) + i\gamma_5 \vec{\tau}\vec{\pi}_{\mathrm{cl}}(x) \right) \right] \psi_i(x) = 0. \tag{5.20}$$

By multiplying from the right with $\bar{\psi}_j(y)$ we obtain the evolution equation for the fermion commutator in the linear sigma model. Similar to Eq. (4.9) the Dirac-like equation of motion for the expectation value of the commutator (5.9) is given by:

$$\left[i\partial_{x,\mu} \gamma^\mu - \frac{g}{2} \left(\sigma_{\mathrm{cl}}(x) + i\gamma_5 \vec{\tau}\vec{\pi}_{\mathrm{cl}}(x) \right) \right] F_{\psi,ij}(x,y) = 0\,. \tag{5.21}$$

In the male/female approach both of the stochastic spinors obey the same Dirac-like equation of motion in accordance to (5.20) and (4.8):

$$\left[i\partial_\mu \gamma^\mu - \frac{g}{2} \left(\sigma_{\mathrm{cl}}(x) + i\gamma_5 \vec{\tau}\vec{\pi}_{\mathrm{cl}}(x) \right) \right] \psi_g(x) = 0. \tag{5.22}$$

As already mentioned, the bosonic fields are treated in the classical-statistical approximation, where the fields are evolved in time and space according to (5.18) and (5.19) for initial conditions that are sampled to give the initial values (5.7), (5.8) and (5.12) on average . For each run the coupled system of equations including the one for the fermion two-point function (5.21) with initial condition (5.11) is solved.

Initial conditions on the lattice

At the beginning of each simulation initial conditions have to be specified. For the bosons one has to specify the initial classical fields and derivatives according to (5.7), (5.8) and (5.12) to obtain quantum-like vacuum initial conditions. They are initialized in momentum space from a Gaussian probability distribution centered around zero with standard deviation of $\left(2\sqrt{m^2+\mathbf{p}^2}\right)^{-1/2}$ for the fields and $\left(\sqrt{m^2+\mathbf{p}^2}/2\right)^{1/2}$ for the time derivatives of the fields. In order to realize parametric resonance in quantum field theory the average initial field is homogeneous with amplitude

$$\phi(t=0) = \sigma_0 \sqrt{\frac{6N}{\lambda}}\,, \tag{5.23}$$

where the parameter σ_0 sets the overall scale for our simulations.

Another important property in momentum space is $\sigma(-\mathbf{p}) = \sigma^*(\mathbf{p})$ and similarly for $\vec{\pi}$, which is required to get real-valued fields in position space. This is achieved by multiplying the real field amplitudes with a random phase factor $e^{i\alpha(\mathbf{p})}$ with $\alpha(\mathbf{p}) = -\alpha(-\mathbf{p})$ and $\alpha = 0$ for $p_i = 0$ and $p_i = \pi/a_s$. The same procedure using another random phase factor $e^{i\beta(\mathbf{p})}$ is applied to get real-valued field derivatives w.r.t. time in position space. Due to the fact that in our approach the scalar fields are classical-statistical we try to minimize possible effects of UV divergent contributions by initializing the quantum-like vacuum correlators only up to a finite momentum $\Lambda < |\mathbf{p}|_{\mathrm{lat}}^{\mathrm{max}}$, with Λ being higher than all of the momentum modes which become relevant during the simulated time.

For the male/female fermion approach, initial values are given in terms of $\psi_M(x)$ and $\psi_F(x)$ at $t = t_0 = 0$. They are directly linked to complex random numbers, which have to fulfill correlator relations of the fermionic ladder operators (4.24). To start with vacuum initial conditions we set all particle numbers to zero. These correlator relations are implemented numerically through complex valued $\xi_s(\mathbf{p}) = A_s(\mathbf{p})e^{i\varphi_s(\mathbf{p})}$ and $\eta_s(\mathbf{p}) = B_s(\mathbf{p})e^{i\theta_s(\mathbf{p})}$ with real amplitudes $A_s(\mathbf{p})$ and $B_s(\mathbf{p})$ coming from a Gaussian distribution and random phases $\varphi_s(\mathbf{p})$ and $\theta_s(\mathbf{p})$ to ensure that all mixed correlators vanish. Having chosen a symmetric finite difference approximation for the first time derivative, we have to specify $\psi_M(x)$ and $\psi_F(x)$ not only at $t = 0$ but also at $t = -a_t$, which is done by an evolution of the free fields according to

$$\psi_{M,F}(t=0,\mathbf{p}) = e^{-i\gamma_0\omega(\mathbf{p})a_t}\psi_{M,F}(t=-a_t,\mathbf{p}). \tag{5.24}$$

The initial statistical propagator $F_\psi(x,y)|_{x^0=y^0=0}$, which solves the free Dirac equation at $t = 0$, reads on the lattice in the presence of the employed Wilson term as follows:

$$F_\psi(x^0=0,y^0=0,\mathbf{p}) = \frac{m_\psi - \gamma^i\bar{p}_i - i\gamma_5\frac{a_s}{2}\mathbf{p}_{\mathrm{lat}}^2}{2\omega(\mathbf{p})}\left(1-2n_\psi(\mathbf{p})\right). \tag{5.25}$$

Likewise, the fermion occupation number (5.17) is given by

$$n_\psi(t,\mathbf{p}) = \frac{1}{2} - \frac{\bar{p}_iF_V^i(t,\mathbf{p}) + m_\psi(t,\mathbf{p})F_S(t,\mathbf{p}) + i\frac{a_s}{2}\mathbf{p}_{\mathrm{lat}}^2F_{PS}(t,\mathbf{p})}{\sqrt{\bar{p}_i\bar{p}^i + m_\psi^2(t,\mathbf{p}) + \frac{a_s^2}{4}\mathbf{p}_{\mathrm{lat}}^4}}. \tag{5.26}$$

Renormalization

To obtain physically relevant information from our numerical simulations, we have to ensure that the results are insensitive to changes of the finite lattice cut-off $\sim 1/a_s$. In practice the variation of the cutoff-scale in simulations barely exceeds one order of magnitude. Here we consider the leading divergences perturbatively, which we explicitly verified to lead to cutoff insensitive numerical results for a variation of the spatial lattice spacing in the range $a_s\sigma_0 = 0.1 - 1$. For our model this concerns the quadratically running scalar mass terms, where the relevant contributions are coming from the one-loop scalar self-energy corrections displayed in Fig. 5.1. Because of our choice of initial conditions with a non-zero σ-field amplitude (5.7), the dressings of σ and $\vec{\pi}$ masses through vacuum fluctuations are in general different. For given renormalized mass squared m^2, we compute the mass parameters $m_{0,\sigma/\pi}^2$ self-consistently from

$$m_{0,\sigma/\pi}^2 + \Sigma_{0,\sigma/\pi}(m_{0,\sigma}^2, m_{0,\pi}^2) = m^2 \tag{5.27}$$

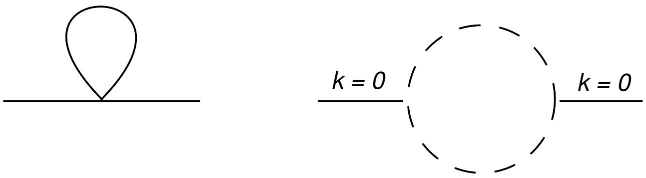

Figure 5.1.: Left: Scalar tadpole. Right: Fermion loop with vanishing external momentum.

using the analytical form of the self-energies displayed in Fig. 5.1:

$$\Sigma_{0,\sigma} = \frac{\lambda}{48}\frac{1}{N^3 a_s^3}\sum_{\mathbf{p}}\left(\frac{3}{\sqrt{m_{0,\sigma}^2 + \mathbf{p}_{\mathrm{lat}}^2}} + \frac{3}{\sqrt{m_{0,\pi}^2 + \mathbf{p}_{\mathrm{lat}}^2}}\right) - g^2\frac{1}{N^3 a_s^3}\sum_{\mathbf{p}}\frac{\bar{p}_i\bar{p}^i + \frac{a_s^2}{4}\mathbf{p}_{\mathrm{lat}}^4}{\left(\bar{p}_i\bar{p}^i + m_\psi^2 + \frac{a_s^2}{4}\mathbf{p}_{\mathrm{lat}}^4\right)^{3/2}}, \tag{5.28}$$

$$\Sigma_{0,\pi} = \frac{\lambda}{48}\frac{1}{N^3 a_s^3}\sum_{\mathbf{p}}\left(\frac{1}{\sqrt{m_{0,\sigma}^2 + \mathbf{p}_{\mathrm{lat}}^2}} + \frac{5}{\sqrt{m_{0,\pi}^2 + \mathbf{p}_{\mathrm{lat}}^2}}\right) - g^2\frac{1}{N^3 a_s^3}\sum_{\mathbf{p}}\frac{\bar{p}_i\bar{p}^i + m_\psi^2}{\left(\bar{p}_i\bar{p}^i + m_\psi^2 + \frac{a_s^2}{4}\mathbf{p}_{\mathrm{lat}}^4\right)^{3/2}}. \tag{5.29}$$

At the beginning of each simulation of the real-time dynamics, these equations are first solved by iteration starting with $m_{0,\sigma/\pi}^2 = m^2$ until convergence is achieved. Then m^2 is replaced by $m_{0,\sigma}^2$ in equation (5.18) and by $m_{0,\pi}^2$ in (5.19).[3]

5.1.3. Comparison of male/female and mode functions approach

The male/female method described above has to converge to the results of the mode function expansion in the limit where the number of male/female pairs is sufficiently large. In practice, the convergence depends on parameters such as the dimension d of space, the number of lattice points N or the value of couplings. In general, simulations employing the mode function expansion are limited to relatively small lattices because the number

---

[3] The Lagrangian (5.1) describes massless fermions. A non-zero mass parameter for the fermions in the Lagrangian would lead to a divergent linear contribution to the bosonic potential requiring an additional renormalization.

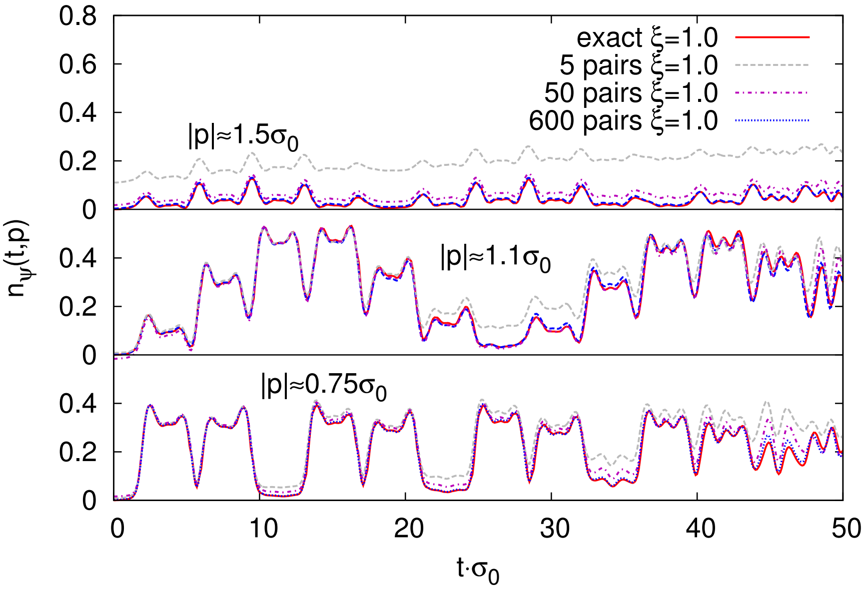

Figure 5.2.: Occupation number of three momentum modes as a function of time and the convergence with increasing number of male/female pairs.

of mode functions increases like N^d for every lattice point. Therefore, the total cost of the simulation increases as N^{2d}. In contrast, the cost for male/female fermion simulations is expected to scale as N^d times the number of male/female pairs. As a consequence, in one spatial dimension the male/female method has no particular advantage over the mode functions approach, as the needed number of pairs is not significantly smaller than the number of mode functions per lattice point. The situation is different in two or three dimensions, where one typically observes reasonable convergence for a much lower number of pairs as compared to the requirements of the full mode function expansion.

To give an explicit example, we compare the time-evolution on a small 16^3 lattice using the full mode function expansion and the male/female method for a varying number of pairs. In the remainder of this work the latter method will then be used on larger lattices to compute results for the analysis of the underlying physics. In Fig. 5.2 the fermion occupation number (5.26) is shown as a function of time for different values of the spatial momentum $\mathbf{p}$. The underlying physical processes will be discussed in detail below. The number of male/female pairs is varied from 5 to 600 for this plot. We clearly observe that both approaches agree to very good accuracy for a sufficiently large number of pairs. The convergence is typically faster for low momentum modes, in agreement with the expectation that self-averaging (which works as an angle average in momentum space) is more efficient for low momenta since the involved characteristic volume is larger.

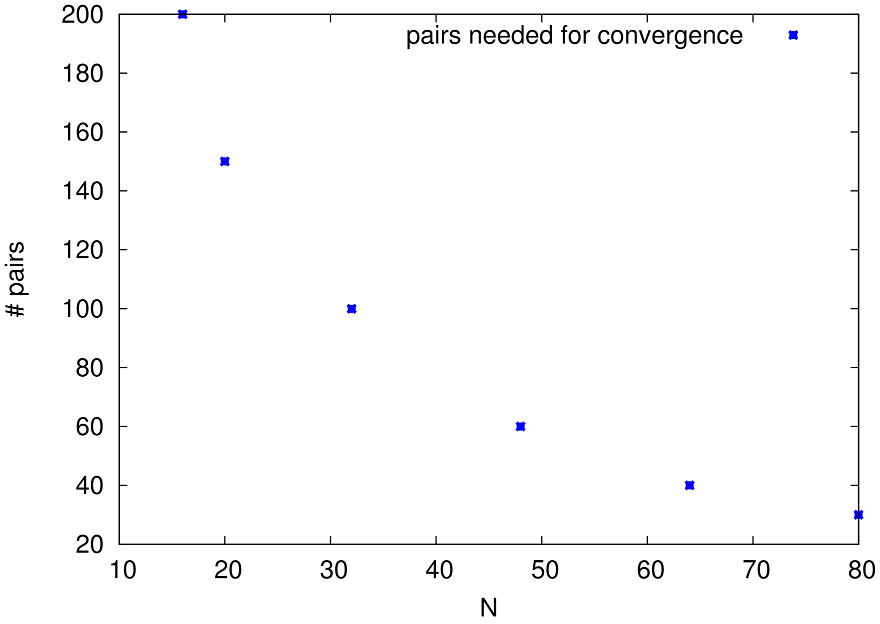

Figure 5.3.: Number of male/female pairs required to achieve convergence as a function of number of lattice sites N in each direction.

For the employed small lattice size in this example we required a relatively high number of pairs. This is expected to change for larger lattices due to enhanced self-averaging. Since a direct comparison with mode function results is impractical for larger lattices, we further investigated the convergence of results as the number of male/female pairs is increased for a given lattice size. Fig. 5.3 shows the number of male/female pairs that are required to achieve convergence of momentum dependent particle spectra with all other parameters, such as simulation time, lattice spacing etc., fixed. One observes that for increasing lattice size the number of pairs can be reduced. Convergence of momentum independent observables like energy density can usually be reached with even lower statistics, because of the full employment of self-averaging for these observables. In general, we find that a larger ultraviolet cutoff or stronger coupling worsen the convergence making, in particular, the study of strongly correlated fermions computationally more expensive than weakly correlated systems.

5.1.4. Validation against quantum field theory

In the previous part we described lattice methods that give a fully non-perturbative description of the dynamics in their range of validity for large bosonic field amplitudes or occupancies. In principle, there are no further approximations in the fermion sector and the lattice description includes the physics of fermion loop corrections to infinite order. However, there are additional procedures to suppress fermion doublers on the lattice using Wilson fermions. It is, therefore, illustrative to validate the lattice description against (continuum) quantum field theory at least in the weak-coupling limit, where this is possible since suitable approximations exist for the latter. The quantum description we employ is based on a resummed large-N expansion to next-to-leading order (NLO) for the bosonic sector and a resummed loop expansion for the fermionic sector of our model [78, 85].

The resummation is efficiently formulated in terms of the two-particle irreducible (2PI) effective action in Minkowski space-time [6]

$$\begin{aligned}\Gamma[\phi, G, G_\psi] &= S[\phi] + \frac{i}{2}\mathrm{Tr}\ln\left(G^{-1}\right) + \frac{i}{2}\mathrm{Tr}\left(G_0^{-1}(\phi)G\right) \\ &- i\mathrm{Tr}\ln\left(G_\psi^{-1}\right) - i\mathrm{Tr}\left(G_{0,\psi}^{-1}G_\psi\right) + \Gamma_2[\phi, G, G_\psi]\,,\end{aligned} \tag{5.30}$$

which includes all quantum corrections if the two-particle irreducible part Γ_2 is known. Here, $\phi(x)$ denotes the field expectation value (5.6) while $G = \mathrm{diag}\{G_\sigma, \vec{G}_\pi\}$ and G_ψ denote the full boson and fermion propagators, which are taken to be diagonal in field index space. The traces involve the sum over field indices as well as space-time integrals. The fields live on a closed time path or Schwinger-Keldysh contour C, which runs forth and back along the real-time axis starting at a given initial time t_0 [6]. The classical part of the action reads

$$S[\phi] = \int_C dt \int d^3x \left(\frac{1}{2}\partial_\mu\phi\,\partial^\mu\phi - \frac{1}{2}m^2\phi^2 - \frac{\lambda}{4!N_s}\phi^4\right), \tag{5.31}$$

while the classical propagators are

$$\begin{aligned}iG_{0,\sigma}^{-1}(x,y;\phi) &= \frac{\delta^2 S}{\delta\phi(x)\delta\phi(y)} \\ &= -\left(\Box + m^2 + \frac{\lambda}{2N_s}\phi^2(x)\right)\delta(x-y)\,, \\ iG_{0,\pi}^{-1}(x,y;\phi) &= -\left(\Box + m^2 + \frac{\lambda}{6N_s}\phi^2(x)\right)\delta(x-y)\,, \\ iG_{0,\psi}^{-1}(\phi) &= \left(i\partial_\mu\gamma^\mu - \frac{g}{2}\phi(x)\right)\delta(x-y)\,.\end{aligned} \tag{5.32}$$

The real-time quantum evolution equations for ϕ, G and G_ψ are obtained from (5.31) by variation

$$\frac{\delta\Gamma[\phi, G, G_\psi]}{\delta\phi(x)} = 0\,, \quad \frac{\delta\Gamma[\phi, G, G_\psi]}{\delta G(x,y)} = 0\,, \quad \frac{\delta\Gamma[\phi, G, G_\psi]}{\delta G_\psi(x,y)} = 0\,. \tag{5.33}$$

They are solved numerically by discretizing the equations on a sphere in spatial momentum space using standard techniques. In particular, this description requires no Wilson term to remove fermion doublers inherent in the above lattice approach.

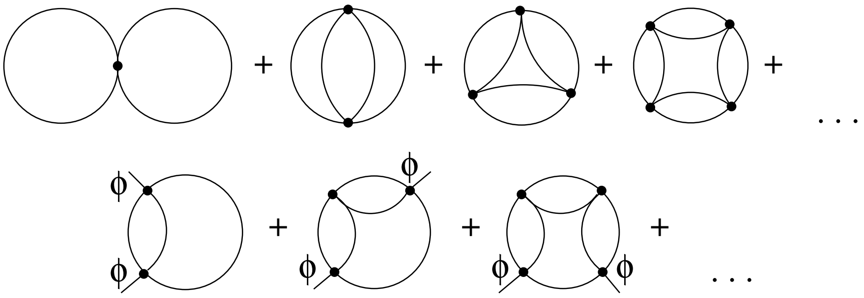

Figure 5.4.: Expansion of Γ_2 to NLO in $1/N$ for the bosonic sector. Solid lines are full boson propagators while external legs correspond to insertions of the macroscopic field ϕ. The dots indicate that we sum up an infinite series of diagrams, with every next diagram having one additional loop in the bubble ring.

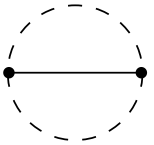

Figure 5.5.: Expansion of Γ_2 to two loops in the fermion sector. A dashed line represents a full fermion propagator.

Our approximation for Γ_2 is depicted graphically in Figs. 5.4 and 5.5. The employed $1/N$ expansion to NLO in the bosonic sector corresponds to summing an infinite series of diagrams [78], while the fermion corrections are taken into account at two-loop order. We will call this approximation "NLO 2PI" in the following. For the comparison, we employ weak couplings $\lambda \ll 1$ and $g \ll 1$. The $1/N$ expansion can describe even non-perturbatively large occupancies of order $1/\lambda$, which will be relevant for the dynamics in the bosonic sector, whereas the occupancies in the fermion sector are strictly limited by Fermi statistics. Of course, the loop expansion of Γ_2 in the fermion sector is not expected to be valid for strong couplings. As a consequence, the quantum results can be used to validate the lattice approach for weak couplings only.

The comparison of quantum and classical-statistical lattice results has been performed in great detail for purely bosonic theories in the past [64, 77]. Here, we concentrate on the fermion sector extending our earlier results [7]. We decompose the propagators into their respective statistical and spectral components as [6]

$$G_{\sigma/\pi}(x,y) = F_{\sigma/\pi}(x,y) - \frac{i}{2}\rho_{\sigma/\pi}(x,y)\,\mathrm{sgn}(x^0 - y^0)\,, \tag{5.34}$$

$$G_{\psi}(x,y) = F_{\psi}(x,y) - \frac{i}{2}\rho_{\psi}(x,y)\,\mathrm{sgn}(x^0 - y^0)\,. \tag{5.35}$$

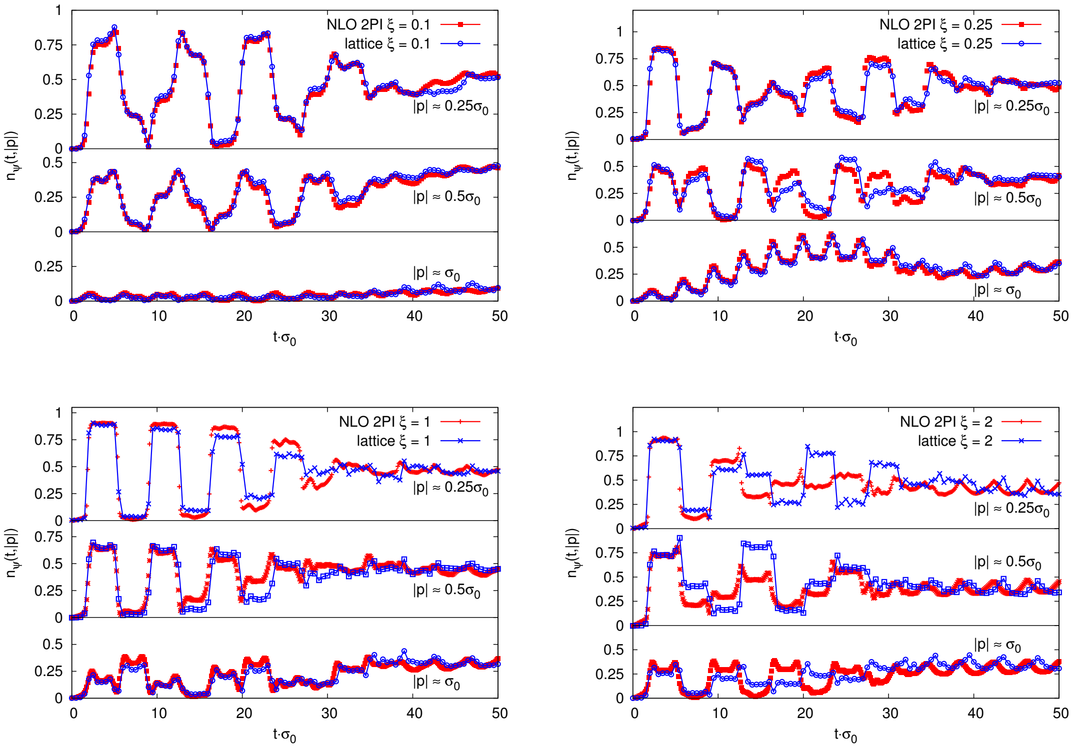

Figure 5.6.: Time evolution of fermion occupation numbers for three different momenta at effective coupling strengths in the range $\xi = 0.1 - 2.0$.

The statistical two-point functions $F_{\sigma/\pi}(x,y)$ and $F_{\psi}(x,y)$ as well as the corresponding spectral functions are the ones defined in 5.1.1. In particular, we employ the same definitions for extracting the time evolution of particle numbers.

In Fig. 5.6, we plot the fermion number $n_{\psi}(t,|\mathbf{p}|)$ as a function of time for three different momentum modes $|\mathbf{p}| = 0.25\sigma_0$, $0.5\sigma_0$ and σ_0. Since we expect our approximation of the 2PI effective action for the quantum evolution to break down at strong coupling, we give the results for different values of the effective coupling $\xi = g^2/\lambda$ and compare them to the respective lattice simulation results. One observes from Fig. 5.6 that for $\xi = 0.1$ the agreement between quantum and lattice approach is almost perfect. It worsens with increasing coupling as expected, but even at $\xi = 1.0$ infrared modes seem to be quite accurately reproduced. However, at $\xi = 2$ the coupling expansion seems to finally break down.

In Figs. 5.7 and 5.8, we present the full spectrum at fixed time $t\sigma_0 = 50$ for two different couplings. We observe a rather good agreement between both methods, reproducing characteristic features in the shape of the distribution. However, there is a clear discrep-

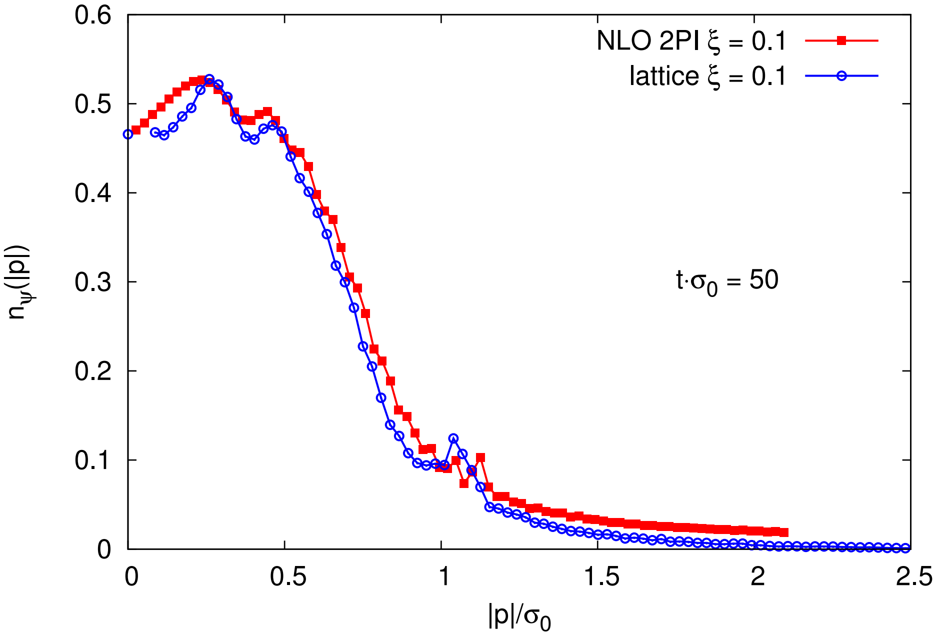

Figure 5.7.: Comparison between fermion spectra computed with 2PI and on the lattice at $\xi = 0.1$.

ancy in the high-momentum part of the spectrum building up for the larger $\xi = 0.25$. In general, we find good agreement between both methods at sufficiently small ξ as expected while the agreement worsens for larger ξ. The level of agreement for small ξ is also remarkable since the comparison involves two very different procedures: The results from the quantum 2PI effective action approach are obtained from a single run of the time evolution equations for correlation functions, while the lattice results are computed from a statistical average of many different runs of the corresponding lattice evolution equations. Already because of the Wilson term for the lattice description, it is rather difficult to get precisely the same initial conditions realized in both cases.

These results confirm that possible dicretization and statistical errors on the lattice are under control. On the other hand, they show that for not too strong coupling a loop approximation beyond lowest order is sufficient to describe fermion production accurately. This has to be confronted with standard semi-classical (LO) descriptions of fermion production, which employ the solution of a Dirac equation in the presence of a time-dependent, but spatially homogeneous background field neglecting fluctuations [21]. In this case, the evolution equation for the fermion statistical two-point function reads

$$\left[i\gamma^\mu \partial_{x,\mu} - \frac{g}{2}\phi(t) \right] F_\psi(x,y) = 0\,. \tag{5.36}$$

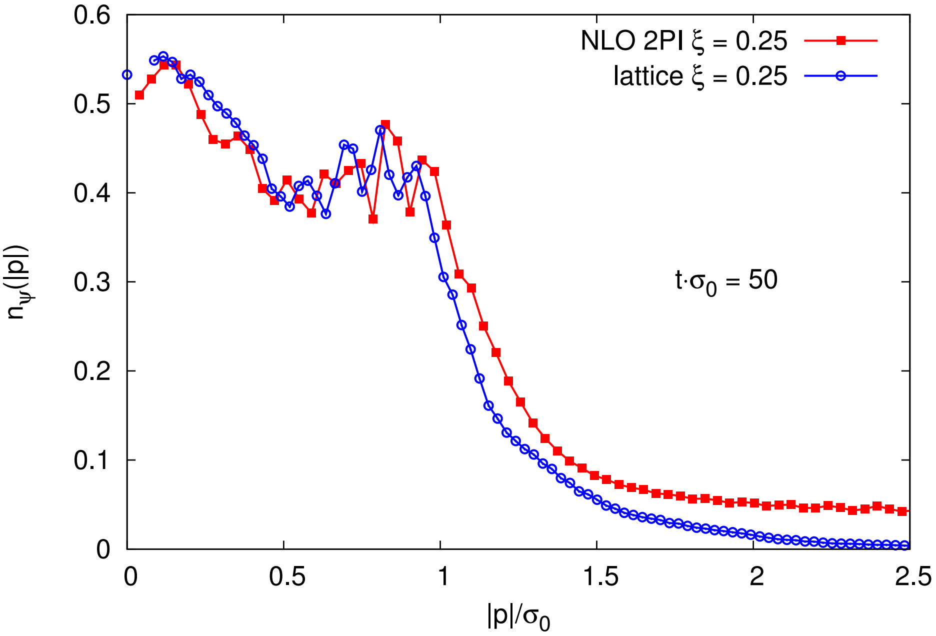

Figure 5.8.: Comparison between fermion spectra computed with 2PI and on the lattice at $\xi = 0.25$.

In contrast, our employed NLO 2PI approximation includes one-loop self-energy corrections to this equation. From the point of view of the lattice approach, a crucial difference concerns the spatial dependence of the fluctuating fields appearing in (5.21). Sampling with respect to these fluctuations leads to the generation of loop corrections for ensemble averages, which are missing in (5.36). In the next section, we will present numerical evidence that a semi-classical approximation fails to describe the dynamics and may only be applied for very short times of the initial evolution.

5.1.5. Fermion production from parametric resonance

The initial conditions described in 5.1.1 lead to the well-known phenomenon of parametric resonance in the scalar sector (described in 2.2.1) which we summarize here as follows: Small initial quantum fluctuations grow exponentially in time. At early times this growth occurs in a compact momentum range with $\mathbf{p}^2 \leq \sigma_0^2/2$. As time proceeds, the exponentially growing modes induce non-linear behaviour and secondary instabilities for higher momentum modes with even faster growth rates occur. As a consequence, there is a fast rise in the occupation numbers $n_{\sigma,\pi}(t,|\mathbf{p}|)$ for a broad momentum range. Figs. 5.9 and 5.10 show the behavior of the field $\phi(t)$ and the occupancies of transverse modes

$n_\pi(t, |\mathbf{p}|)$, respectively. The rapidly oscillating field decreases its amplitude with time, while the occupancies grow. After the fast initial growth period of occupation numbers, the time evolution of the now highly occupied scalar field modes slows down considerably, and can be described in terms of turbulent flows of energy and particle number [79, 80, 81, 82]. The subsequent evolution becomes self-similar and the corresponding power-law behavior with $n_\pi(|\mathbf{p}|) \sim 1/|\mathbf{p}|^4$ is clearly visible from Fig. 5.10.

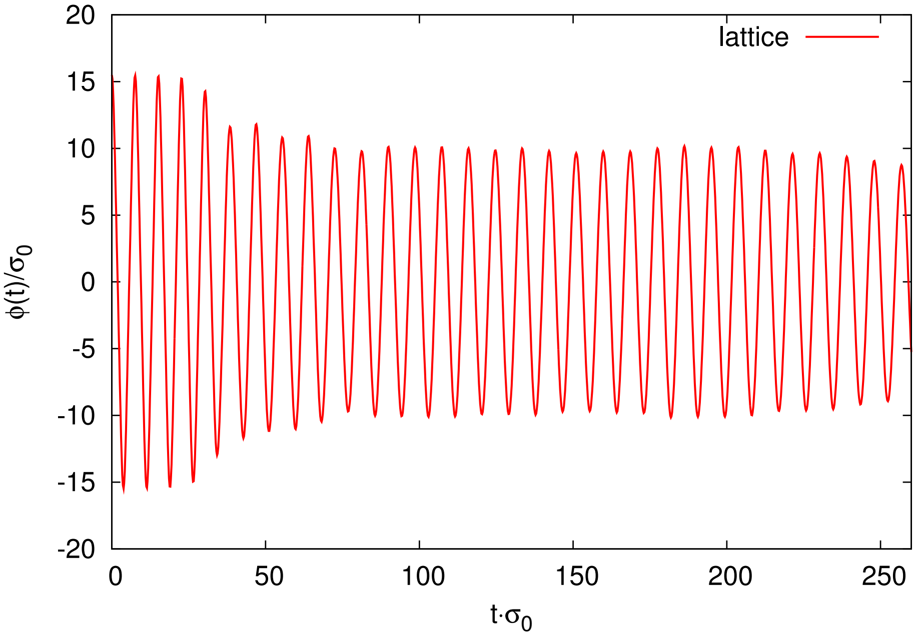

Figure 5.9.: Time evolution of the macroscopic field.

In the following, we will analyze the behavior of the fermions, which is the main topic of our work. To this end, it is useful to compare our lattice simulation results with standard semi-classical approximations based on Eq. (5.36). For this comparison we distinguish the weak-coupling regime, where $\xi = g^2/\lambda \ll 1$, and the strongly coupled case with ξ of order one. Fig. 5.11 shows the fermion occupation number distribution for $\xi = 0.1$ at the time $t\sigma_0 = 250$ after the initial instability has ceased. The lattice simulation results (circles) show a low-momentum range for $|\mathbf{p}| \leq \sigma_0$, where the distribution is rather flat. For higher momenta one observes a power-law behavior whose exponent agrees well with the scaling exponent found for the bosonic occupancies as shown in Fig. 5.10. While bosons can support a $1/|\mathbf{p}|^4$ dependence also at low momenta, the fermion number distribution has to level off in the infrared because of the Pauli exclusion principle of course [85, 96]. For this weak-coupling case we observe corresponding results also in the quantum theory based on the 2PI effective action at NLO, in accordance with the

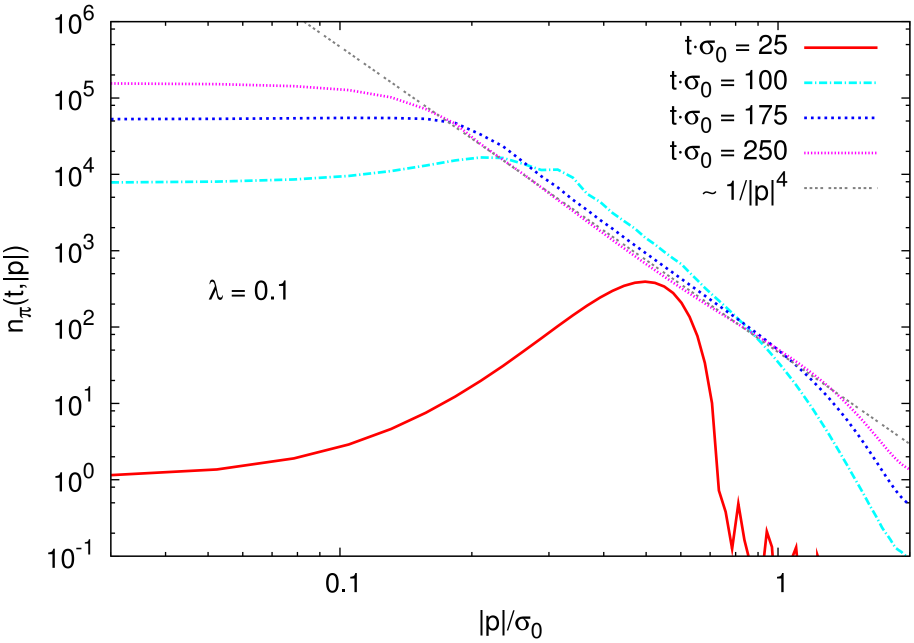

Figure 5.10.: Spectra of transverse scalar occupation numbers at different times.

discussion of Sec. 5.1.4. However, the lattice results including fluctuations clearly show significant differences to the semi-classical approximation results (squares), which neglect all fluctuations. In fact, the observed differences are so pronounced only after the bosonic fields become highly populated. This enhancement of fluctuations, which is missing in standard semi-classical approximations, will be discussed in detail below.

A similar snapshot of occupation number spectra for the strongly coupled case ($\xi = 1$), shown in Fig. 5.12, reveals a rather different picture. Here, the lattice simulation exhibits a distribution without any power-law behaviour. Remarkably, the distribution can be nicely fitted to a Fermi-Dirac distribution with time-dependent temperature and chemical potential parameters. At the time $t\sigma_0 = 250$ employed for Fig. 5.12 they are $T/\sigma_0 = 1.15$ and $\mu/\sigma_0 = 0.13$. The similarity to the Fermi-Dirac distribution is non-trivial at this stage, since the bosons are still far from equilibrium showing the characteristic $\sim 1/|\mathbf{p}|^4$ behavior in the infrared. The Fermi-Dirac distribution also requires the specification of a dispersion relation or ω_p and we approximate it here by the free dispersion relation for massless fermions with a pseudoscalar Wilson term as discussed in (4.36). It should be emphasized that the total charge in our simulations is zero such that the number of particles and antiparticles is equal. As a consequence, the chemical potential vanishes for true thermal equilibrium. Here we find that $\mu(t)$ is oscillating, which is not surprising in view of the oscillating Yukawa fermion mass term at this stage, and its absolute value turns out

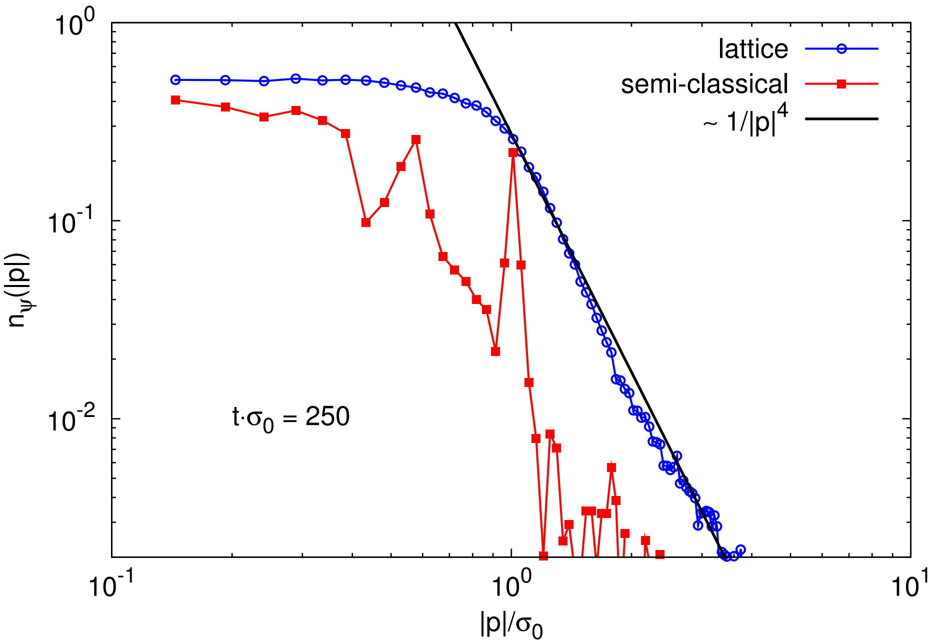

Figure 5.11.: Lattice simulation results for the occupation number distribution of weakly coupled fermions with $\xi = 0.1$ are compared to the standard semi-classical approximation.

to be much smaller than the temperature for all considered times. The time-dependence of the fitted temperature parameter is shown in Fig. 5.13. It is seen to approximately rise linearly in time, after performing an average over periods of $\triangle t = 5/\sigma_0$ in order to smooth oscillations due to $\phi(t)$. To get a simple estimate of how much this time-dependent temperature parameter deviates from the value of the equilibrium temperature, we compute the temperature of a corresponding gas of non-interacting massless bosons and fermions having a continuum dispersion relation:

$$T_{\mathrm{eq}} = \sigma_0 \left(\frac{45 N_s}{\pi^2 \left(N_s + \frac{7}{2} N_f \right) \lambda} \right)^{\frac{1}{4}} \simeq 2.02 \sigma_0 \,. \tag{5.37}$$

Here, we used the initial energy density, which for parametric resonance is given in terms of $\phi(t = 0)$ and the self-coupling λ (here and throughout this section $\lambda = 0.1$). This estimate indicates that the observed time-dependent temperature parameter is still far from the asymptotic equilibrium value. The observed linear rise of the temperature parameter would lead to the above estimate for the equilibrium temperature after a time $t_{\mathrm{eq}} \simeq 10^3/\sigma_0$.

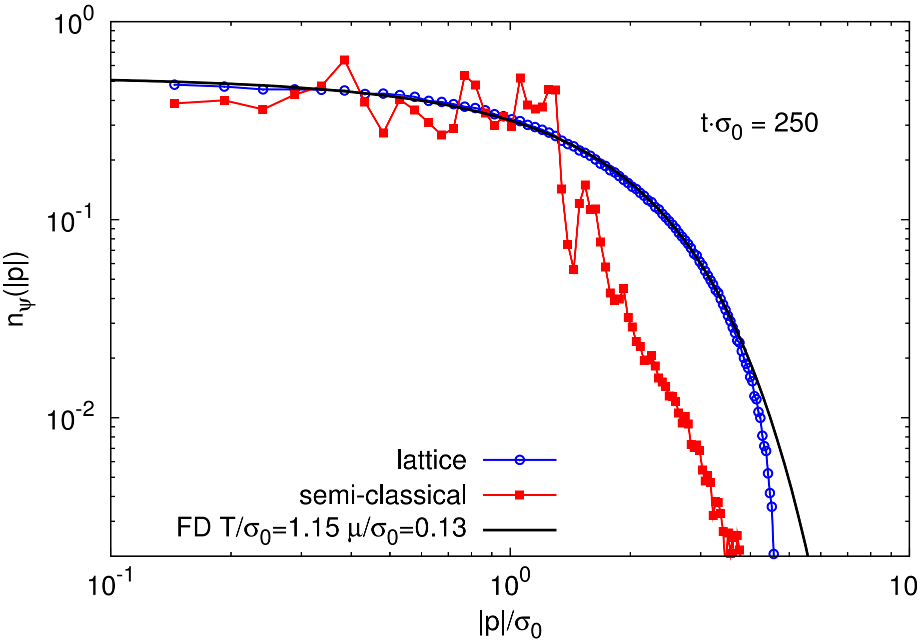

Figure 5.12.: Lattice simulation results for the occupation number distribution of strongly coupled fermions with $\xi = 1$ are compared to the semi-classical approximation. Shown is also a Fermi-Dirac distribution with time-dependent temperature and chemical potential parameters.

In order to study in more detail the similarities and deviations from a Fermi-Dirac distribution, it is instructive to consider the 'inverse slope parameter' $\ln\left(n_\psi^{-1} - 1\right)$. Fig. 5.14 shows this quantity for $\xi = 1$ as a function of ω_p at four different times. For a thermal equilibrium distribution it would be a time-independent straight line. For a vanishing chemical potential in thermal equilibrium this line would go through the origin. One observes from the figure that an approximately stable inverse slope is established rather quickly for low momenta around $|\mathbf{p}| \lesssim 1.5\omega_p/\sigma_0$. This is due to the fact that already at early times many low-momentum bosonic quanta are occupied, making it possible for fermions to scatter off them and redistribute momentum and energy. In contrast, there are almost no high-momentum bosons present at early times, preventing a more efficient transfer of energy and particles to the UV. Around $t\sigma_0 = 250$ one observes again the high level of agreement with a Fermi-Dirac distribution with fitted temperature and chemical potential parameter at that time.

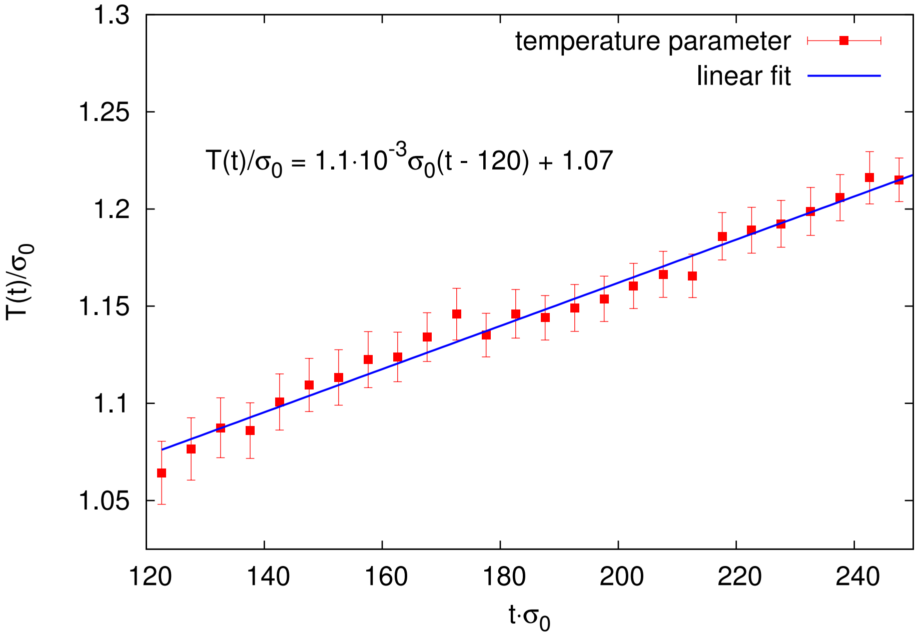

Figure 5.13.: Behaviour of the time-dependent temperature parameter.

5.1.6. Understanding amplified fermion production

The above lattice simulation results for fermion production from parametric resonance revealed a dramatic difference compared to standard semi-classical estimates. The latter includes for instance fermion decay from a homogeneous background field, but neglects fluctuations or scattering effects. Scattering processes can become strongly enhanced if the participating modes are highly occupied. Correspondingly, the observed differences between lattice simulations and the semi-classical treatment are pronounced once the bosons become strongly occupied.

In the following, we analyze the impact of scattering processes on the dynamics in more detail. To this end, we consider the NLO $1/N$ approximation for the quantum 2PI effective action of 5.1.4 in the weak-coupling regime with $\xi = 0.1$. As discussed above, the NLO 2PI approximation is found to accurately reproduce the full lattice simulation result in this regime. In particular, we will use this approximation to derive kinetic equations that explain the relevant underlying processes. The power counting will be based on an expansion in the coupling g in the presence of large occupancies with parametric dependence $n_{\sigma,\pi}(t, |\mathbf{p}|) \sim 1/\lambda$ for $\lambda \ll 1$ and $g^2/\lambda \ll 1$. We also emphasize that the observation of an amplified fermion production in the presence of large bosonic occupancies is not specific to the phenomenon of parametric resonance, however we will continue to consider this example. For the main points of the following analysis one could equally well

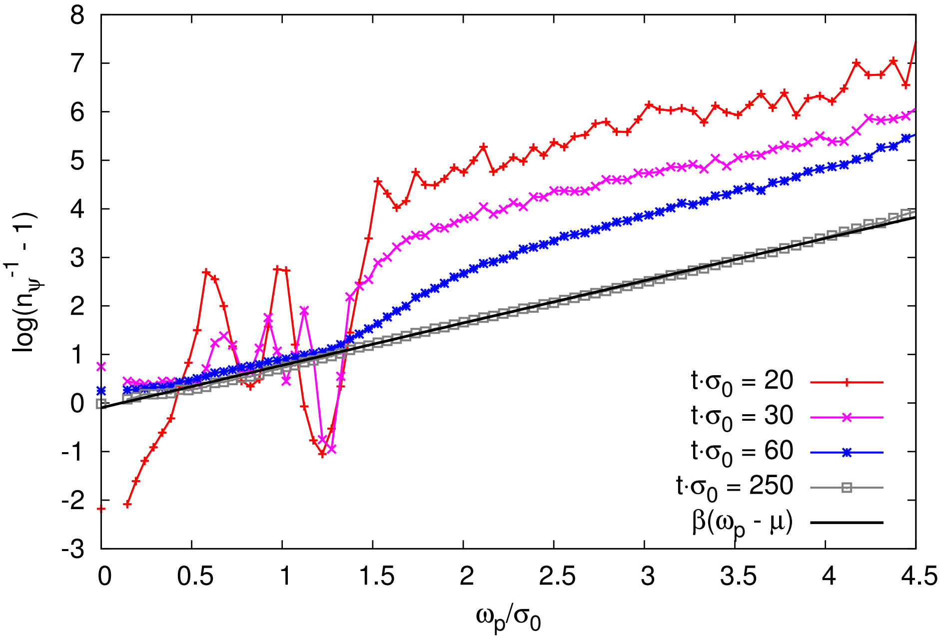

Figure 5.14.: Lattice simulation results for the "inverse slope parameter" $\ln\left(n_\psi^{-1} - 1\right)$ at four different times. For comparison the solid line corresponds to a Fermi-Dirac distribution with fitted temperature and chemical potential at $t\sigma_0 = 250$, having the same values as in Fig. 5.12.

consider other non-equilibrium instabilities leading to – or even directly starting from – large occupancies.

Counting powers of the coupling g, direct scattering appears at order g^2 according to 5.1.4, whereas the semi-classical approximation based on equation (5.36) is restricted to processes at order g. Fig. 5.15 compares the total number of produced fermions at order g^2 (NLO 2PI, solid line) to results from the semi-classical approximation (dashed line). In the figure, we also give an analytic estimate for the production rate from kinetic theory (dotted line), which will be explained below. While for very short times the order g and g^2 results agree rather well, after the end of the parametric resonance regime, i.e. when the occupancies become large, the order g^2 corrections are seen to dominate the fermion production by far. Apparently, highly occupied bosons act as a very efficient amplifier for genuine quantum corrections to the fermion dynamics.

This phenomenon can be understood from the NLO approximation of the 2PI effective action described in 5.1.4. In order to make analytic progress, we consider a standard gradient expansion to lowest order in derivatives following Ref. [97] and already introduced in Sec. 3.3. It employs for two-point functions, such as $F_\phi(x, y)$ given by (5.10)

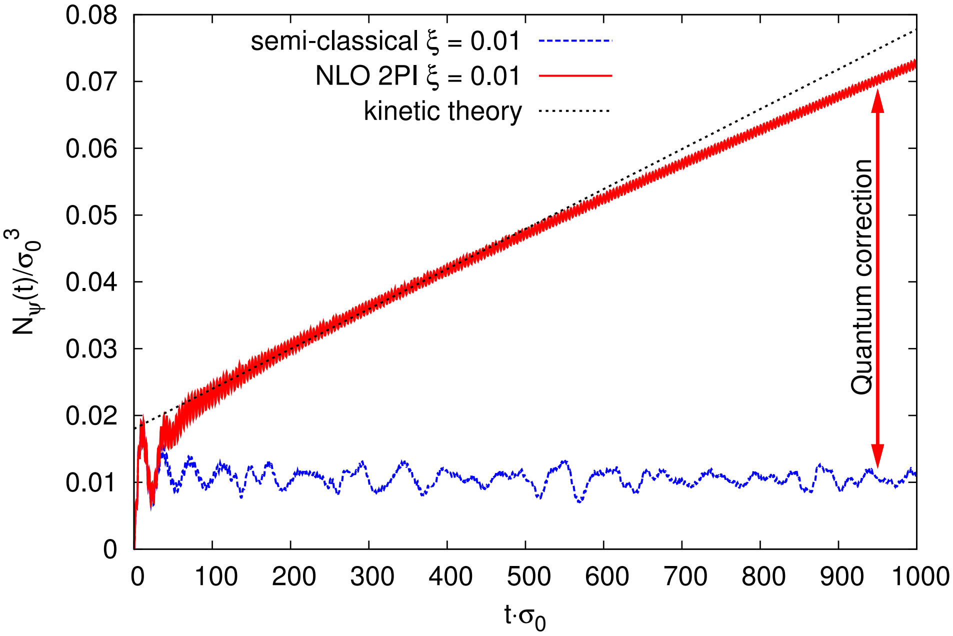

Figure 5.15.: Total number of produced fermions at order g (semi-classical approximation, dashed line) and order g^2 (NLO 2PI, solid line) for the weak-coupling regime with $\xi = g^2/\lambda = 0.01$. Shown is also an analytic estimate for the production rate from kinetic theory (dotted line), which is shifted to account for the initial semi-classical fermion production until $t\sigma_0 \simeq 10$.

and $F_\psi(x, y)$ defined in (5.9), the introduction of relative coordinates $x - y$ and center coordinates $(x+y)/2$. For the considered spatially homogeneous systems, a Fourier transformation with respect to the relative coordinates leads to $F_{\sigma,\pi}(t, k)$ and $F_\psi(t, k)$ with four-momentum k and the time coordinate $t \equiv (x^0 + y^0)/2$. The general form of the equation for the boson two-point function to lowest order in derivatives with respect to the center coordinate is

$$2k^0\partial_t F_{\sigma,\pi}(t, k) \;=\; \Sigma_\rho(t, k)F_{\sigma,\pi}(t, k) - \Sigma_F(t, k)\rho_{\sigma,\pi}(t, k)\,, \tag{5.38}$$

where the "collision term" on the right hand side encodes the "gain" minus "loss" structure in terms of the statistical (Σ_F) and spectral (Σ_ρ) parts of the self-energy. At order g^2 the spectral and statistical components of the self-energy displayed on the right of Fig. 5.1 read

$$\begin{aligned}\Sigma_F(t, k) \;&=\; \frac{g^2}{2}\int\frac{d^4p}{(2\pi)^4}\mathrm{Tr}[F_\psi(t, k+p)F_\psi(t, p) - \frac{1}{4}\rho_\psi(t, k+p)\rho_\psi(t, p)]\,,\\ \Sigma_\rho(t, k) \;&=\; \frac{g^2}{2}\int\frac{d^4p}{(2\pi)^4}\mathrm{Tr}[F_\psi(t, k+p)\rho_\psi(t, p) - \rho_\psi(t, k+p)F_\psi(t, p)]\,.\end{aligned}$$

The physical content of these expressions can be further clarified by setting the fermion spectral function $\rho_\psi(t,k)$ on shell and introducing occupation numbers $n_\phi(t,k)$ and $n_\psi(t,k)$ for bosons and fermions, respectively, with

$$\begin{aligned} F_{\sigma,\pi}(t,k) &= \left[\frac{1}{2} + n_\phi(t,k)\right]\rho_{\sigma,\pi}(t,k)\,, \\ F_\psi(t,k) &= \left[\frac{1}{2} - n_\psi(t,k)\right]\rho_\psi(t,k)\,. \end{aligned} \tag{5.39}$$

The (anti-)symmetry of the (spectral) statistical correlation functions translates into

$$n_\phi(t,-k) = -\left[n_\phi(t,k)+1\right]\,, \quad n_\psi(t,-k) = -\left[n_\psi(t,k)-1\right]\,. \tag{5.40}$$

The time-independent on-shell spectral functions are given by

$$\rho_{\sigma,\pi}(k) = 2\pi\mathrm{sgn}(k^0)\delta(k^2-m^2)\,, \tag{5.41}$$

$$\rho_\psi(k) = 2\pi k_\mu\gamma^\mu\mathrm{sgn}(k^0)\delta(k^2)\,, \tag{5.42}$$

for the considered case of massless fermions. After performing traces in spinor and flavour space as well as some of the integrals and projecting onto positive frequencies we arrive at

$$\begin{aligned} \partial_t n_\phi(t,\mathbf{k}) = {} & \pi g^2\int\frac{d^3p}{(2\pi)^3}\int d^3q\ \delta(\mathbf{k}-\mathbf{p}-\mathbf{q})\ \delta(\omega_k-|\mathbf{p}|-|\mathbf{q}|)\,\frac{1}{\omega_k}\left(1-\frac{\mathbf{pq}}{|\mathbf{p}||\mathbf{q}|}\right)\times \\ & \times\left[\left(n_\phi(t,\mathbf{k})+1\right)n_\psi(t,\mathbf{p})n_\psi(t,\mathbf{q})\ -n_\phi(t,\mathbf{k})\left(n_\psi(t,\mathbf{p})-1\right)\left(n_\psi(t,\mathbf{q})-1\right)\right]\,. \end{aligned} \tag{5.43}$$

Here $\omega_k = \sqrt{k^2+m^2}$ is the free bosonic dispersion relation. Along the same lines one can obtain the corresponding kinetic equation for the fermion occupation number,

$$\begin{aligned} \partial_t n_\psi(t,\mathbf{k}) = {} & \pi g^2\int\frac{d^3p}{(2\pi)^3}\int d^3q\ \delta(\mathbf{k}+\mathbf{p}-\mathbf{q})\ \delta\big(|\mathbf{k}|+|\mathbf{p}|-\omega_q\big)\,\frac{1}{\omega_q}\left(1-\frac{\mathbf{kp}}{|\mathbf{k}||\mathbf{p}|}\right)\times \\ & \times\left[\left(n_\psi(t,\mathbf{k})-1\right)\left(n_\psi(t,\mathbf{p})-1\right)n_\phi(t,\mathbf{q}) - n_\psi(t,\mathbf{k})\left(n_\psi(t,\mathbf{p})-1\right)\left(n_\phi(t,\mathbf{q})+1\right)\right]\,. \end{aligned} \tag{5.44}$$

From these expressions we observe that

$$\partial_t\left(N_\phi(t)+N_\psi(t)\right) = \int\frac{d^3k}{(2\pi)^3}\partial_t\left(n_\phi(t,\mathbf{k})+n_\psi(t,\mathbf{k})\right) = 0 \tag{5.45}$$

reflecting total number conservation of bosons and fermions, $N_\phi + N_\psi$, in this approximation. Total number changing processes would enter the kinetic description at higher order in g. However, they are crucial for the approach to thermal equilibrium at late times [85, 98], these processes turn out not to be important for the time of enhanced fermion production in the weak-coupling regime.

It is instructive to consider (5.43) for $n_\psi = 0$, which is approximately realized at sufficiently early times. The equation can then be written as

$$\partial_t n_\phi(t, \mathbf{k}) \simeq -\Gamma_{\phi\to\psi\bar\psi}(\mathbf{k})\, n_\phi(t, \mathbf{k}) \tag{5.46}$$

with

$$\Gamma_{\phi\to\psi\bar\psi}(\mathbf{k}) = \pi g^2 \int \frac{d^3p}{(2\pi)^3} \int d^3q\ \delta(\mathbf{k} - \mathbf{p} - \mathbf{q})\, \delta\left(\omega_k - |\mathbf{p}| - |\mathbf{q}|\right) \frac{1}{\omega_k} \left(1 - \frac{\mathbf{pq}}{|\mathbf{p}||\mathbf{q}|}\right). \tag{5.47}$$

For $\mathbf{k} = 0$ one obtains the standard vacuum decay rate for the production of massless fermions with momenta $\pm m/2$, i.e. $\Gamma_{\phi\to\psi\bar\psi}(0) = g^2 m/(8\pi)$. Taking the number conservation (5.45) into account, we can write for the change in the total fermion number

$$\partial_t N_\psi(t) \simeq \int \frac{d^3k}{(2\pi)^3} \Gamma_{\phi\to\psi\bar\psi}(\mathbf{k})\, n_\phi(t, \mathbf{k}). \tag{5.48}$$

To get a parametric estimate for the right hand side, we may approximate $n_\phi(t, \mathbf{k}) \simeq \Theta(|\mathbf{k}| - \sigma_0)/\lambda$ around the time after the parametric resonance regime ends. The crucial ingredient here is the enhancement by a factor of $1/\lambda$, which for the considered weak-coupling case encodes the amplification of $\partial_t N_\psi$ from being order g^2 to order $g^2/\lambda \equiv \xi$ for parametrically large Bose occupancies. As a consequence, one expects an approximately linear rise in the total fermion number with slope proportional to ξ as shown in Fig. 5.15 for $\xi = 0.01$. Because of the non-zero fermion occupation numbers building up with time, this linear rise is diminished by the Pauli suppression due to the presence of already produced fermions. We can also use (5.43) to estimate the magnitude of the backreaction of fermions onto the bosonic sector. To this end, we compare the bosonic gain term $\sim n_\psi(t, \mathbf{p}) n_\psi(t, \mathbf{q})$ to the loss term $\sim -n_\phi(t, \mathbf{k})(1 - n_\psi(t, \mathbf{q}) - n_\psi(t, \mathbf{k}))$. The latter is enhanced by the macroscopic occupation of scalars while the former is strictly ≤ 1 and we find it to be even $\leq 1/4$ at later times during our simulations. The minor role of fermionic backreaction in the weak-coupling regime agrees well with our findings from the full simulation data.

The above kinetic description provides a detailed understanding of the weak-coupling case with $\xi \ll 1$. It is expected to fail to describe the physics for strong couplings, where higher order processes are no longer suppressed. This is also what we find by comparing it to the nonperturbative lattice simulation results in accordance with the discussion of 5.1.4. It is a characteristic property of the above kinetic description that typical fermion and boson momenta are similar. In Fig. 5.16 on the left we show the occupancies of bosons and produced fermions for $\xi = 0.1$, where the highest momenta with a non-vanishing occupation number lie in the same region for both species. The right graph shows the same quantities for $\xi = 1$, where one observes the tendency for fermions to extend their

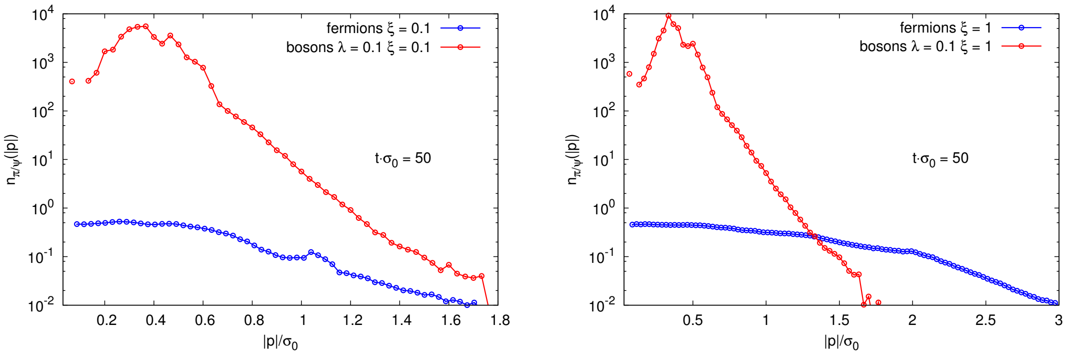

Figure 5.16.: Lattice simulation results for occupation number distributions of fermions and bosons at $t\sigma_0 = 50$ for $\xi = 0.1$ (left) and $\xi = 1$ (right).

distribution to higher momenta than it is the case for bosons. Even though the fermion occupancy per mode is limited by the exclusion principle, they quickly populate higher momentum modes in the nonperturbative regime. This contribution becomes essential for strong enough coupling since the high-momentum part carries most of the energy.

5.1.7. Conclusions

In this section we have studied non-equilibrium production of fermions from parametric resonance in 3 + 1 dimensions for a generic linear sigma model. As our main result, we confirmed the dramatic amplification of fermion production in the presence of highly occupied bosons that was first pointed out in Ref. [7] and extended the results to the strong coupling regime.

We compared different real-time techniques – lattice simulations with male/female fermions, mode functions approach and quantum 2PI effective action with its associated kinetic theory – and discussed their range of applicability. It turned out that the efficient male/female lattice approach accurately converges to the exact mode functions result for the available lattice sizes. The study shows the strength of the male/female method to address physical questions for large volumes, where the mode function approach becomes computationally intractable. For weak couplings we found that the lattice simulation results agree well with those obtained from the quantum 2PI effective action, emphasizing the ability of the lattice approach to describe genuine quantum phenomena.

Applying an improved lattice discretization with a pseudoscalar Wilson term, we were able to accurately resolve the high-momentum behaviour of particle number distributions. For weak couplings this revealed a power-law behavior above a characteristic momentum. For strongly coupled fermions, we found that a quasi-thermal Fermi-Dirac distribution is approached, with time-dependent temperature and chemical potential parameters. This happens while the bosons are still showing turbulent behavior far from equilibrium [99].

In the employed model, the coupling to the fermions and the bosonic self-coupling can be separately chosen to represent the weak-coupling ($\xi \ll 1$) and the strong-coupling regime ($\xi \gtrsim 1$). This allowed us to validate the lattice simulation techniques in the weak-coupling regime by comparing it to alternative, quantum techniques. Another interesting application of these methods are investigations of theories where $\xi \ll 1$ cannot be realized. An important class of such theories concerns non-Abelian gauge theories, where the bosonic self-coupling and the coupling to the fermion sector are given by the same coupling such that the relevant ratio is $\xi = 1$.

5.2. Massive fermions from tachyonic preheating

In the last section, we discussed the phenomenon of enhanced production of fermions during parametric resonance. An aspect of these investigations was a time-dependent Yukawa mass. The oscillating macroscopic field caused a damped oscillation of the effective mass term, so that the particles were constantly switching between a massless and a massive state. While the initial conditions described massive fermions, it is clear that for infinitely late times the massive state would have disappeared since the field would eventually have come to rest in the minimum of the symmetric potential. In this section, we will consider a case in which fermions remain massive even after thermalization. Contrary to the previous study we will start from a state with a vanishing or negligible mass, however, early stages of time evolution will lead to an exponentially increasing m_ψ^2. After these early stages the field and simultaneously the Yukawa mass will saturate at a finite value.

Investigations of both types of fermion dynamics should complement each other because a mutual comparison may allow us to disentangle production mechanisms for light and heavy fermions. A feature parametric and tachyonic scenarios have in common is the existence of essentially two channels of fermion production involved in both of them, namely the decay of bosonic fluctuations and direct production from the time-dependent homogeneous fields. A clean way to separate the impacts of these production channels is to combine lattice simulations of fully interacting system with leading-order calculations. This recipe was used in the previous section and we will return to it here as well.

To realize tachyonic instability in quantum field theory we perform a quench at the beginning of the time evolution, by changing the sign in front of m^2 after vacuum initial conditions, similar to the ones introduced in the last section, have been set. This procedure leads to the emergence of a double-well potential characteristic for spontaneous symmetry breaking with a concave shape around the origin.

Starting from such initial conditions leads to the emergence of exponentially growing scalar occupation numbers. This can be seen by looking at the equation of motion for $F_\phi(t,t',\mathbf{p})$ at early times

$$\left[\partial_t^2 + \mathbf{p}^2 - m^2\right] F_\phi(t,t',\mathbf{p}) = 0\,, \tag{5.49}$$

where all contributions from fluctuations, which are not relevant during these early stages, have been omitted. The macroscopic field is also rolling down towards the minimum of the double-well potential exhibiting a typical growth rate of $\gamma_0 = m$ (with $m = \sqrt{|m^2|}$), according to the linearized equation of motion

$$\left[\partial_t^2 - m^2\right] \phi(t) = 0\,. \tag{5.50}$$

Scalar occupation numbers grow with a momentum dependent rate

$$\gamma\,(\mathbf{p}) = 2\,\sqrt{m^2 - \mathbf{p}^2}\,. \tag{5.51}$$

which is maximal for $|\mathbf{p}| = 0$ and represents the equal-time behaviour of the statistical propagator $F_\phi(t,t',\mathbf{p}) \sim e^{\sqrt{m^2-\mathbf{p}^2}(t+t')}$. Obviously, the unstable modes are confined to the low momentum region $|\mathbf{p}| < m$. This initial growth pattern changes with time as self-energy contributions become important. In particular, one observes secondary instabilities at higher momenta which start at later times, but grow with multiples of the maximal primary growth rate. Finally, primary as well as secondary growth breaks down as soon as fluctuations become parametrically of the order $1/\lambda$, meaning that this stage cannot be described in any perturbative approach relying on an expansion in powers of λ.

5.2.1. Implementation and results

Fermion production during tachyonic preheating is tightly connected to the dynamics of bosons, as has been shown in [96]. To assess the enhancement of fermion production from symmetry breaking for a range of effective couplings, we consider a simplified model which is of major relevance to cosmological studies of reheating in the early universe. Here, we restrict ourselves to one scalar bosonic field interacting with itself and coupled to one flavour of Dirac fermions via a standard scalar Yukawa coupling:

$$\mathcal{L} = \frac{1}{2}\partial_\mu\phi\,\partial^\mu\phi - \frac{1}{2}\,m^2\phi^2 - \frac{\lambda}{4!}\phi^4 + \bar{\psi}\left(i\,\partial_\mu\gamma^\mu\right)\psi - h\bar{\psi}\phi\psi. \tag{5.52}$$

When simulating the scenario of spinodal decomposition in this model, we do not single out any direction for the macroscopic field. This means that the field $\phi(t)$ itself remains zero while the modulus of the field $|\phi(t)| = \sqrt{\phi^2(t)}$ grows exponentially in time until it saturates in the new minimum of the potential. A very similar model, in which an additional bosonic sector was also coupled to the tachyonic field, has been considered in [100]. Since we will compare our numerical results to the analytical estimates made in this work, we will allow ourselves to repeat some of the key statements made there.

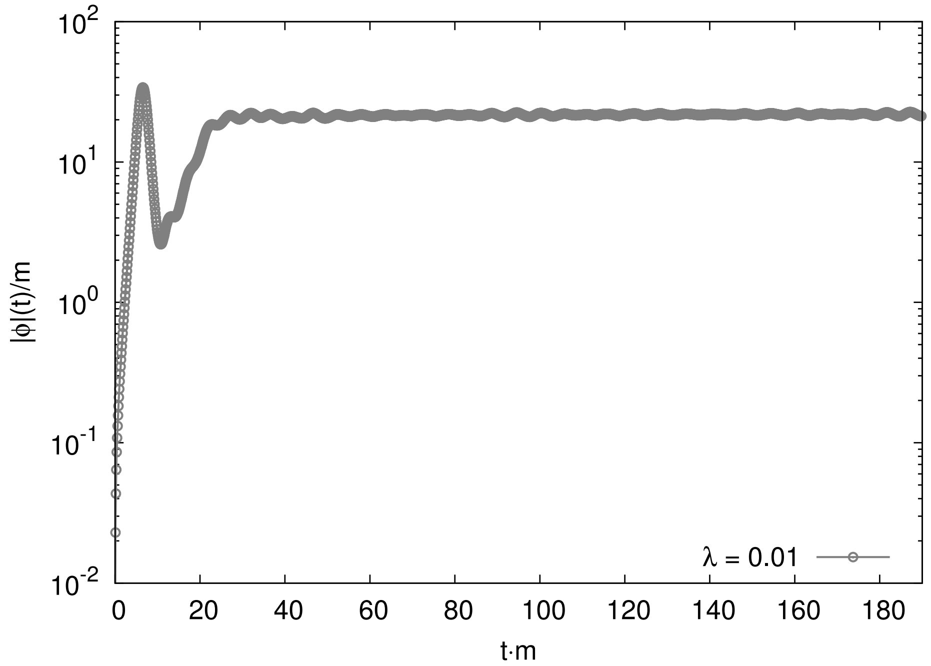

Figure 5.17.: Time dependence of the modulus of the macroscopic field. Mind the initial oscillations and subsequent relaxation to the new potential minimim.

The authors in [100] have considered fermions coupled to a time-dependent macroscopic field which undergoes symmetry breaking via spinodal decomposition. The analytical expression for the rolling down of the field without subsequent oscillations was given as

$$|\phi|(t) = \frac{v}{2}\left(1 + \tanh\frac{m(t-t_*)}{2}\right), \tag{5.53}$$

where t_* is the time at which the macroscopic field reaches the new potential minimum for the first time. We confirmed that this formula agrees with our numerical results at early times. In Fig. 5.17, we see that in our simulations the field modulus indeed rises exponentially in the beginning so that the rolling field increases even beyond the new minimum. Then, the field rolls back and oscillates for a period of time until it finally comes to rest. Since fermions acquire an effective Yukawa mass via $m_\psi^2 = h^2\phi^2$ they are driven to become massive after symmetry breaking. Taking into account only the classical double well potential, the final fermion mass should be $m_\psi = \sqrt{6}\frac{h}{\sqrt{\lambda}}m = \sqrt{6\xi}m$. Based on solving the Dirac equation for a time-dependent Yukawa mass the authors in [100] derived an analytical estimate for the time evolution of fermionic fluctuations. We will compare our results mainly to the expression for the shape of the spectrum after the end of the instability:

$$n_\psi(|p|, \sqrt{\xi}) = \frac{\cosh\left[2\pi\sqrt{6\xi}\right] - \cosh\left[2\pi(\sqrt{p^2 + 6\xi m^2} - |p|)/m\right]}{2\sinh\left[2\pi|p|/m\right]\sinh\left[2\pi\sqrt{p^2 + 6\xi m^2}/m\right]}, \tag{5.54}$$

as well as to their results for the total number of produced Dirac fermions and the share of total energy $\rho_0 = \frac{3m^4}{2\lambda}$ which was transfered into fermionic particles:

$$N_\psi(\sqrt{\xi}) = 1.44 \times 10^{-3} m^3 \frac{\sqrt{6\xi + 0.64} - 0.8}{\sqrt{6\xi}}, \tag{5.55}$$

$$\rho_\psi/\rho_0 = 1 \times 10^{-3} \lambda(\sqrt{6\xi + 0.64} - 0.8). \tag{5.56}$$

The factors of 6 appearing here come from the fact that we use a different definition for the scalar self-coupling λ as as the case in [100]. To see how fermions are produced during symmetry breaking we simulated the system for a range of effective couplings, $0.05 < \sqrt{\xi} < 1$. For both weak and strong couplings a similar time pattern arises, which is depicted in Fig. 5.18. Four stages of fermion production can be observed:

1. In the first, very short stage fermions are produced while the field modulus and fluctuations are initially increasing. Simultaneously, the Yukawa mass rises exponentially, terminating this stage as soon as fermion production becomes kinematically suppressed. This first phase lasts until $t \simeq 8/m$ in Fig. 5.18.

2. In the second stage of production, the field modulus oscillates back towards zero, making fermions lighter and therefore immediately lifting kinematical constraints. Additionally, the bosonic fluctuations are already exponentially enhanced at this point and free to decay into fermions, allowing a strong boost in the fermion production rate. This boost is very pronounced in Fig. 5.18 for $8/m \lesssim t \lesssim 22/m$. The combination of these two factors leads to an overabundance of fermions, which is only reduced in the following phase.

3. Finally the field goes back to its new minimum, so that a large portion of the now considerably heavier and overabundant fermions decay, as seen in Fig. 5.18 after $t \simeq 22/m$. The resulting spectrum marks the amount of fermions produced during the nonperturbative stage of symmetry breaking.

4. The longest phase begins after symmetry breaking, where massive fermions are produced by scattering and decay of bosonic particles. For sufficiently small values of ξ this processes may be described in the framework of a kinetic description with lowest-order matrix elements. If the fermion occupancies at this stage remain low ($n_\psi \ll 1/2$) despite all of the previous processes, we may disregard the non-linear Pauli suppression and would expect, similar to 5.1.6, a linearly rising total fermion

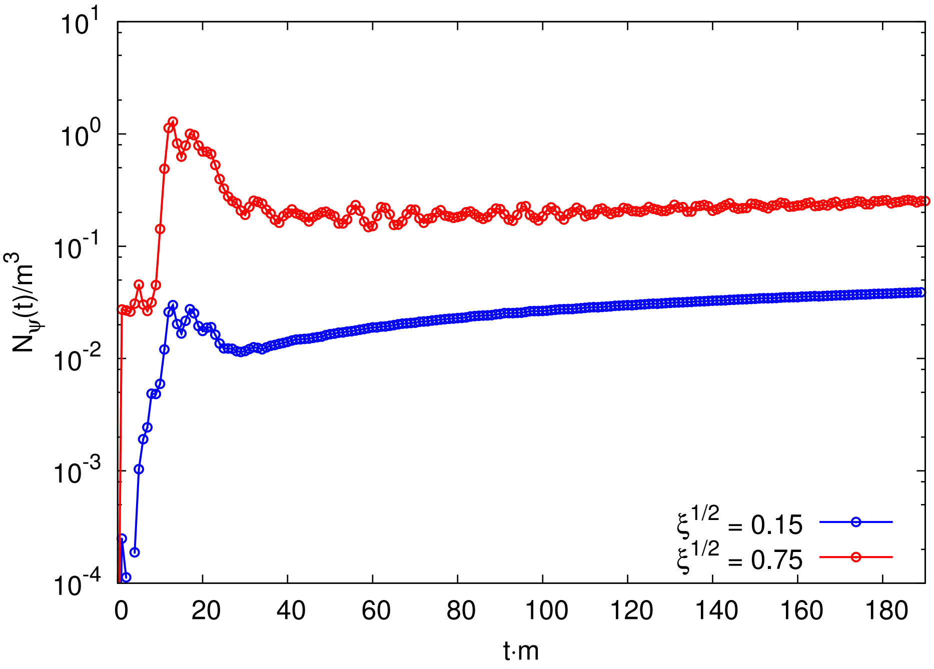

Figure 5.18.: Total number of produced fermions as a function of time for $\sqrt{\xi} = 0.15$ and $\sqrt{\xi} = 0.75$. The time pattern seems to be similar while stronger coupling leads to an increase in the overall output of fermionic particles.

> number. Excitingly, this is exactly the behaviour we observe in Fig. 5.18 for $\sqrt{\xi} = 0.75$ starting from $t \simeq 40/m$, while for $\sqrt{\xi} = 0.15$ the slope of the increasing total fermion particle number flattens over time. Further below we will link this observation to details of fermion spectra after the non-perturbative phase.

It appears that for stronger couplings the four stages are more distinctive, primarily because the mass plays a stronger role in the dynamics. Although both weakly and strongly coupled scenarios exhibit the same overall time pattern, the resulting spectra are clearly different, which is demonstrated in Figs. 5.19 and 5.20. In both cases, lattice results show that more particles are produced than could be expected based solely on leading-order arguments. The Pauli principle also ensures that the vast number of additional fermions occupy states with higher momenta, making them more relativistic. An interesting observation is that the particle numbers in the infrared are lower at stronger coupling, which is compensated by larger occupation of high momentum modes.

This can be explained by the fact that the height of a thermal Fermi-Dirac distribution for a vanishing chemical potential is determined by the mass, with higher masses leading to a lower occupation in the infrared. Since the fermion mass in our model is proportional to the coupling, it is clear that stronger couplings would indeed lower the typical occupa-

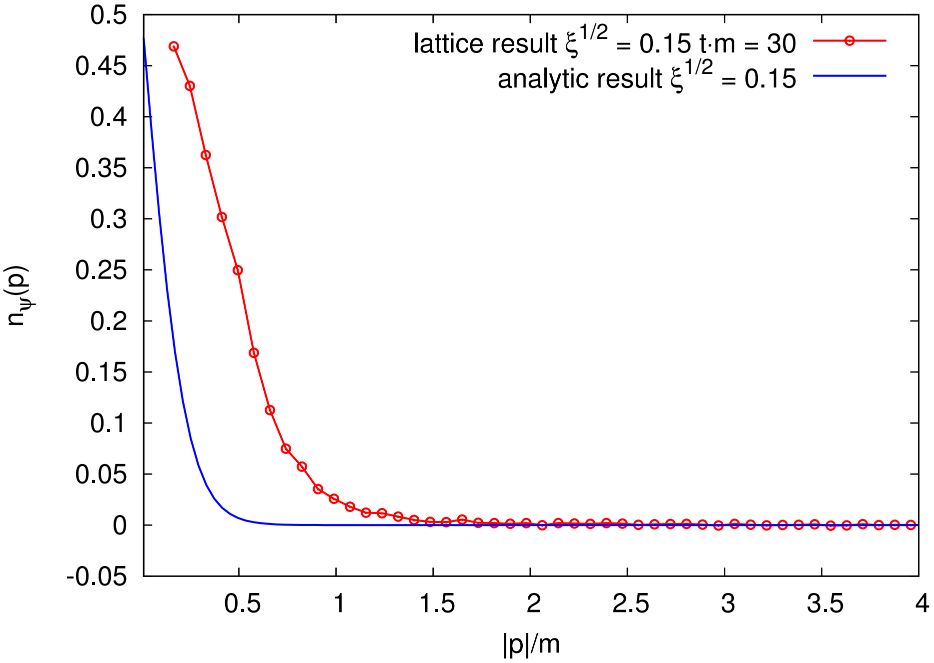

Figure 5.19.: Comparison between lattice results and analytical leading-order predictions for fermion spectra after symmetry breaking for $\sqrt{\xi} = 0.15$. The effective fermion mass for this coupling is $m_\psi \simeq 0.4m$.

tion number for low momenta. Because occupation numbers for strong couplings remain relatively low compared to $1/2$, we may neglect the Pauli blocking and by applying this approximation additionally explain the linearly rising total fermion number in Fig. 5.18 for later times.

Summarizing, the fermion spectrum at strong couplings is closer to the thermal distribution and is marked by lower occupation numbers. The weak coupling fermion spectrum in Fig. 5.19 is concentrated at low momenta, hence making Pauli suppression highly relevant and explaining the slope flattening over time of the total fermionic particle number in Fig. 5.18.

Another difference between lattice results and analytical estimates of a potentially phenomenological relevance is the already mentioned relativistic nature of fermion fluctuations. So far the leading-order results suggested that fermions produced after a tachyonic instability are non-relativistic. However our simulations indicate that this is not the case. A closer look at the lattice spectra in Figs. 5.19 and 5.20 reveals that for both weak and strong coupling there is a non-negligible share of fermions with momenta larger than their effective mass, thus invalidating possible non-relativistic approximations.

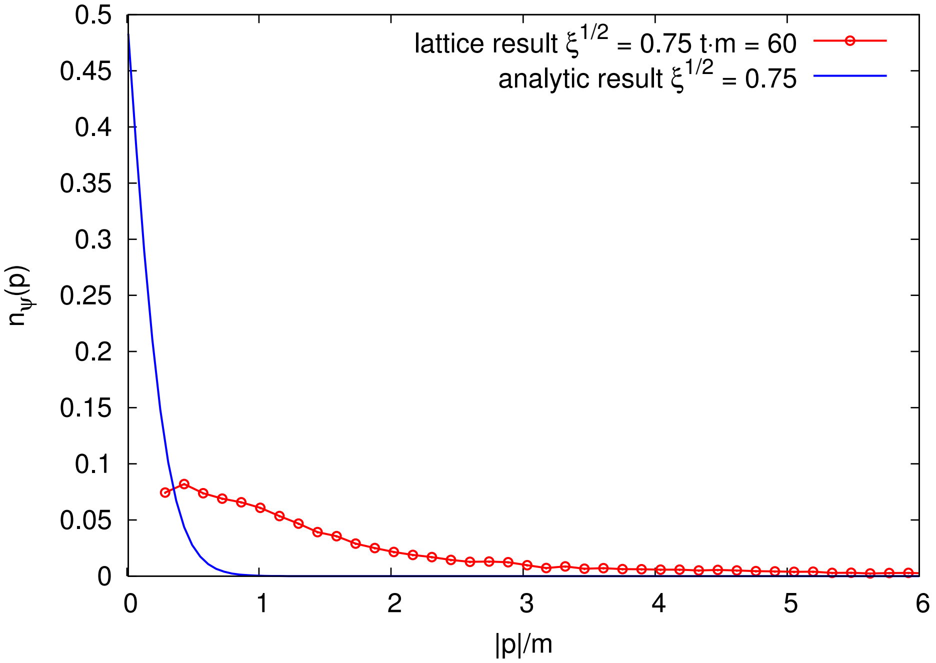

Figure 5.20.: Comparison between lattice results and analytical leading-order predictions for fermion spectra after symmertry breaking for $\sqrt{\xi} = 0.75$. The effective fermion mass for this coupling is $m_\psi \simeq 1.8m$.

Since a disagreement between analytical leading order and lattice results has become apparent already in Figs. 5.19 and 5.20 we did a direct comparison between these two approaches for a range of effective couplings in order to further quantify the differences. In Figs. 5.21 and 5.22 we plotted the total number as well as the total quasiparticle energy of fermions after symmetry breaking (third stage) as a function of $\sqrt{\xi}$. In both figures, we see the failure of the leading order approach, which underestimates the presented bulk quantities by up to three orders of magnitude for the strongest coupling presented. The errorbars are due to limited statistics, an issue which can be addressed in the future by averaging over more classical-statistical trajectories, but which has no effect on the qualitative behaviour of the system. We conclude that to correctly analyze production of massive fermions from the early stages of a bosonic instability a numerical investigation, which consistently includes effects of bosonic fluctuations, is indispensable.

5.2.2. Conclusions

What did we learn from this study of fermion production during tachyonic preheating? A primary and most astonishing result is the enhancement of fermion output by orders of

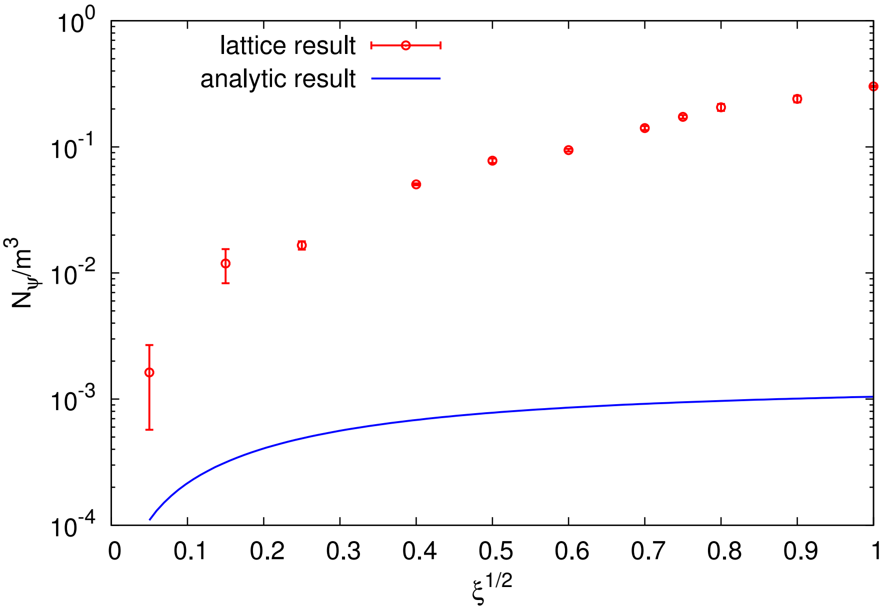

Figure 5.21.: Comparison between lattice results and analytical leading order predictions for the total number of fermions produced after symmertry breaking. Note larger differences for stronger couplings.

magnitude compared to leading-order analytic predictions. We observed that the amplification is much stronger than after the initial stages of parametric resonance for similar values of the effective coupling, although both types of instabilities lead to parametrically high bosonic occupation numbers. Another consequence of the Pauli principle and the increased number of fermions is that contrary to analytic expectations the typical momentum of produced particles becomes comparable to their mass, putting in question the validity of current non-relativistic approaches to fermion dynamics after preheating. These findings may prove their relevance for early Universe cosmology in future studies of particle abundances during reheating after inflation.

Of course, computational and numerical limitations allowed us to explore only a window of the available parameter space in the chosen model of preheating. Since recent experimental observations [101] promise to shed some light onto the microscopic details of inflation and constrain available inflationary models, we believe that they could put some boundaries on the physically relevant set of parameters in the future. In this case, new studies of preheating for alternative combinations of masses and couplings or entirely different models would be appropriate.

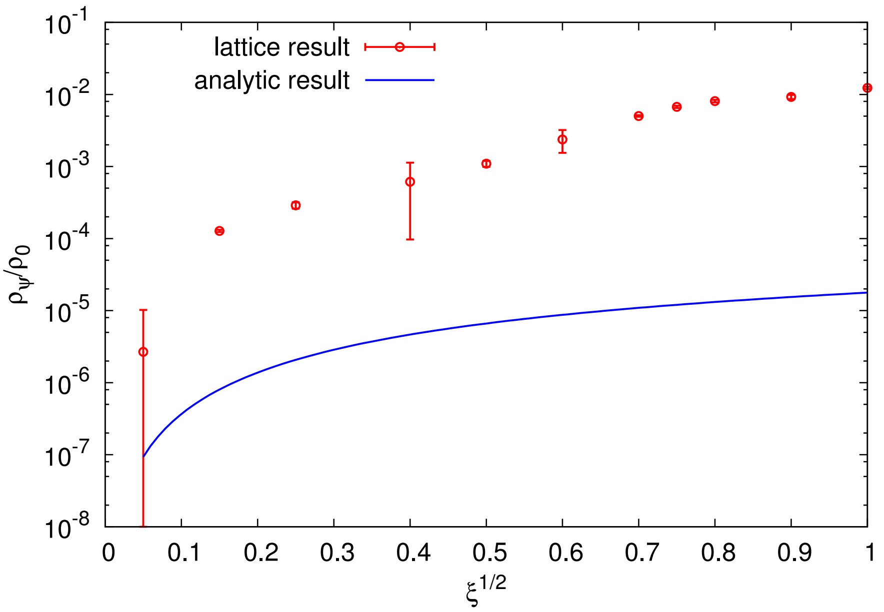

Figure 5.22.: Comparison between lattice results and analytical leading order predictions for the fraction of the initial energy contained in fermionic quasiparticles after symmetry breaking. The errors here are larger due to UV artefacts which are less important for particle numbers.

Chapter 6.

Gauge Theories with Fermions

The most successful current physical theory, the Standard Model, is a gauge theory. Two of its main ingredients, QED (quantum electrodynamics) and QCD (quantum chromodynamics), are gauge theories as well. These examples should illustrate the importance of studying particle production in theories with a local gauge symmetry. In the next chapter we will consider fermion production in a lower dimensional version of QED and in the two color version of QCD. First two sections will be dedicated to studies of Schwinger effect in 1 + 1 dimensions, this theory exhibits confinement, a property usually associated with full QCD in $3+1$ dimensions. We will investigate the non-perturbative decay of electric fields into fermions and the build-up of electric strings between separated charges. A consistent picture for the dynamical process of string breaking will be presented and extended towards multiple string breaking scenarios. In two color QCD we will concentrate on studies of quark production during early pre-equilibrium stages of heavy-ion collisions. Here three different models of initial conditions will be considered, ones that are dominated by instabilities and those starting immediately from an overpopulated gluonic state. Evidence for the existence of a universal isotropic scaling solution for quarks, accompanying the turbulent gluonic energy cascade, will be presented.

6.1. Schwinger model

In the following section we present real-time dynamics of particle production in the massive Schwinger model. The theoretical description of the non-perturbative phenomenon of Schwinger pair production in quantum field theory out of equilibrium is a demanding task and very little is known so far for realistic scenarios. Most current approaches assume the electromagnetic field as being an external one with a one-dimensional inhomogeneity, so that the problem of particle production can be mapped onto a one-dimensional quantum mechanical scattering problem [102, 103]. This approach neglects, in particular, the backreaction of the created fermion–anti-fermion pairs on the electromagnetic field. This is closely related to kinetic descriptions in terms of a momentum dependent distribution function of pairs in collisionless (Vlasov) approximations [104, 105, 106, 107, 108, 109]. For multi-dimensional inhomogeneities, more advanced approaches such as semi-classical approximations of the vacuum effective action [110] or the Dirac-Heisenberg-Wigner phase space formulation [111, 112] have been applied. However, to describe strongly inhomogeneous field configurations including the full back-reaction of the produced particles remains a theoretical challenge. In view of the potential experimental applications it is crucial to devise new theoretical methods which can deal with this situation.

This is done here by the already introduced real-time lattice simulations with fermions. In this non-perturbative approach the full quantum dynamics of fermions is included while the gauge field dynamics can be accurately represented by classical-statistical simulations for relevant field strengths. As the inclusion of dynamical fermions can become numerically very expensive, the real-time evolution of fermions is taken into account by means of a low-cost fermion algorithm [23].

Instead of going directly to full $3+1$ dimensional QED we decided to apply these techniques to QED in $1+1$ dimensions – the massive Schwinger model [113, 114] first, in order to compare with established continuum results and to develop and improve gauge theory specific numerical applications of the lattice fermion approach. Introducing a lattice generalization of the Dirac-Heisenberg-Wigner function, we show that the simulations accurately reproduce the results described by the Schwinger formula in the limit of a static background field. We discuss the decay of the field due to the backreaction of the created fermion–anti-fermion pairs and apply the approach to strongly inhomogeneous gauge fields. For these fields we compute for the first time the backreaction of the created pairs on the gauge fields. Most strikingly, we find that a self-consistent electric field between the produced fermion and the anti-fermion bunch builds up for times exceeding the initial pulse duration. The two bunches consisting of particles and anti-particles act as a capacitor, creating a homogeneous electric field between them, which can be represented in terms of a linear rising potential.

This section is organized in the following way: In Sec. 6.1.1 we briefly review the low-cost fermion algorithm and derive the real-time lattice equations of motion for the massive Schwinger model. Additionally, we construct a lattice generalization of the Dirac-Heisenberg-Wigner function which is subsequently used as a read-out tool for fermionic distributions. In Sec. 6.1.2 we first apply this formalism to a static electric background field and compare to the Schwinger formula. We then discuss the decay of the background field due to the backreaction of the created fermion–anti-fermion pairs. As a second example, we investigate the pair creation process in the presence of a space- and time-dependent electric field. In Sec. 6.1.3 we conclude and give an outlook. Some less important computational details have been moved to the appendices A and B.

6.1.1. Real-time lattice gauge theory

Continuum formulation

We consider QED in 1 + 1 dimensions, which is defined in the continuum by the action

$$\mathcal{S} = \int d^2x \left(\bar{\psi}[i\gamma^\mu D_\mu - m]\psi - \frac{1}{4}\mathcal{F}^{\mu\nu}\mathcal{F}_{\mu\nu} \right), \tag{6.1}$$

with the covariant derivative $D_\mu = \partial_\mu + ie\mathcal{A}_\mu$ ensuring gauge invariance of the action under local $U(1)$ transformations

$$\psi \to \psi e^{ie\Lambda} \quad , \quad \mathcal{A}_\mu \to \mathcal{A}_\mu - \partial_\mu \Lambda \; . \tag{6.2}$$

Here $\mu = 0, 1$ as space-time is only two-dimensional with $x^0 \equiv t$ and $x^1 \equiv x$. The field strength tensor $\mathcal{F}^{\mu\nu} = \partial^\mu \mathcal{A}^\nu - \partial^\nu \mathcal{A}^\mu$ possesses only one non-trivial component which is regarded as the electric field:

$$\mathcal{F}^{10} = -\mathcal{F}^{01} = E(x, t) \; . \tag{6.3}$$

We will frequently consider temporal axial gauge with $\mathcal{A}_0(x, t) = 0$ and simply denote the spatial component of the vector potential as $\mathcal{A}(x, t)$.[1] One observes that the electric field $E(x, t)$ is the canonical momentum conjugate to $\mathcal{A}(x, t)$.

The Dirac algebra is composed of two Dirac gamma matrices only:

$$\{\gamma^\mu, \gamma^\nu\} = 2g^{\mu\nu} \qquad \text{with} \qquad (\gamma^\mu)^\dagger = \gamma^0\gamma^\mu\gamma^0 \; , \tag{6.4}$$

with $g^{\mu\nu} = \mathrm{diag}(1, -1)$. This algebra may be represented in terms of the first two Pauli matrices $\gamma^0 \equiv \sigma_1$ and $\gamma^1 \equiv -i\sigma_2$. Moreover, the chirality matrix

$$\{\gamma^\mu, \gamma_5\} = 0 \qquad \text{with} \qquad (\gamma_5)^\dagger = \gamma_5 \; , \; (\gamma_5)^2 = 1 \; , \tag{6.5}$$

can be defined in terms of the third Pauli matrix $\gamma_5 \equiv \sigma_3$. As a consequence, the spinors ψ and $\bar{\psi}$ are two-component field operators, obeying the equal-time anticommutation relation:

$$\{\psi(x, t), \bar{\psi}(y, t)\} = \gamma^0 \delta(x - y) \; . \tag{6.6}$$

Time evolution equations

As introduced before (2.1.2), in the classical-statistical theory observables are calculated as ensemble averages of solutions of Maxwell's equation

$$\partial_\mu \mathcal{F}^{\mu\nu}(x, t) = \langle j^\nu(x, t) \rangle \tag{6.7}$$

---

[1] We note that this incomplete gauge choice leaves a residual gauge invariance under time-independent gauge transformations.

starting from different canonical field variables at initial time t_0, here $\mathcal{A}_{t_0}(x) = \mathcal{A}(x, t_0)$ and $E_{t_0}(x) = E(x, t_0)$. The values for the canonical field variables at initial time are distributed according to a normalized phase-space density functional $W[\mathcal{A}_{t_0}, E_{t_0}]$, such that an observable $\langle O \rangle$ is given by [64, 65]:

$$\langle O \rangle = \int D\mathcal{A}_{t_0} DE_{t_0}\, W[\mathcal{A}_{t_0}, E_{t_0}]\, O_{\mathrm{cl}}[\mathcal{A}_{t_0}, E_{t_0}]\ . \tag{6.8}$$

Here $O_{\mathrm{cl}}[\mathcal{A}_{t_0}, E_{t_0}] = \int D\mathcal{A}\, O[\mathcal{A}]\, \delta(\mathcal{A} - \mathcal{A}_{\mathrm{cl}}[\mathcal{A}_{t_0}, E_{t_0}])$, where $\mathcal{A}_{\mathrm{cl}}[\mathcal{A}_{t_0}, E_{t_0}]$ is the solution of the classical field equation (6.7) with initial conditions $\mathcal{A}_{\mathrm{cl}} = \mathcal{A}_{t_0}$ and $E_{\mathrm{cl}} = E_{t_0}$ at initial time t_0. Ensemble averages at initial time are taken to correspond to the respective quantum expectation values for the gauge fields. Similar to our toy model in 2.1.2 the gauge field dynamics in the classical-statistical approximation is accurately described in the presence of sufficiently high occupation numbers or fields, which is in general the case for the relevant field strengths for pair production. It breaks down once the typical gauge field occupancies become of order unity.

The subsequent time evolution then follows from (6.7) with

$$\langle j^\nu(x,t) \rangle = \frac{e}{2}\, \langle [\bar{\psi}(x,t), \gamma^\nu \psi(x,t)] \rangle\ , \tag{6.9}$$

where the expectation value is taken with respect to the initial state of the spinor field. We will restrict ourselves to the Dirac vacuum within the current investigation. The equations of motion for the spinors read:

$$i\gamma^\mu D_\mu \psi(x,t) = m\psi(x,t)\ , \tag{6.10a}$$

$$iD^*_\mu \bar{\psi}(x,t)\gamma^\mu = -m\bar{\psi}(x,t)\ . \tag{6.10b}$$

Since the fermions appear only quadratically in the action (6.1) these equations are exact for given classical gauge field configuration.

Equivalently, the above equations can be conveniently expressed in terms of the equal-time statistical propagator

$$F(x,y;t) \equiv \frac{1}{2}\langle [\psi(x,t), \bar{\psi}(y,t)] \rangle\ , \tag{6.11}$$

which yields the closed system of equations:

$$i\gamma^\mu D_{x,\mu} F(x,y;t) = mF(x,y;t)\ , \tag{6.12a}$$

$$iD^*_{\mu,y} F(x,y;t)\gamma^\mu = -mF(x,y;t)\ , \tag{6.12b}$$

$$\partial_\mu \mathcal{F}^{\mu\nu}(x,t) = -e\,\mathrm{Tr}\left[\gamma^\nu F(x,x;t)\right]\ . \tag{6.12c}$$

We note that the gauge field dynamics in 1 + 1 dimensions is special since it is governed by the fermionic backreaction only. Therefore, we do not consider sampling over initial gauge field configurations in this work.

Initial conditions and low-cost fermions

We have to solve the Cauchy problem (6.12) in order to calculate fermion–anti-fermion pair production. Accordingly, we need to provide an initial value for the statistical propagator at $t_0 = 0$. To this end, we consider an asymptotic Dirac vacuum – corresponding to zero particle number and vanishing gauge field – and employ the framework of canonical quantization in 1 + 1 dimensions:

$$\psi(x,t) = \int \frac{dp}{2\pi} e^{ipx} [u(p)a(p)e^{-i\omega t} + v(-p)b^\dagger(-p)e^{i\omega t}] \,, \tag{6.13}$$

with $\omega = \sqrt{m^2 + p^2}$ and anti-commuting creation and annihilation operators

$$\{a(p), a^\dagger(p')\} = \{b(p), b^\dagger(p')\} = 2\pi\,\delta(p - p') \,, \tag{6.14}$$

whereas all other anti-commutators vanish. An explicit representation of the eigenspinors is given by

$$u(p) = \frac{1}{\sqrt{2\omega(\omega+p)}} \begin{pmatrix} \omega + p \\ m \end{pmatrix} \,, \tag{6.15a}$$

$$v(p) = \frac{1}{\sqrt{2\omega(\omega+p)}} \begin{pmatrix} \omega + p \\ -m \end{pmatrix} \,, \tag{6.15b}$$

fulfilling the orthogonality relations:

$$u^\dagger(p)u(p) = 1 = v^\dagger(p)v(p) \;\;,\;\; u^\dagger(p)v(-p) = 0 \,. \tag{6.16}$$

Because of the fact that the asymptotic Dirac vacuum is homogeneous in space and time, we obtain the initial value

$$F(x,y;t_0) = \int \frac{dp}{2\pi} e^{ip(x-y)} \frac{m - p\gamma^1}{2\omega} \,, \tag{6.17}$$

which is, up to differences because of dimensionality, same as in scalar theories considered in previous chapters.

In the massive Schwinger model the description of fermion dynamics may be based on a mode function expansion [22]. This treatment can be well suited for low dimensional systems but becomes computationally too expensive in higher dimensions. In view of later applications of our approach to 3 + 1 dimensional non-Abelian gauge theory, we perform a stochastic integration of an equivalent set of equations with the male/female method 4.2. To this end, we introduce ensembles of classical stochastic spinors male $\psi_M(x,t)$ and female $\psi_F(x,t)$ spinor fields. Given these c-number spinors, we define:

$$F_{\text{sto}}(x,y;t) \equiv \langle \psi_M(x,t)\bar{\psi}_F(y,t) \rangle = \langle \psi_F(x,t)\bar{\psi}_M(y,t) \rangle \,, \tag{6.18}$$

where here $\langle ... \rangle$ is understood as an ensemble average. The requirement

$$F_{\text{sto}}(x, y; t) \overset{!}{=} F(x, y; t) \tag{6.19}$$

is met provided that the stochastic spinors $\psi_g(x,t)$, with the gender index $g = \{M, F\}$ both satisfy the Dirac equation (6.10a) and $F_{\text{sto}}(x, y; t)$ takes the initial value (6.17). This second requirement is achieved by initializing the stochastic spinors according to

$$\psi_g(x, t_0) = \int \frac{dp}{2\pi} e^{ipx} \frac{1}{\sqrt{2}} [u(p)\xi(p) \pm v(-p)\eta(p)] \,, \tag{6.20}$$

with complex random variables $\xi(p)$ and $\eta(p)$. Note that the male and female spinors only differ by the sign of the antiparticle component. In order to reproduce the initial value (6.17), the random variables are sampled according to

$$\langle \xi(p)\xi^*(p') \rangle = \langle \eta(p)\eta^*(p') \rangle = (2\pi)\delta(p - p') \,, \tag{6.21}$$

whereas all other correlators vanish.

In an actual simulation employing male/female fermions, the closed system (6.12) is solved in the form:

$$\begin{aligned} i\gamma^\mu D_\mu \psi_g(x,t) &= m\psi_g(x,t) \,, & (6.22a) \\ \partial_\mu \mathcal{F}^{\mu\nu}(x,t) &= -e \operatorname{Tr}\left[\gamma^\nu F_{\text{sto}}(x, x; t)\right] \,. & (6.22b) \end{aligned}$$

The stochastic spinors $\psi_g(x,t)$ are evolved in time independently and the ensemble average $\langle ... \rangle$ appearing in the definition (6.18) is approximated by an average over a sufficiently large number N_{sto} of pairs of male/female spinors. While the computational cost of the mode function approach scales with the volume of the phase space, i.e. N^2 in our case, the resource requirements of male/female fermions are proportional to just $N \times N_{\text{sto}}$.

6.1.1.1. Lattice formulation

We solve the equations of motion (6.22) on a 1 + 1 dimensional space-time lattice. For the spatial sublattice, we define:

$$\Lambda = \left\{ l \,\middle|\, \frac{x}{a_s} \in \{0, ..., N-1\} \right\} \,, \tag{6.23}$$

with the spatial lattice spacing a_s and the total number of spatial lattice sites N. A point on the space-time lattice is then denoted by $\mathbf{x} \equiv (l, j)$ with the temporal lattice spacing a_t such that $t = a_t j$. We employ periodic boundary conditions in the compactified spatial direction whereas no periodicity assumptions apply for the non-compact temporal direction. The lattice action governing the dynamics is then composed of a pure gauge part as well as part describing the fermions, including their interaction with the gauge field.

Pure gauge part

In order to put the gauge fields on the lattice, we use the compact formulation of a gauge theory with $U(1)$ symmetry. The parallel transporter $U_\mu(\mathbf{x})$ is associated with the link from a lattice point $\mathbf{x}$ to a neighboring point $\mathbf{x}+\hat{\mu}$ in the direction of the space-time lattice axis $\mu = 0, 1$:

$$U_\mu(\mathbf{x}) = e^{iea_\mu \mathcal{A}_\mu(\mathbf{x})} . \tag{6.24}$$

The link variable obeys $U_\mu^*(\mathbf{x}) = U_\mu^{-1}(\mathbf{x})$ and we use the definition $U_{-\mu}(\mathbf{x}) = U_\mu^*(\mathbf{x}-\hat{\mu})$. The continuum gauge transformation (6.2) translates to

$$\psi(\mathbf{x}) \rightarrow \Omega(\mathbf{x})\psi(\mathbf{x}) , \tag{6.25a}$$

$$U_\mu(\mathbf{x}) \rightarrow \Omega(\mathbf{x})U_\mu(\mathbf{x})\Omega^*(\mathbf{x}+\hat{\mu}) , \tag{6.25b}$$

with $\Omega \in U(1)$. Given the gauge-dependent link variable, we define the gauge-invariant plaquette variable:

$$U_{\mu\nu}(\mathbf{x}) = U_\mu(\mathbf{x})U_\nu(\mathbf{x}+\hat{\mu})U_\mu^*(\mathbf{x}+\hat{\nu})U_\nu^*(\mathbf{x}) . \tag{6.26}$$

Disregarding higher order terms in the lattice spacings a_μ, we find:

$$U_{\mu\nu}(\mathbf{x}) = e^{iea_\mu a_\nu \mathcal{F}_{\mu\nu}(\mathbf{x})} . \tag{6.27}$$

Accordingly, the pure gauge part of the action can be written as

$$\mathcal{S}_g[U] = \frac{1}{e^2 a_s a_t} \sum_{\mathbf{x}} \mathrm{Re}\,[1 - U_{01}(\mathbf{x})] . \tag{6.28}$$

Moreover, the electric field (6.3) is given by

$$E(\mathbf{x}) = \frac{1}{ea_s a_t} \mathrm{Im}\,[U_{01}(\mathbf{x})] . \tag{6.29}$$

Dirac and interaction part

Using a symmetric finite difference approximation for the first derivatives, the naive discretization of the fermionic part is given by

$$\mathcal{S}_f^{(0)}[\psi, \bar{\psi}, U] = a_t a_s \sum_{\mathbf{x}} \bar{\psi}(\mathbf{x}) \left[i\gamma^\mu \frac{U_\mu(\mathbf{x})\psi(\mathbf{x}+\hat{\mu}) - U_{-\mu}(\mathbf{x})\psi(\mathbf{x}-\hat{\mu})}{2a_\mu} - m\psi(\mathbf{x}) \right] , \tag{6.30}$$

where the gender index is omitted for simplicity. This expression is gauge-invariant under lattice gauge transformations (6.25), however, it also gives rise to unphysical fermion doublers 4.3.

The spatial doublers, corresponding to high-momentum excitations showing a low-energy dispersion relation, are conveniently suppressed by adding a gauge-invariant Wilson term in the action:

$$-\frac{a_s}{2}\int d^2x\,\bar{\psi}D_1D^1\psi\,, \tag{6.31}$$

which vanishes in the continuum limit $a_s \to 0$. This additional term ensures that only low-momentum excitations show a low-energy dispersion relation. In the lattice implementation, this corresponds to adding one more term to the action:

$$\mathcal{S}_f^{(W)}[\psi,\bar{\psi},U] = a_t a_s \sum_{\mathbf{x}} \bar{\psi}(\mathbf{x}) \times \left[\frac{U_1(\mathbf{x})\psi(\mathbf{x}+\hat{1}) - 2\psi(\mathbf{x}) + U_{-1}(\mathbf{x})\psi(\mathbf{x}-\hat{1})}{2a_s}\right]. \tag{6.32}$$

We do not include a temporal Wilson term as this would turn the Dirac equation into a second order differential equation in time. The temporal doublers are avoided provided that we initialize only the physical mode and choose the temporal lattice spacing to be much smaller than the spatial lattice spacing $a_t \ll a_s$ [22, 23, 89].

The construction of the stochastic spinor ensemble on the space-time lattice follows the same lines as in section 4.3 with appropriate definition of lattice momenta. Here the mass term is modified due to the scalar spatial Wilson term

$$\tilde{m} = m + \frac{2}{a_s}\sin^2\left(\frac{\pi q}{N}\right)\,, \tag{6.33}$$

while the complex random variables $\xi(q)$ and $\eta(q)$ are sampled by applying same techniques as in 4.3.

Lattice equations of motion

To simplify simulations afterwards, we use the gauge freedom and employ the lattice equivalent of the temporal axial gauge: $U_0(\mathbf{x}) = 1$ for the equations of motion. Stationarity of the lattice action

$$\mathcal{S}[\psi,\bar{\psi},U] = \mathcal{S}_g[U] + \mathcal{S}_f^{(0)}[\psi,\bar{\psi},U] + \mathcal{S}_f^{(W)}[\psi,\bar{\psi},U] \tag{6.34}$$

with respect to the temporal link $U_0(\mathbf{x})$ results in the discretized version of the Gauss law:

$$E(\mathbf{x}) - E(\mathbf{x}-\hat{1}) = \frac{ea_s}{2}\bar{\psi}(\mathbf{x})\gamma^0\psi(\mathbf{x}+\hat{0}) + c.c. \tag{6.35}$$

This equation is a constraint which is fulfilled during the time evolution for the considered initial conditions.

The stationary condition of the action with respect to the spatial link $U_1(\mathbf{x})$, on the other hand, results in the equation of motion:

$$E(\mathbf{x}) - E(\mathbf{x}-\hat{0}) = -\frac{ea_t}{2}\bar{\psi}(\mathbf{x})[\gamma^1 - i]U_1(\mathbf{x})\psi(\mathbf{x}+\hat{1}) + c.c. \tag{6.36}$$

Finally, the stationarity condition of the action with respect to the Dirac field $\bar{\psi}(\mathbf{x})$ gives:

$$\begin{aligned}\psi(x+\hat{t}) &= \psi(x-\hat{t}) - 2ia_t m\gamma^0\psi(x) - \frac{a_t}{a_s}\gamma^0\gamma^1\left[U_1(x)\psi(x+\hat{1}) - U_1^\dagger(x-\hat{1})\psi(x-\hat{1})\right]\\ &+ \frac{ia_t}{a_s}\gamma^0\left[U_1(x)\psi(x+\hat{1}) + U_1^\dagger(x-\hat{1})\psi(x-\hat{1}) - 2\psi(x)\right].\end{aligned} \tag{6.37}$$

The set of equations (6.35)–(6.37) is the lattice version of (6.22) in temporal axial gauge including a spatial Wilson term.

In order to solve the Cauchy problem, we have to provide the following initial values at $t_0 = a_t j_0 = 0$:

$$E(\mathbf{x}_0 - \hat{0}) \quad , \quad U_1(\mathbf{x}_0) \quad , \quad \psi(\mathbf{x}_0 - \hat{0}) \quad , \quad \psi(\mathbf{x}_0)$$

with $\mathbf{x}_0 = (l, j_0)$ for all $l \in \Lambda$. Most notably, we have to choose initial values for the spinors at $j_0 - 1$ and j_0, which is a consequence of the chosen leapfrog algorithm. To be able to initialize them we assume a free field evolution at initial times.

The algorithm, which is a variant of the one introduced in [115], can then be summarized in the following way:

1. *Electric field evolution:* Given $E(\mathbf{x}-\hat{0})$, $U_1(\mathbf{x})$ and $\psi(\mathbf{x})$ we evolve the electric field to $E(\mathbf{x})$ according to (6.36).

2. *Dirac field evolution:* Given $\psi(\mathbf{x}-\hat{0})$, $\psi(\mathbf{x})$ and $U_1(\mathbf{x})$ we evolve the Dirac field to $\psi(\mathbf{x}+\hat{0})$ according to (6.37).

3. *Temporal plaquette:* We evaluate the temporal plaquette $U_{01}(\mathbf{x})$ according to (6.27):

$$U_{01}(\mathbf{x}) = e^{iea_s a_t \mathcal{F}_{01}(\mathbf{x})} = e^{iea_s a_t E(\mathbf{x})}\,. \tag{6.38}$$

4. *Spatial link evolution:* The link variable $U_1(\mathbf{x}+\hat{0})$ is calculated from the temporal plaquette $U_{01}(\mathbf{x})$ in temporal axial gauge according to (6.26):

$$U_1(\mathbf{x}+\hat{0}) = U_{01}(\mathbf{x})U_1(\mathbf{x})\,. \tag{6.39}$$

5. Reiterate the steps 1 – 4.

6.1.1.2. Gauge-invariant correlation functions

In order to compare our simulation results with typical discussions using the Dirac-Heisenberg-Wigner phase-space approach [111, 112, 116, 117, 118, 119, 120], we define suitable gauge invariant two-point correlation functions on the lattice.

Continuum Wigner function

Starting from the continuum expression for the statistical propagator (6.11), a gauge-invariant generalization may be defined as:

$$\tilde{F}(x_1, x_2; t) = \exp\left(ie \int_{x_2}^{x_1} dx \mathcal{A}(x, t) \right) F(x_1, x_2; t) \,. \tag{6.40}$$

The Wilson line factor ensures gauge invariance under local $U(1)$ transformations. The Fourier transformation with respect to the relative coordinate defines the Wigner function:

$$\mathcal{W}(x, p, t) \equiv - \int dy e^{-ipy} \tilde{F}\,(x + y/2, x - y/2; t) \,, \tag{6.41}$$

with $x = (x_1 + x_2)/2$ and $y = x_1 - x_2$. The Wilson line factor in (6.40) is not unique, however, a physical sensible interpretation of p as kinetic momentum forces the integration path to be chosen along the straight line. Equivalently to (6.41), we may also write:

$$\mathcal{W}(x, p, t) = - \int dz e^{2ip(x-z)} \tilde{F}(z, 2x - z; t) + \gamma.c. \tag{6.42}$$

with the abbreviation:

$$D + \gamma.c. \equiv D + \gamma^0 D^\dagger \gamma^0 \,. \tag{6.43}$$

As the Wigner function is in the Dirac algebra and fulfills $\mathcal{W}^\dagger = \gamma^0 \mathcal{W} \gamma^0$, one can decompose it in terms of its Dirac bilinears:

$$\mathcal{W} = \frac{1}{2} \left[\mathbb{s} + i\gamma_5 \mathbb{p} + \gamma^0 \mathbb{v}_0 - \gamma^1 \mathbb{v} \right] \,, \tag{6.44}$$

where all its irreducible components can be chosen to be real. Regarding the Dirac vacuum, which is described by the statistical propagator (6.17), the only non-vanishing components are given by:

$$\mathbb{s}_{\text{vac}}(x, p, t) = -\frac{m}{\omega} \quad , \quad \mathbb{v}_{\text{vac}}(x, p, t) = -\frac{p}{\omega} \,. \tag{6.45}$$

In terms of these components the total charge Q and the total energy $\mathcal{E}$ can be expressed as phase-space integrals:

$$Q = e \int d\Gamma \mathbb{v}_0(x, p, t) \,, \tag{6.46a}$$

$$\mathcal{E} = \int d\Gamma [m\mathbb{s}(x, p, t) + p\mathbb{v}(x, p, t)] + \frac{1}{2} \int dx E^2(x, t) \,, \tag{6.46b}$$

with the phase-space volume element $d\Gamma = dxdp/(2\pi)$. The integrands $\epsilon(x,p,t) = [m\mathbb{s}(x,p,t) + p\mathbb{v}(x,p,t)]$ and $\varrho(x,p,t) = \mathbb{v}_0(x,p,t)$ are regarded as energy pseudo-distribution and charge pseudo-distribution, respectively. We may define further quantities such as the particle number pseudo-distributions:

$$n^{\pm}(x,p,t) = \frac{\epsilon(x,p,t) - \epsilon_{\text{vac}}(x,p,t) \pm \omega\mathbb{v}_0(x,p,t)}{2\omega}\,, \tag{6.47}$$

which may be associated to the density of particles and anti-particles, respectively. Of course, in the interacting quantum theory the interpretation of these phase-space pseudo-distributions, collectively denoted as $m(x,p,t)$, has to be taken with care. We emphasize that our approach is not based on these quantities and we use them only for read-out and comparison with literature results. We will frequently consider also the partially integrated position space and momentum space marginal distributions:

$$m_{\mathcal{X}}(x,t) \equiv \int \frac{dp}{2\pi} m(x,p,t)\,, \tag{6.48a}$$

$$m_{\mathcal{P}}(p,t) \equiv \int dx\, m(x,p,t)\,, \tag{6.48b}$$

or the fully integrated quantities:

$$m(t) \equiv \int d\Gamma\, m(x,p,t)\,, \tag{6.49}$$

instead of the pseudo-distributions $m(x,p,t)$.

Lattice Wigner function

In order to adjust the above continuum treatment to the lattice, we have to account for the periodicity of the spatial lattice properly. Our approach is an extension of previous work on the discrete Wigner function in the context of signal processing [121].

We first define the gauge invariant generalization of the lattice statistical propagator according to:

$$\tilde{F}(l_1,l_2;j) = \mathcal{U}(l_1,l_2;j)F(l_1,l_2;j)\,, \tag{6.50}$$

where $\mathcal{U}(l_1,l_2;j)$ is the lattice analogue of the Wilson line factor along the straight line path. However, since the straight line path between two lattice points is not unique due the periodicity of the lattice, we choose to define it such that properties of the above standard continuum interpretation apply. It turns out that this requires taking the shortest path between two lattice points. Accordingly, for $\Delta l = l_1 - l_2 > 0$ we employ:

$$\Delta l \leq \frac{N}{2}: \qquad \mathcal{U} = \prod_{l=l_2}^{l_1-1} U_1(\mathbf{x})\,, \tag{6.51a}$$

$$\Delta l > \frac{N}{2}: \qquad \mathcal{U} = \prod_{l=l_1}^{N-1} U_1^*(\mathbf{x}) \times \prod_{l=0}^{l_2-1} U_1^*(\mathbf{x})\,. \tag{6.51b}$$

On the other hand, for $\Delta l < 0$ we use:

$$\Delta l > -\tfrac{N}{2}: \qquad \mathcal{U} = \prod_{l=l_1}^{l_2-1} U_1^*(\mathbf{x})\,, \tag{6.52a}$$

$$\Delta l \leq -\tfrac{N}{2}: \qquad \mathcal{U} = \prod_{l=l_2}^{N-1} U_1(\mathbf{x}) \times \prod_{l=0}^{l_1-1} U_1(\mathbf{x})\,. \tag{6.52b}$$

More precisely, we utilize the following Wigner lattices:

$$\Lambda_{\mathcal{W}} \;=\; \left\{ l \;\middle|\; \frac{2x}{a_s} \in \{0, ..., 2N-1\} \right\}\,, \tag{6.53a}$$

$$\tilde{\Lambda}_{\mathcal{W}} \;=\; \left\{ q \;\middle|\; \frac{Lp}{\pi} \in \{-N, ..., N-1\} \right\}\,, \tag{6.53b}$$

which have the same extent as the original ones Λ and $\tilde{\Lambda}$, however, each with twice as many grid points. We then define the lattice Wigner function according to

$$\begin{aligned} \mathcal{W}(l, q, j) \equiv{} & -\frac{a_s}{2} e^{\pi i l q/N} \\ & \times \sum_{k \in \Lambda} e^{-2\pi i k q/N} \tilde{F}(k, [l-k]_N; j) + \gamma.c. \end{aligned} \tag{6.54}$$

with $l \in \Lambda_{\mathcal{W}}$ and $q \in \tilde{\Lambda}_{\mathcal{W}}$. We account for the periodicity of the lattice by taking the module operation in the second argument of the statistical propagator:

$$[l-k]_N = (l-k) \bmod N\,. \tag{6.55}$$

This definition is such that we reproduce the above continuum expressions for the marginal distributions, as shown in Appendix A. Moreover, the lattice Wigner function (6.54) again fulfills $\mathcal{W}^\dagger = \gamma^0 \mathcal{W} \gamma^0$ so that the decomposition in terms of its Dirac bilinears (6.44) is possible.

In complete analogy to the continuum, we may then again define various pseudo distributions:

$$\varrho(l, q, t) \;=\; e\mathbb{v}_0(l, q, t)\,, \tag{6.56a}$$

$$\epsilon(l, q, t) \;=\; [\tilde{m}\mathbb{s}(l, q, t) + \tilde{q}\mathbb{v}(l, q, t)]\,, \tag{6.56b}$$

$$n^\pm(l, q, t) \;=\; \frac{\epsilon(l, q, t) - \epsilon_{\text{vac}}(l, q, t) \pm \tilde{\omega}\mathbb{v}_0(l, q, t)}{2\tilde{\omega}}\,, \tag{6.56c}$$

corresponding to charge, energy and particle/anti-particle number, respectively. Given these pseudo-distributions $m(l, q, t)$, the marginal distributions are defined via

$$m_{\mathcal{X}}(l, j) \;\equiv\; \frac{1}{2L} \sum_{q \in \tilde{\Lambda}_{\mathcal{W}}} m(l, q, j)\,, \tag{6.57a}$$

$$m_{\mathcal{P}}(q, j) \;\equiv\; \frac{a_s}{2} \sum_{l \in \Lambda_{\mathcal{W}}} m(l, q, j)\,, \tag{6.57b}$$

whereas the fully integrated quantities are given by

$$m(j) = \frac{1}{2N} \sum_{q \in \tilde{\Lambda}} \sum_{l \in \Lambda_{\mathcal{W}}} m(l, q, j) \, . \tag{6.58}$$

Here one should note the summation order in the last expression: The sum over $l \in \Lambda_{\mathcal{W}}$ yields the marginal distribution $m_{\mathcal{P}}(q, t)$ which is non-vanishing for even q only. Accordingly, the subsequent sum is just taken over $q \in \tilde{\Lambda}$.

6.1.2. Pair production simulations

We now come to the results which are based on the lattice approach presented in the previous section. As a first example, we consider a static electric background field, disregarding the backreaction of created fermion–anti-fermion pairs. This configuration can be solved analytically such that we can compare our lattice simulations with well established continuum results. Subsequently, we also include the backreaction of created fermion–anti-fermion pairs and discuss the decay of the gauge field which shuts pair production off after a characteristic time.

As a second example, we investigate the pair creation process in the presence of a space- and time-dependent electric field. Neglecting backreaction in a first step, we can compare to and complement previous investigations based on the continuum Dirac-Heisenberg-Wigner approach [119, 122]. Subsequently, we solve the full lattice evolution and compare.

6.1.2.1. Spatially homogeneous gauge field

We consider a static electric background field $E(x, t) = E_0$ in temporal axial gauge $\mathcal{A}_0 = 0$, represented by the vector potential

$$\mathcal{A}(t) = E_0 t \, . \tag{6.59}$$

Within the compact lattice formulation, this corresponds to a trivial temporal link $U_0(\mathbf{x}) = 1$ and the spatial link

$$U_1(\mathbf{x}) = e^{iea_t a_s E_0 j} \tag{6.60}$$

disregarding higher order terms in the lattice spacing. Moreover, we introduce the dimensionless field strength parameter

$$\epsilon = \frac{E_0}{E_c} \, , \tag{6.61}$$

with the critical Schwinger field strength $E_c = m^2/e$. For all subsequent numerical results we employ $e/m = 0.3$. In Appendix B we briefly review some analytic results, which are used for comparison in the following.

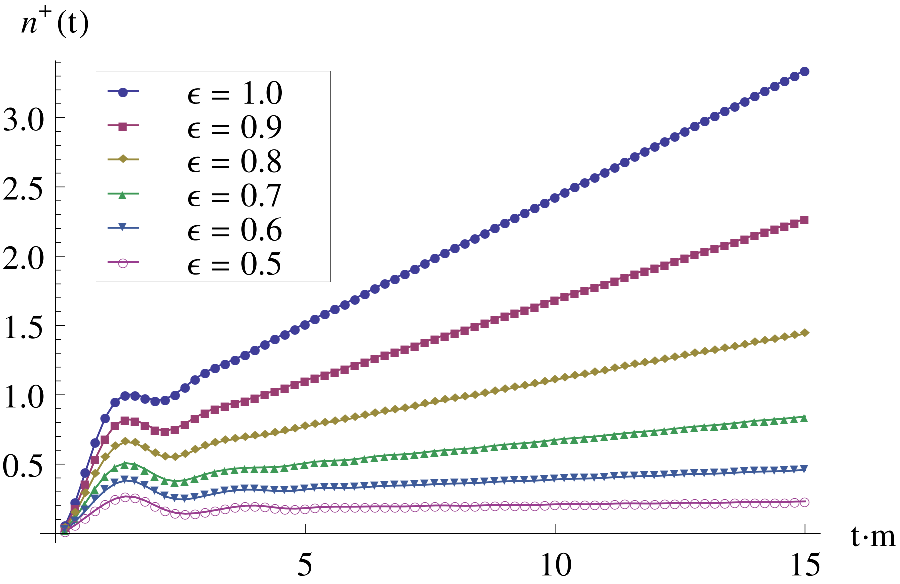

Figure 6.1.: Time evolution of the total particle number $n^+(t)$ for different values of ϵ. The parameters are $N_{\text{sto}} = 10^3$, $a_t = 0.00125/m$, $a_s = 0.025/m$, $N_s = 1024$ such that $L = 25.6/m$.

Particle production without backreaction

In this section we disregard the backreaction of created fermion–anti-fermion pairs on the electric field. This corresponds to neglecting the fermionic contributions in the gauge field equation of motion (6.36). Starting with the vacuum initial conditions for the fermions, this amounts to evolving the fermion equation (6.37) with a sudden switching-on of the electric field at initial time.

In Fig. 6.1 we show the time evolution of the total number of produced particles, $n^+(t)$, for various values of the dimensionless field strength parameter ϵ. Most notably, we observe two different regimes: At early times there is a transient oscillatory behavior superimposed which can be attributed to the sudden switching-on of the electric field. For $\epsilon = 1$ we estimate this oscillation to be exponentially damped with a characteristic rate $\gamma \simeq 1/m$, leading to a purely linear growth to very good accuracy after times of a few γ^{-1}.

The slope of the linear rise of $n^+(t)$ strongly depends on the value of ϵ. In order to extract its functional dependence, we perform a linear fit. For this we measure the change in the total number of particles Δn^+ which are produced during the time interval $T = 10/m$ for times large compared to γ^{-1}. In Fig. 6.2 we compare the slope for different values of ϵ with the analytical result from Appendix B:

$$\frac{\Delta n^+}{TLm^2} = \frac{\epsilon}{2\pi} \exp\left(-\frac{\pi}{\epsilon}\right) . \tag{6.62}$$

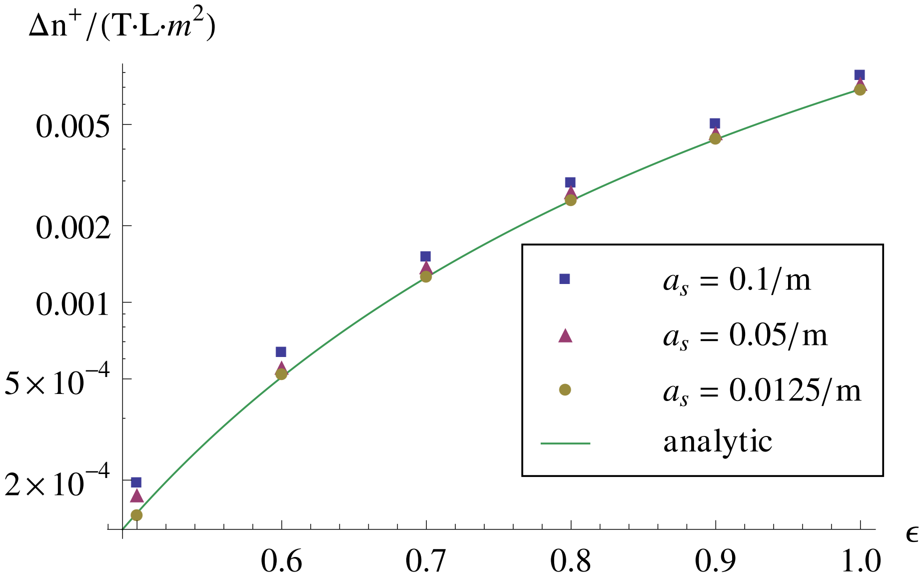

Figure 6.2.: Comparison of the analytical results (6.62) with the numerical fit for $L = 25.6/m$ and different lattice spacings a_s. The remaining parameters are $N_{\text{sto}} = 10^3$ and $a_t = a_s/20$.

We emphasize that for this analytical result the initial time is sent to the remote past such that it cannot reproduce the transient oscillatory regime. However, both the simulation and the analytical result should accurately agree for large enough times.

The lattice results are shown in Fig. 6.2 for different spatial lattice spacings a_s keeping the volume $L = a_s N$ constant, thus increasing N accordingly. One clearly observes that the simulation and the analytical result (6.62) fall nearly on top of each other for small enough a_s, indicating that we are close to the continuum limit in that case. As a matter of fact, we find that temporal discretization errors are quite negligible for $a_t \lesssim a_s/20$. This corroborates that the real-time lattice simulation is in fact capable of reproducing the analytic results in the continuum limit to very good accuracy.

In Fig. 6.3 we show the normalized particle number marginal distribution $n^+_{\mathcal{P}}(p,t)/L$, corresponding to the momentum spectrum of created particles (B.2), and compare it to the continuum value $f(p)$. In comparison to the integrated particle number shown above, the spectrum is not smooth but shows fluctuations due to the sampling of low-cost fermions. As a matter of fact, these fluctuations can be systematically reduced by taking N_{sto} larger. We find that it suffices to take the number N_{sto} of the order of 10^3 in order to accurately calculate integrated quantities such as $n^+(t)$. This is in contrast to the momentum spectrum $n^+_{\mathcal{P}}(p,t)$ where the number N_{sto} needed to be at least of the order of 10^4 to suppress the statistical fluctuations sufficiently and obtain sensible results. In contrast to the one-dimensional case considered here, the convergence is expected to be even better for three

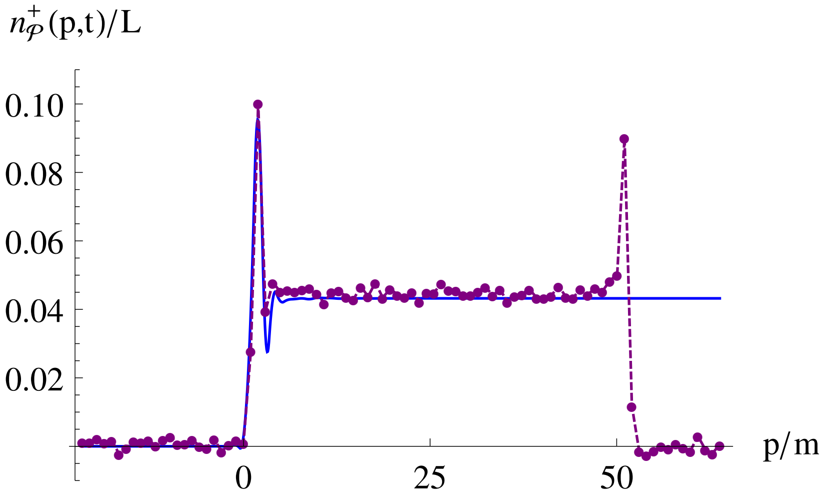

Figure 6.3.: Comparison of the continuum expression $f(p)$ (solid line) with the normalized particle number marginal distribution $n^+_{\mathcal{P}}(p,t)/L$ (dashed line) for $\epsilon = 1$ at $t = 50/m$. The parameters are $N_{\text{sto}} = 10^5$, $a_t = 0.00125/m$, $a_s = 0.025/m$, $N = 1024$ such that $L = 25.6/m$.

space dimensions where self-averaging plays a major role [7].

The established interpretation of $f(p)$ is such that electric field energy is taken and transformed into virtual fermion–anti-fermion pairs, showing up as the distinctive peak around momenta $p = 0$. If the applied field strength E_0 is large enough, i.e. of the order of E_c, these charged excitations can be separated over the Compton wavelength and become real fermion–anti-fermion pairs. These real particles are then further accelerated in the background electric field and achieve higher and higher momenta up to $p \to \infty$.

We observe good agreement of simulation and analytical results regarding the virtual fermion–anti-fermion peak around $p = 0$ as well as the overall magnitude of $n^+_{\mathcal{P}}(p,t)/L$. However, we observe a qualitatively different behavior for large momenta. This is due to the fact that the analytic result assumes an electric field which has existed for all times such that all momenta up to $p \to \infty$ are already occupied whereas we solve an initial value problem on the lattice. Accordingly, we observe a transient effect corresponding to the peak at high momenta propagating to higher and higher momenta during the time evolution.

Particle production with backreaction

We now include the backreaction of created fermion–anti-fermion pairs on the electric field. As a consequence, particle creation comes with a simultaneous decrease of the electric field due to energy conservation. This energy transfer from the gauge sector to the fermion sector finally results in a decay of the electric field.

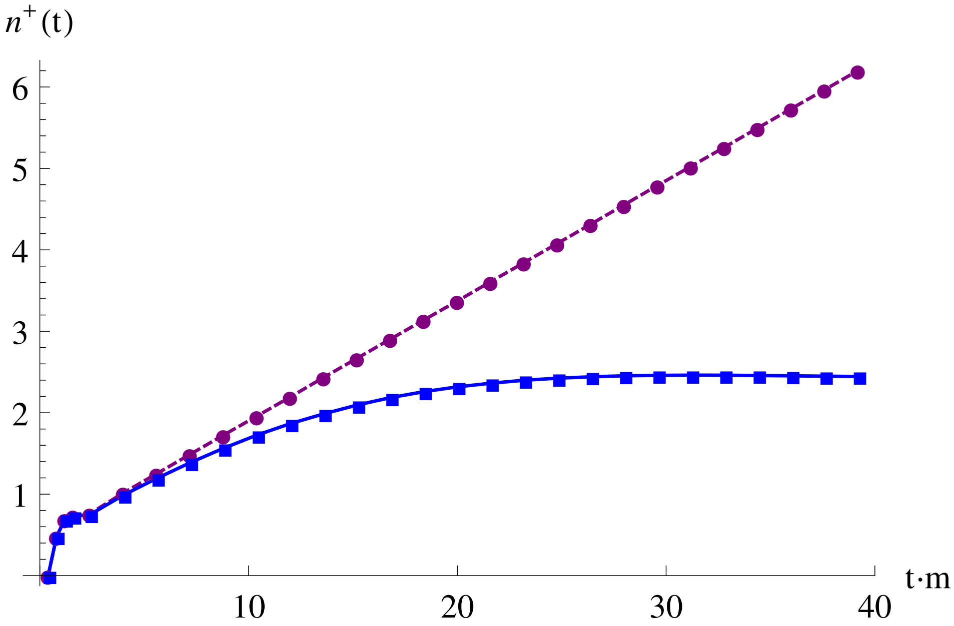

Figure 6.4.: Time evolution of the total particle number $n^+(t)$ with (solid line) and without (dashed line) backreaction for an initial value $\epsilon = 1$. The parameters are $N_{\text{sto}} = 10^4$, $a_t = 0.0025/m$, $a_s = 0.075/m$, $N = 256$ such that $L = 19.2/m$.

In Fig. 6.4 we compare the time evolution of the total particle number $n^+(t)$ for simulations with and without backreaction. We have already seen in the previous section that the particle number grows eventually linearly if we disregard the backreaction of created fermion–anti-fermion pairs on the electric field. However, this changes drastically if we include the backreaction mechanism: Following the transient regime at early times, the pair production rate immediately slows down once the pair creation process kicks in and the electric field is weakened. Eventually, this is getting to a point where the fermion–anti-fermion production process effectively stops and $n^+(t)$ levels off. This process happens on rather short time scales of the order of $\Delta t \sim 25/m$.

To see the long-time behavior, in Fig. 6.5 we show the particle number $n^+(t)$ and the electric field $E(t)$ for times up to $800/m$. Most notably, we observe the occurrence of plasma oscillations in accordance with previous investigations [104]: Starting from $t_0 = 0$, the magnitude of the electric field decreases due to the creation of fermion–anti-fermion pairs. Due to the backreaction mechanism, an internal electric field builds up so that the field eventually changes sign and grows until a first local minimum is achieved. The electric field then increases again, changes sign, reaches a local maximum and so forth. The oscillation frequency Ω increases with the number of produced fermions, in accordance with the expected parametric dependence.

The behavior of the particle number $n^+(t)$ follows from the oscillatory behavior of the

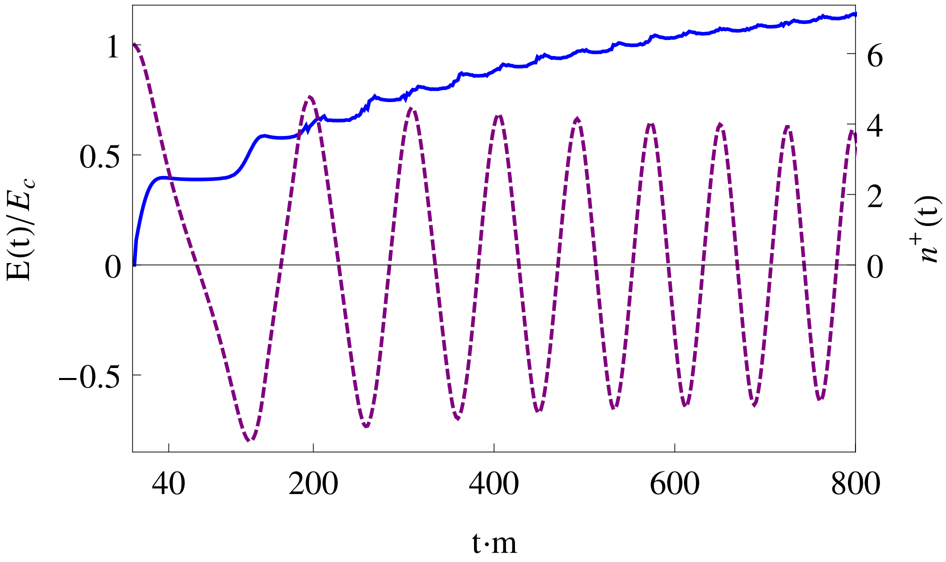

Figure 6.5.: Time evolution of the electric field $E(t)$ (dashed line) and the total particle number $n^+(t)$ (solid line) for an initial value $\epsilon = 1$ for a much longer time period. The parameters are as in Fig. 6.4.

electric field: Particle creation effectively terminates when the magnitude of the field strength drops below $\sim 0.5E_\mathrm{c}$, corresponding to the approximate plateaus in $n^+(t)$. However, at those instants of time at which the electric field reaches local extrema, fermions are created again. Due to the fact that the envelope of the electric field decreases with time, the particle number $n^+(t)$ assumes the shape of a staircase with decreasing step height.

We emphasize that the classicality condition $\langle\mathcal{A}\mathcal{A}\rangle \gg 1$ [64] is well fulfilled also after the backreaction effectively terminates the pair production: For an electric field amplitude E with characteristic oscillation frequency Ω the classicality condition reads $E^2/\Omega^2 \gg 1$. In our case $E \simeq E_c/2 = m^2/2e$ during these times such that with $\Omega \simeq \pi m/50$ for the employed coupling $e/m = 0.3$ we have $E^2/\Omega^2 \simeq 700$.

Moreover, in Fig. 6.6 we demonstrate that the energy transfer from the gauge sector to the fermion sector is in agreement with energy conservation.

Finally, in Fig. 6.7 we compare the normalized particle number marginal distributions $n^+_{\mathcal{P}}(p,t)/L$ for simulations with and without backreaction prior to the onset of plasma oscillations. We observe two major modifications if we include the backreaction:

First, the high-momentum peak is shifted to lower momenta. This is due to the fact that acceleration in an electric field is proportional to its field strength. Accordingly, particles are less accelerated and achieve lower momenta if the electric field is decreasing gradually.

Second, the overall magnitude of $n^+_{\mathcal{P}}(p,t)/L$ declines in the low-momentum regime. Again, this can be attributed to the decay of the electric field as the decrease of the field

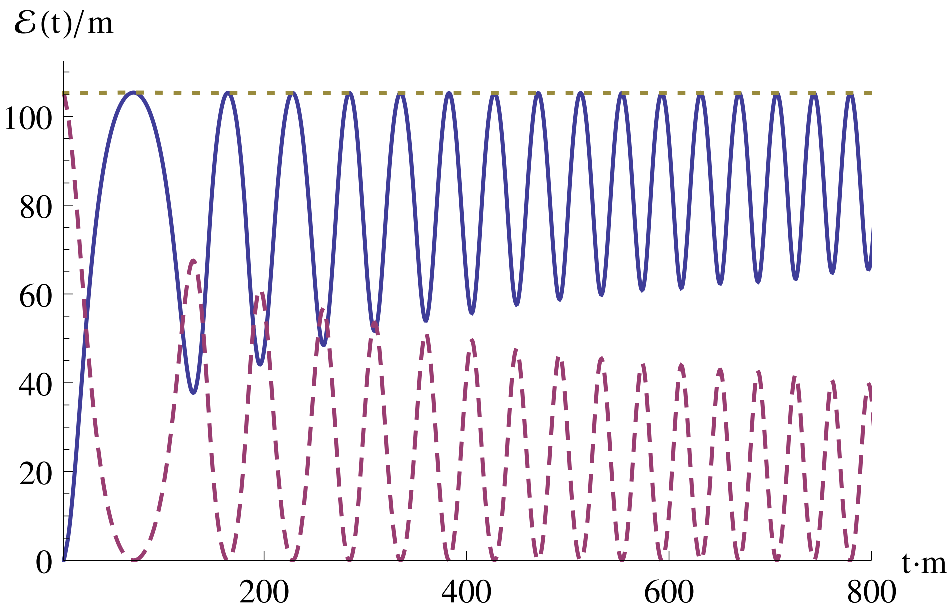

Figure 6.6.: Energy transfer between the fermionic sector (solid line) and the gauge sector (dashed line) for an initial value $\epsilon = 1$. The dotted line shows the total energy, with the fermion vacuum contribution being subtracted. The parameters are as in Fig. 6.4.

strength is accompanied by a drop in the pair production rate. Consequently, this gradual decrease of the pair production rate shows itself as a decreasing amplitude of $n^{+}_{\mathcal{P}}(p,t)/L$.

This simple picture changes rather drastically at late times because of the occurrence of plasma oscillations. In Fig. 6.8 we show the normalized particle number marginal distribution $n^{+}_{\mathcal{P}}(p,t)/L$ at different times. Due to the fact that the electric field changes its sign again and again, the fermions are accelerated back and forth in momentum space over and over again. The shaking of the fermions by the electric field has several implications:

In contrast to the wedge-shaped spectrum at early times, this results in a peaked marginal number distribution at late times. It has to be emphasized, however, that this peaked distribution still oscillates around $p = 0$ in accordance with the electric field. Moreover, owing to the ongoing creation of fermion–anti-fermion pairs at times when the electric field reaches its local extrema, the overall magnitude of $n^{+}_{\mathcal{P}}(p,t)/L$ increases as well.

6.1.2.2. Space- and time-dependent field

As a further example we consider an inhomogeneous electric background field which is localized in space and time:

$$E(x,t) = E_0 \operatorname{sech}^2(\omega t) \exp\left(-\frac{x^2}{2\lambda^2}\right), \tag{6.63}$$

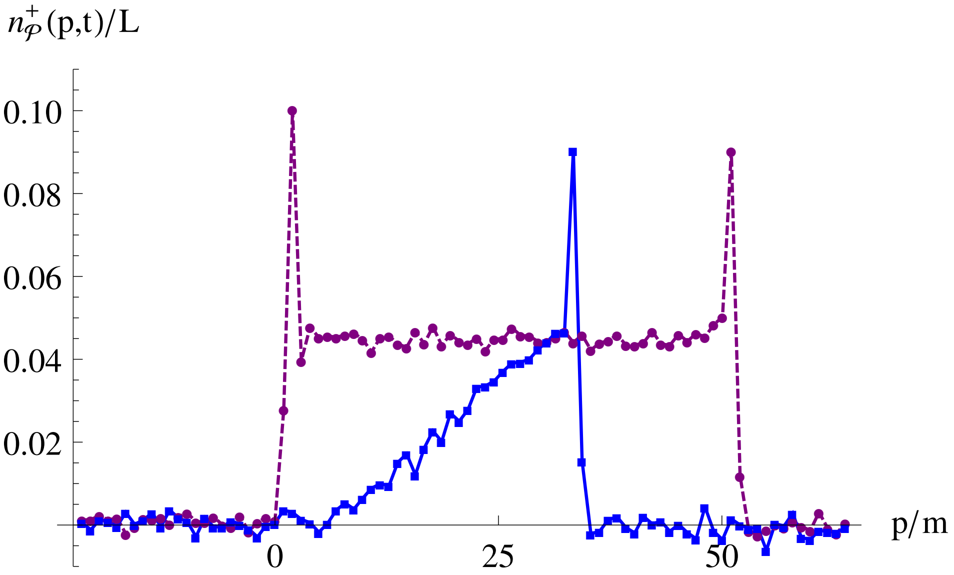

Figure 6.7.: Normalized particle number marginal distribution $n^+_{\mathcal{P}}(p,t)/L$ with (solid line) and without (dashed line) backreaction for an initial value $\epsilon = 1$ at $t = 50/m$. The parameters are $N_{\text{sto}} = 10^5$, $a_t = 0.00125/m$, $a_s = 0.025/m$, $N = 1024$ such that $L = 25.6/m$.

where ω and λ determine the duration and spatial extent of the pulse, respectively. Studies based on the continuum Dirac-Heisenberg-Wigner function only recently started to address such inhomogeneous configurations, disregarding the backreaction of created fermion–anti-fermion pairs [119, 122]. Here we are for the first time able to take this fermionic backreaction into account using our lattice techniques. This will allow us to discuss the striking phenomenon of a linear rising potential building up between produced fermion bunches for times exceeding the pulse duration.

Particle production without backreaction

In a first step, we solve the problem without taking into account backreaction. Consequently, we do not evolve the electric field according to (6.36) as it does not fulfill Maxwell's equation. We rather force the electric field to be given according to (6.63) at every space-time point and investigate the fermion–anti-fermion production in this given background field.

In Fig. 6.9 we show the position-space marginal distributions $n^\pm_{\mathcal{X}}(x,t)$ for three different times, with the electric field parameters $\epsilon = 1$, $\omega = 0.1m$ and $\lambda = 5/m$. One observes two qualitatively different regimes, corresponding to early times ('creation regime') and late times ('propagation regime').

The fermion–anti-fermion pair creation process takes place at early times, when charged

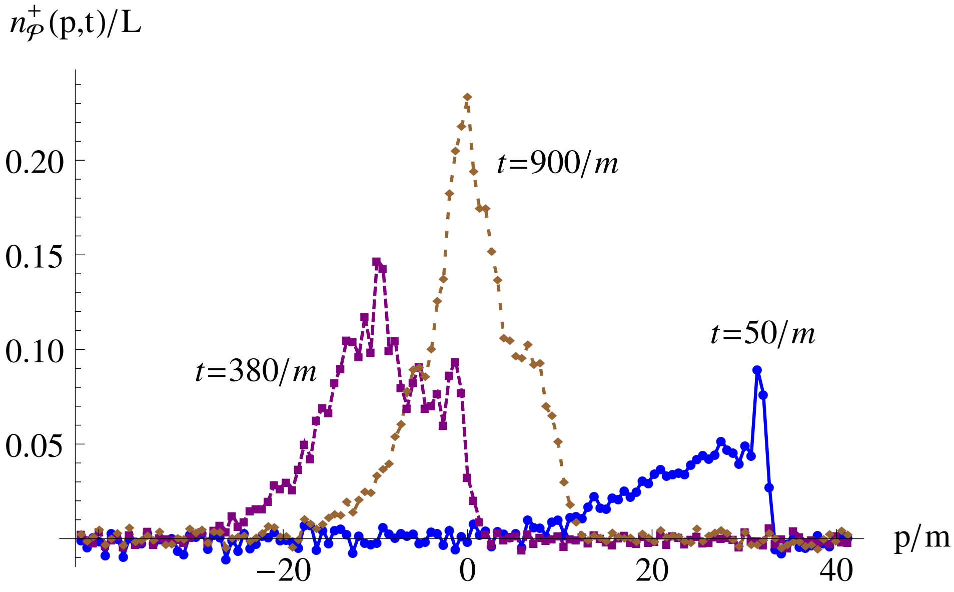

Figure 6.8.: Normalized particle number marginal distribution $n^+_{\mathcal{P}}(p,t)/L$ for simulations with backreaction at different times for an initial value $\epsilon = 1$. The parameters are $N_{\text{sto}} = 10^4$, $a_t = 0.0025/m$, $a_s = 0.075/m$, $N = 512$ such that $L = 38.4/m$.

excitations are created in a space region where the electric field acts. The creation process also comes with a polarization effect, separating positive from negative charges. It has to be emphasized, however, that $n^+_{\mathcal{X}}(x,t)$ and $n^-_{\mathcal{X}}(x,t)$ still overlap at these early times.

This changes in the propagation regime: Owing to the acceleration by the electric field, one bunch of excitations with positive charge propagates into the positive x-direction whereas another bunch of excitations with negative charge propagates into the opposite direction. Asymptotically, these bunches can be identified with particles and antiparticles, respectively.

In Fig. 6.10 we show the total number of created particles $n^+(t)$ for $t \to \infty$ as a function of the spatial extent λ. The result without backreaction corresponds to the dashed line. One clearly observes the termination of the fermion–anti-fermion creation process for small values of λ: The pair creation process terminates if the work done by the electric field over its spatial extent is too small to provide the rest mass energy of the fermion–anti-fermion pair. This observation is in perfect agreement with previous studies [110, 119, 123, 124]. For large values of λ we find a linear growth of the particle number, which reflects the scaling of the available electric field energy that grows with λ.

Particle production with backreaction

We now consider the numerical solution of the full lattice problem including backreaction. The solid line in Fig. 6.10 shows the full result for the total number of created particles

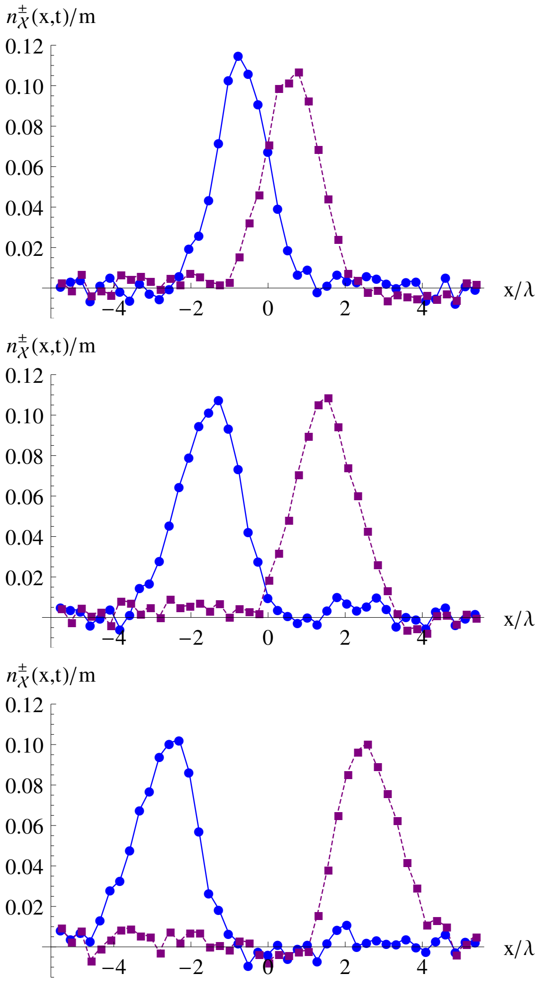

Figure 6.9.: Position space marginal distributions $n_\chi^-(x,t)$ (solid line) and $n_\chi^+(p,t)$ (dashed line) for $\epsilon = 1$ at different times $t = 0$ (top), $t = 0.6/\omega$ (middle) and $t = 1.2/\omega$ (bottom). The parameters are $N_{\text{sto}} = 10^5$, $a_t = 0.01/m$, $a_s = 0.22/m$, $N = 256$ such that $L = 56.32/m$.

$n^+(t \to \infty)$ as a function of the spatial extent λ. In accordance with the previous discussion we find that the backreaction mechanism tends to decrease the number of created particles since the electric field is weakened by the pair-production. For large enough spatial extent of the pulse, such that the pair-production is significant enough for backreaction to become important, this eventually decreases the slope of the curve growing linearly with λ for large spatial extent.

The dashed curve in the upper part of Fig. 6.11 shows the position-space marginal distribution $n_\chi^\pm(x,t)$ at time $t = 6/\omega$. At this time the duration of the initial electric

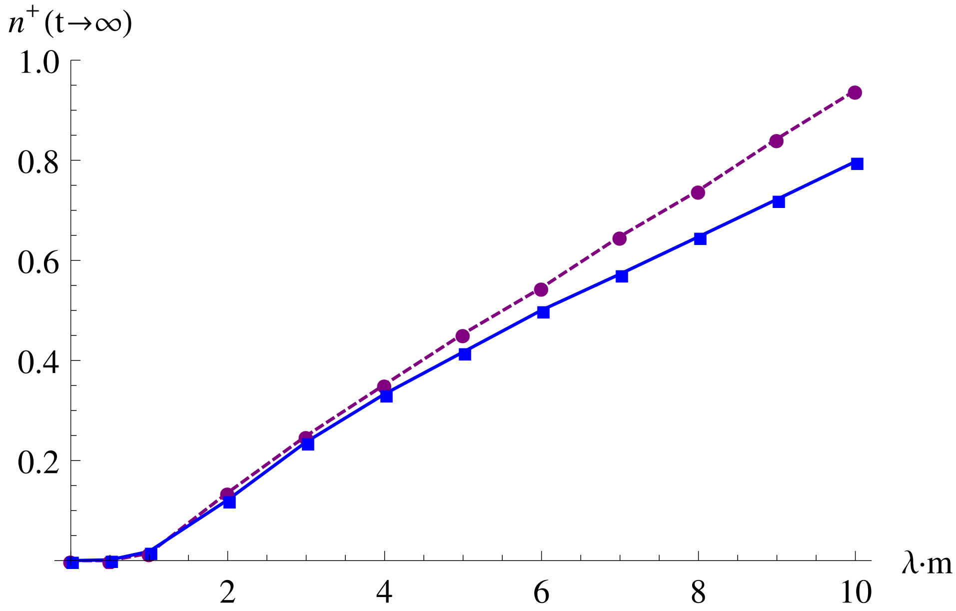

Figure 6.10.: Total number of created particles $n^+(t \to \infty)$ for $\epsilon = 1$ as function of the spatial extent λ of the pulse. Compared are the full result (solid line) and the result without backreaction (dashed line). The parameters are $N_{\text{sto}} = 10^5$, $a_t = 0.00125/m$, $a_s = 0.22/m$, $N = 512$ such that $L = 112.64/m$.

field pulse and the corresponding pair creation regime is long over. The electric field parameters are $\epsilon = 1$, $\omega = 0.2m$ and $\lambda = 5/m$.

The acceleration by the electric field leads to one bunch of excitations with positive charge propagating into the positive x-direction whereas another bunch of excitations with negative charge is propagating into the opposite direction. Most strikingly, we find that a self-consistent electric field $E(x,t)$ between the two fermion bunches builds up in the absence of any external field (6.63) at these times. The two bunches consisting of particles and anti-particles act as a capacitor [125], creating a homogeneous electric field between them whereas there is no field outside them. This electric field is shown in the lower part of Fig. 6.11. Owing to the description of the fermionic degrees of freedom in terms of low-cost fermions, we observe some small fluctuations in the electric field on top of this homogeneous field. Again, these fluctuations decrease with increasing N_{sto}.

The homogeneous electric field between the fermion bunches can be represented in terms of a linear rising potential. For larger values of the initial field strength E_0 or the coupling e, we expect that secondary particle creation due to the self-consistent electric field takes place. This mechanism would result in the depletion of the electric field reminiscent to the effect of string-breaking. This will involve further studies with supercritical initial field strengths which is beyond the scope of the present work and deferred to a future publication.

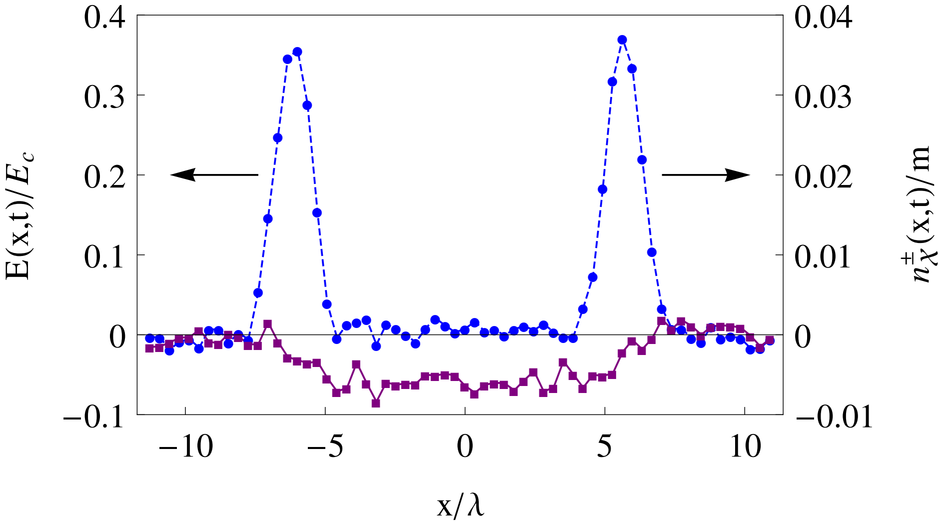

Figure 6.11.: Self-consistent electric field $E(x,t)$ (solid line) and position space marginal distributions $n^{\pm}_{\chi}(x,t)$ (dashed line) at $t = 6/\omega$ for $\epsilon = 1$, $\omega = 0.2m$ and $\lambda = 5/m$. The arrows indicate the propagation direction of the particle and anti-particle bunch, respectively. The parameters are $N_{\text{sto}} = 10^6$, $a_t = 0.0075/m$, $a_s = 0.22/m$, $N = 512$ such that $L = 112.64/m$.

6.1.3. Conclusions

We investigated fermion–anti-fermion pair production in 1 + 1 dimensions based on real-time lattice simulations. To this end, we discussed the lattice equations of motion using the low-cost fermion algorithm to solve them. In order to define gauge-invariant fermionic distributions corresponding to charge, energy or particle/anti-particle number, we derived the lattice analogue of the continuum Dirac-Heisenberg-Wigner function. In the continuum formulation, gauge invariance of these distributions is achieved by a Wilson line along the straight line. On the lattice, however, the straight line path is not unique due the periodicity of the lattice. We showed that correspondence with established results is achieved by replacing the straight path in the continuum by the shortest path on the lattice.

Investigating the field-strength dependence of the fermion–anti-fermion production rate in a static background field we accurately reproduced the Schwinger formula. We then discussed the decay of the field due to the backreaction of the created fermion–anti-fermion pairs. For the case of inhomogeneous gauge fields we computed for the first time the full problem taking backreaction into account. Most notably, we could show that the two bunches consisting of particles and anti-particles create a homogeneous electric field between them whereas there is no field outside them. In subsequent work we will extend these studies to supercritical initial field strengths, which is expected to lead to striking pair creation phenomena reminiscent of string breaking.

It should be emphasized that the real-time lattice simulations are considerably cheaper from a computational point of view than continuum approaches such as based on the Dirac-Heisenberg-Wigner function. In view of potential experimental applications it is crucial that strongly inhomogeneous configurations can be well described. Strong inhomogeneities are a challenge for alternative approaches based on derivative expansions underlying effective kinetic descriptions. Here the lattice approach, which is based on ensemble techniques using inhomogeneous configurations, is particularly powerful.

We employed a low-cost fermion algorithm in our 1 + 1 dimensional simulations even though a mode-function expansion of the spinors would have been the more direct way. One reason for our choice was that we are aiming at investigations of QED and QCD in 3 + 1 dimensions since then the application of the mode function expansion becomes impracticable. Possible investigations of QED in 3 + 1 dimensions will show several major differences compared to the massive Schwinger model. Most notably, the gauge degrees of freedom are dynamical in contrast to 1 + 1 dimensions where the dynamics of the electric field is governed only by the fermionic backreaction.

6.2. Dynamics of string breaking

In this section we present a detailed *space-time picture of string breaking* in QED in one spatial dimension. This is possible since in this case the quantum dynamics of string breaking can be accurately mapped onto a classical problem, which can be rigorously solved on a computer using lattice gauge theory techniques [22, 7, 94].

For the case of two external static charges we establish a *two-stage process*: Exceeding a critical distance between the external charges quickly leads to spontaneous creation of fermion–antifermion pairs. However, the dynamical charges are produced on top of each other and, therefore, initially do not screen the external charges. We find that it takes a much longer time to separate the dynamical charges such that the string can finally break.

Strikingly, it turns out that most of the energy content of the string goes into the work that is required for the process of charge separation, and only a small fraction is spent on pair creation. This has a significant impact on the estimate of the critical charge separation for string breaking, and we give a simple model that explains our simulation results. We then exploit the rich phenomenology that becomes accessible in a real-time treatment of string formation and subsequent breaking. For this purpose, we discard external charges and consider the physical situation of dynamical charges only. This allows us to establish the phenomenon of multiple string breaking from dynamical charges flying apart.

6.2.1. Two stages of string breaking

The vacuum of QED is unstable against the formation of many-body states in the presence of strong electric fields. The creation of electron-positron pairs in a uniform electric field may be viewed as a quantum process in which virtual electron-positron dipoles can be separated to become real pairs once they gain the binding energy of twice the rest mass, $2m$, where we use the convention with a speed of light equal to one. This Schwinger process is exponentially suppressed unless a critical field strength determined by the electron mass m and the electric charge e is reached [68, 69, 70]:

$$E_{\mathrm{c}} = \frac{m^2}{e} \,. \tag{6.64}$$

For a confining string connecting two external static charges, the energy content of the string rises linearly with the distance between the charges. For the case of QED in one spatial dimension with N_0 external charges $\pm eN_0$ that are separated by a distance d, Gauss' law $\partial_x E = eN_0\,[\delta(x+d/2) - \delta(x-d/2)]$ results in a homogeneous electric field $E_{\mathrm{str}} = eN_0$ between the two charges. Accordingly, the potential energy rises linearly with the separation d:

$$V_{\mathrm{str}} = \frac{1}{2}\int_{-d/2}^{d/2} dx\, E_{\mathrm{str}}^2 = \frac{e^2 N_0^2 d}{2} \,. \tag{6.65}$$

In the absence of dynamical fermions, this equation holds for arbitrary separations d. However, in the interacting theory fermion–antifermion pairs will be created spontaneously once the energy content of the string becomes large enough for distances exceeding a critical distance $d_{\mathbf{c}}$. As a dynamical process, string breaking can be defined to happen at the time when the total screening of the external charges by the dynamically created pairs occurs such that the corresponding electric field vanishes. For this it is necessary to produce at least N_0 fermion–antifermion pairs. Due to the exponential suppression of the Schwinger mechanism, this is expected to occur efficiently only for $E_{\mathrm{str}} \gtrsim m^2/e$ according to (6.64). Therefore, we consider $e/m = 1/\sqrt{N_0}$ in the following such that $E_{\mathrm{str}} = E_{\mathrm{c}}$. Below we will discuss also more general sets of parameters in the context of multiple string breaking.

We compute this process from first principles using real-time simulation techniques for lattice QED with Wilson fermions following Refs. [22, 7, 94]. In this nonperturbative approach the full quantum dynamics of fermions is included while the gauge field dynamics is accurately represented by classical simulations for relevant field strengths. The real-time simulations are performed on a spatial lattice with the number of sites ranging from 1024 up to 4096 and lattice spacings between $a_s = 0.05/m$ and $0.1/m$, with temporal steps $a_t/a_s = 0.0125 - 0.04$. We carefully checked the insensitivity of our results to volume and lattice spacing variations. Observables such as the charge density $\rho(x,t)$ or the fermion density $n(x,t)$ are calculated from gauge-invariant correlation functions in a standard way [94]. Here the fermion density $n(x,t)$ is related to the fermion energy density so that fermions and antifermions contribute with the same sign. As these observables are defined from the quantum expectation value of correlation functions, quantities like the average number of fermion–antifermion pairs $N(t) = \int dx\, n(x,t)/2$ can take on non-integer values. First, we consider the case $N_0 = 1$ such that $e/m = 1$. In Fig. 6.12 the space-time evolution of the fermion density $n(x,t)$ is shown for two external static charges $\pm e$ separated by $d = 28/m$, along with the electric field $E(t)$ at $x = 0$ as well as the average number of pairs $N(t)$ as a function of time. From the simulations we find that the employed separation of external charges just lies above the required critical distance $d_{\mathbf{c}}$ for string breaking. At early times, the fermion density $n(x,t)$ between the external charges increases due to the Schwinger mechanism on rather short time scales of $t_{\text{prod}} \simeq 1/m$. At the same time, we find that the charge density still vanishes, $\rho(x,t) = 0$: Fermions and antifermions are initially produced on top of each other and, accordingly, the dynamically created charges do not screen the electric field E_{str} yet. After the first stage, fermion–antifermion production has ceased and the average number of pairs $N(t_{\text{prod}}) \simeq N_0$ stays practically constant. At the same time, the remaining electric field separates the dynamically created charges, which is a much longer lasting process with a separation time $t_{\text{sep}} \simeq 20/m$. Due to the continuous separation process, the external charges are gradually screened so that $E(t) \to 0$ in the end. This screening process shows a linear behavior in time since the dynamically created charges move apart from each other close to the forward light cone. Remarkably, only a rather small fraction of the initial electric field energy is expended on the rest mass energy, $V_{\text{str}} > 2m$, whereas the largest fraction is used for separating the charges.

We have also simulated the system in the weak coupling regime $e/m = 1/\sqrt{N_0}$ with $N_0 = 2, 3, 4, 5$ such that still $E_{\text{str}} = E_{\text{c}}$. The picture of a two-stage process is seen also in these cases with the critical distance showing the dependence $d_{\mathbf{c}} \simeq 26/e = 26\sqrt{N_0}/m$.

We now give a simple dynamical picture providing, in particular, semi-quantitative estimates for $d_{\mathbf{c}}$ as well as the charge separation work W. To describe the fermion–antifermion production, we employ a model which is based on the Schwinger formula in one spatial dimension, which is typically applicable even for slowly varying electric fields:

$$\dot{N}(t) = d\frac{eE(t)}{2\pi}\exp\left(-\frac{\pi m^2}{eE(t)}\right), \tag{6.66}$$

with $N(0) = 0$. For $t \lesssim t_{\text{prod}} \ll d$, the electric field $E(t)$ decreases with time due to the production of fermion–antifermion pairs as well as the gradual screening of the external charges. In this regime, the field can be approximately described by

$$E(t) \simeq \sqrt{e^2 N_0^2 - \frac{4mN(t)}{d}} - \frac{eN(t)}{d}t\,. \tag{6.67}$$

Solving the differential equation (6.66) with (6.67), such that $N(t_{\text{prod}}) \to N_0$, results in a numerical estimate for the critical distance $d_{\mathbf{c}} \simeq 28.5/e = 28.5\sqrt{N_0}/m$, which is in good agreement with the values we find in our real-time lattice simulations.

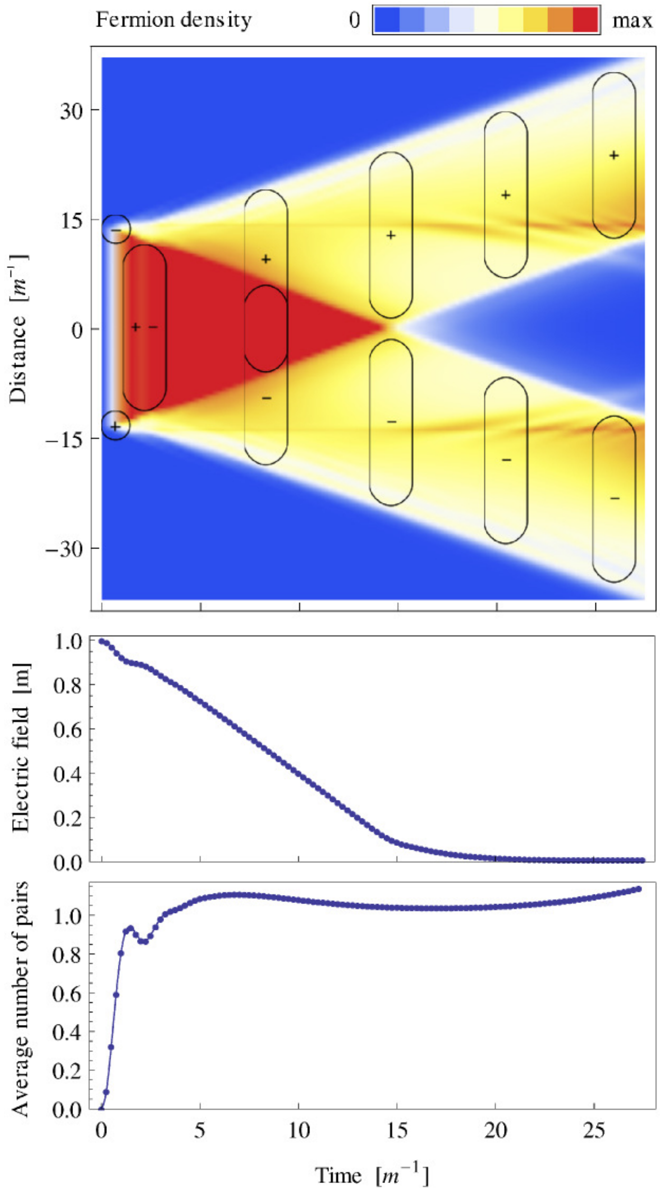

Figure 6.12.: Space-time evolution of string breaking for external static charges ±e (denoted by $\ominus$ and $\oplus$) with $e/m = 1$ separated by $d = 28/m$. **Top:** Fermion density $n(x,t)$. The vertical ovals represent the charge density $\rho(x,t)$ according to our model (6.68) for charge separation. The charge density vanishes in regions where positively and negatively charged ovals overlap. **Middle:** Time-dependence of the electric field $E(t)$ at $x = 0$. **Bottom:** Average number of fermion–antifermion pairs $N(t)$.

Moreover, we give an estimate of the charge separation work W which is based on the simple model that two homogeneous regions of positive and negative charge density are produced on top of each other at some time $t = 0$. These charges are then accelerated by the electric field and move apart from each other close to the forward light cone:

$$\rho^{\pm}(x,t) = \pm\frac{eN_0}{d_\mathbf{c}}\left[\Theta\left(x \mp t + \frac{d_\mathbf{c}}{2}\right) - \Theta\left(x \mp t - \frac{d_\mathbf{c}}{2}\right)\right], \tag{6.68}$$

with the average charge $\int dx\rho^{\pm}(x,t) = \pm eN_0$ and $\Theta(x) = 1$ for $x > 0$ while being zero otherwise. For this model, by applying Gauss' law, the electric field $E(x,t)$ is obtained analytically. The work done by the electric field on the positive and negative charges upon separating them over a distance $d_\mathbf{c}/2$, such that the electric field is completely screened at $x = 0$, is then given by

$$W^{\pm} = \pm\frac{eN_0}{d_\mathbf{c}}\int_{-d_\mathbf{c}/2}^{d_\mathbf{c}/2} dx_i \int_{x_i}^{x_i \pm d_\mathbf{c}/2} dxE(x,t) = \frac{5e^2N_0^2d_\mathbf{c}}{24}\,, \tag{6.69}$$

where the integral is over the time-dependent paths $x(t) = x_i + t$. Plugging $d_\mathbf{c}$ into the expression for the work (6.69) one obtains:

$$W = W^{+} + W^{-} = \frac{5e^2N_0^2d_\mathbf{c}}{12} \simeq 12mN_0^{3/2}\,. \tag{6.70}$$

This confirms our findings that the total work for charge separation well exceeds the rest mass energy $2mN_0$.

The two-stage process of fermion–antifermion production and charge separation describes the early-time behavior of the system well. At later times, however, the picture becomes more involved due to the dynamics of the created fermion–antifermion pairs coupled to the electric field. Here, we want to mention two effects which can be observed at later times: screening of external charges and propagating charge-neutral states.

In Fig. 6.13 the charge density $\rho(x, t = 100/m)$ is shown at late times for $N_0 = 1$ separated by $d = 10/m$ in the strong-coupling regime with $e/m = 2$, such that $E_{\text{str}} = 4E_\text{c}$. At early times, we again observe the two-stage process of pair production and charge separation. However, due to the particular choice of d and E_{str} there are more than one but rather $N(t_{\text{prod}}) \simeq 5$ fermion–antifermion pairs produced. Accordingly, only one fermion and antifermion are subsequently used to screen the external charges $\pm e$. For this configuration we find for its spread $\simeq 3/m$. This behavior resembles the screening of external charges in the Schwinger model, corresponding to the limit $e/m \to \infty$ [126]. The remaining $4N(t)/5 \simeq 4$ fermion–antifermion pairs, however, bunch to composite charge-neutral states which propagate freely since the external charges are totally screened. A detailed description of this effect is deferred to a future investigation.

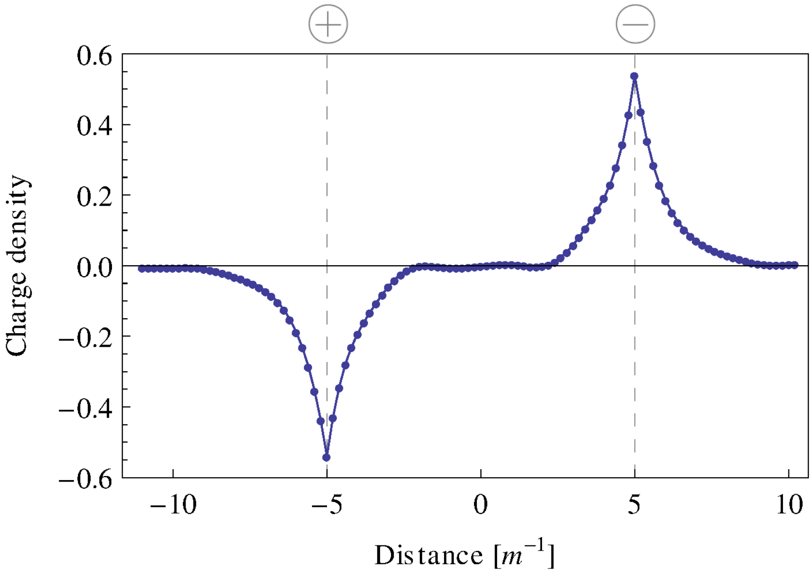

Figure 6.13.: Screening of external charges. The charge density $\rho(x, t = 100/m)$ is shown for external static charges $\pm e$ (denoted by $\ominus$ and $\oplus$) separated by $d = 10/m$ for $e/m = 2$.

6.2.2. Multiple string breaking

So far we considered string breaking for two external static charges. We now generalize the above setup by simulating two oppositely charged bunches of dynamical fermions moving apart from each other, i. e. we no longer include external static charges. These bunches can be either produced by an external field pulse, or, more directly, one can initialize the fermion fields according to a given distribution [119]. Here we employ Gaussian distributions around $x = 0$ with a width of $\sigma_x = 5/m$ in real-space and $\sigma_p = 4.6m$ in momentum-space. We initialize two fermion bunches with relativistic momenta in opposite direction with an initial number of pairs $N(0) = 24$ and given coupling $e/m = 0.35$.

In order to visualize the time evolution, we display in Fig. 6.14 the electric field $E(x, t)$ (upper left panel) and its value at $x = 0$ (lower left panel). Moreover, we also show the charge density $\rho(x, t)$ (upper right panel) and the average number of pairs $N(t)$ (lower right panel). Due to the initial relativistic momenta of the fermions and antifermions, they move apart from each other with a velocity close to the speed of light. In the current configuration, fermions with negative/positive charge move into the positive/negative x–direction. Upon separating from each other, an electric field string is formed between them.

For the chosen initial conditions the maximum achieved field strength is much larger than E_c. The time at which this maximum is reached is indicated by the first dashed line

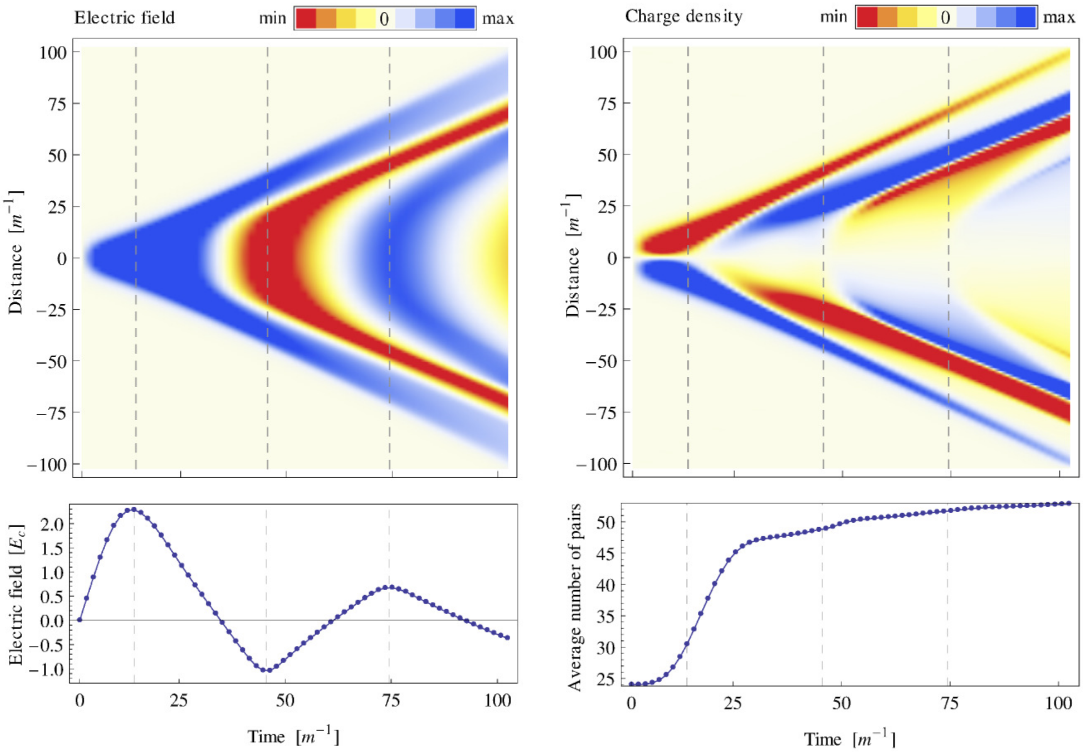

Figure 6.14.: Space-time evolution of multiple string breaking from dynamical charges flying apart. **Top left:** Electric field $E(x,t)$. **Bottom left:** Central electric field $E(0,t)$ in units of E_c. The dashed lines indicate the times at which $E(0,t)$ is extremal. **Top right:** Charge density $\rho(x,t)$. **Bottom right:** Average number of fermion–antifermion pairs $N(t)$. The dashed lines indicate the times at which $E(0,t)$ becomes extremal.

in Fig. 6.14. Around this time, efficient fermion production sets in such that the average number of pairs $N(t)$ rises significantly. In complete analogy to the above discussion, the newly created charges still sit on top of each other such that the electric field is not screened yet.

In order to screen the initial bunches, the newly created charges need to be separated. As a consequence, the electric field performs work and drops linearly with time and finally even changes sign. At that time, two new bunches of fermions have formed which are oppositely charged compared to the initial ones, and again move apart from each other (*primary string breaking*). This results in a secondary electric string with a maximum field strength of the order of $-E_c$, indicated by the second dashed line. As a consequence, fermion production sets in again, however, less efficient than before because of the lower maximum field strength. Charges are again created on top of each other and are subsequently separated, resulting in a rise of the electric field including a sign change. As a consequence, the formation of two new fermion bunches can be observed, again oppositely charged compared to the previous ones (*secondary string breaking*). The following extremum of the electric field, as indicated by the third dashed line in the corresponding figures, is already below the critical field strength such that fermion production effectively stops and the average number of pairs becomes asymptotically constant.

6.2.3. Conclusions

To conclude, our results provide unprecedented insights into the real-time dynamics of string formation and breaking from first principles. The described phenomenon of string breaking in QED is intimately related to a one-dimensional geometry, which poses strong constraints on possible experimental realizations. However, ultracold atoms in an optical lattice could provide a perfect laboratory for this type of physics, in particular, since they are very suitable to access low-dimensional geometries. For the specific case of QED in one spatial dimension, one can use angular momentum conserving atomic scattering processes to directly implement the $U(1)$ gauge symmetry without the need to construct low-energy effective theories [33]. In this context, our calculation serves as an important validator for quantum simulators using cold atoms.

6.3. Quark production and gluon dynamics in QCD

In this section we will explore how quarks are produced in QCD starting from initial conditions relevant for the early pre-equilibrium phases of heavy-ion collisions. Earlier studies of purely gluonic dynamics in heavy-ion collisions have established a turbulent regime with an energy cascade towards the ultraviolet. The purposes of our investigations are to determine the overall scale of quark production and to get an insight into spectral properties of non-equilibrium fermionic distributions. Special emphasis will be placed on the role of bosonic turbulence for their late time behaviour. Furthermore, we are interested in a comparison between different initial scenarios concerning their impact on the quark sector.

6.3.1. QCD on a real-time lattice

To study real-time dynamics of QCD in 3 + 1 dimensions, we apply methods of lattice gauge theory similar to those introduced for 1 + 1 dimensional QED in Sec. 6.1. In lattice gauge theory, the action is formulated in terms of so-called unitary link variables $U_\mu(x)$ instead of the original gauge fields $A_\mu^a(x)$. The connection between these formulations is straight forward:

$$U_\mu(x) = e^{iga_\mu A_\mu(x)} = e^{iga_\mu A^b_\mu(x)\sigma^b}\,. \tag{6.71}$$

Here a_μ is the lattice spacing in spatial or temporal direction (no summation over μ is implied), g is the gauge coupling and σ^b are the $N_c^2 - 1$ generators of the relevant gauge group $SU(N_c)$. We will restrict ourselves to the $SU(2)$ gauge group where the traceless and Hermitian generators are proportional to the standard Pauli matrices τ_a

$$\sigma_a = \frac{\tau_a}{2}\,, \tag{6.72}$$

with

$$\tau_1 = \begin{pmatrix} 0 & 1 \\ 1 & 0 \end{pmatrix}, \quad \tau_2 = \begin{pmatrix} 0 & -i \\ i & 0 \end{pmatrix}, \quad \tau_3 = \begin{pmatrix} 1 & 0 \\ 0 & -1 \end{pmatrix}. \tag{6.73}$$

Since our goal is to formulate the QCD action in terms of local gauge-invariant quantities, we construct closed loops from neighbouring link variables, the so-called plaquettes

$$U_{\mu\nu}(x) = U_\mu(x) U_\nu(x+\hat{\mu}) U^\dagger_\mu(x+\hat{\nu}) U^\dagger_\nu(x)\,. \tag{6.74}$$

The notation $\hat{\mu}$ used here implies moving to the next lattice point in μ direction. These objects contain information about the field-strength tensor $F_{\mu\nu} = F^a_{\mu\nu}\sigma^a$. Its components can be extracted to the leading order in lattice spacings via

$$F^a_{\mu\nu}(x) = \frac{-2i}{ga_\mu a_\nu}\mathrm{Tr}\left[\sigma^a U_{\mu\nu}(x)\right]. \tag{6.75}$$

Particularly important are the local chromoelectric and chromomagnetic fields, $E_j(x)$ and $B_j(x)$:

$$E^a_j(x) = \frac{-2i}{ga_t a_s}\mathrm{Tr}\left[\sigma^a U_{0j}(x)\right] \tag{6.76}$$

$$B^a_j(x) = \frac{i}{ga_s^2}\epsilon_{jkl}\mathrm{Tr}\left[\sigma^a U_{kl}(x)\right]. \tag{6.77}$$

Now we have all of the ingredients for the gluonic part of the lattice action, $S_g[U]$:

$$S_g[U] = \frac{4}{g^2}\sum_x \left\{ \frac{a_s}{a_t}\sum_j \left[1 - \frac{1}{2}\mathrm{Tr}U_{0j}(x)\right] - \frac{a_t}{a_s}\sum_{j<k}\left[1 - \frac{1}{2}\mathrm{Tr}U_{jk}(x)\right] \right\}, \tag{6.78}$$

where we sum over all lattice points x and the three spatial directions j. The above expression is nothing else but the lattice version of the standard gauge action $S_{gauge} = \frac{1}{2}\int_x (E^2(x) - B^2(x))$. In the total action for our two-colour version of QCD, $S[U, \bar{\psi}, \psi] =$

$S_g[U] + S^0_\psi[U, \bar\psi, \psi] + S^W_\psi[U, \bar\psi, \psi]$, the quark contribution consists of the standard fermionic term with a gauged central derivative $S^0_\psi[U, \bar\psi, \psi]$ and a pseudoscalar Wilson term $S^W_\psi[U, \bar\psi, \psi]$, similar to the one employed in Chap. 5:

$$S^0_\psi[U, \bar\psi, \psi] = a_t a_s^3 \sum_{x,\mu} \bar\psi(x) \left(i\gamma^\mu \frac{U_\mu(x)\psi(x+\hat\mu) - U^\dagger_\mu(x-\hat\mu)\psi(x-\hat\mu)}{2a_\mu} - m\psi(x) \right) \tag{6.79}$$

$$S^W_\psi[U, \bar\psi, \psi] = a_t a_s^3 \sum_{x,j} \bar\psi(x) \left(i\gamma^5 \frac{U_j(x)\psi(x+\hat j) + U^\dagger_j(x-\hat j)\psi(x-\hat j) - 2\psi(x)}{2a_s} \right) \tag{6.80}$$

Mind that also the derivatives in the Wilson term have been consistently gauged with gluonic link variables. For the time evolution we take advantage of the gauge freedom and apply the temporal axial gauge, meaning that $A_0 = 0$ and correspondingly $U_0 = \mathbb{I}$. But before making such simplification we derive the equations of motion for our theory. We do it by variation of the action w.r.t. the fermion fields and the link variables. The discretized fermionic equation of motion is given by

$$\begin{aligned} \psi(x+\hat t) = \psi(x-\hat t) &- 2ia_t m\gamma^0\psi(x) - \frac{a_t}{a_s}\gamma^0 \sum_j \gamma^j \left[U_j(x)\psi(x+\hat j) - U^\dagger_j(x-\hat j)\psi(x-\hat j)\right] \\ &- \frac{a_t}{a_s}\gamma^0\gamma^5 \sum_j \left[U_j(x)\psi(x+\hat j) + U^\dagger_j(x-\hat j)\psi(x-\hat j) - 2\psi(x)\right] . \end{aligned} \tag{6.81}$$

This equation will govern the time evolution of stochastic spinor fields in the framework of male/female method, as described in Sec. 4.2. Variation of the action w.r.t. the spatial links leads to a dynamical equation for the chromoelectric field

$$\begin{aligned} E^a_j(x) = E^a_j(x-\hat t) &+ \frac{2ia_t}{ga_s^3} \sum_{k\neq j} \Big[\mathrm{Tr}(\sigma^a U_j(x) U_k(x+\hat j) U^\dagger_j(x+\hat k) U^\dagger_k(x)) \\ &+ \mathrm{Tr}(\sigma^a U_j(x) U^\dagger_k(x+\hat j-\hat k) U^\dagger_j(x-\hat k) U_k(x-\hat k))\Big] \\ &+ \frac{ga_t}{4} \sum_j \Big[\langle\bar\psi(x)\gamma^j\sigma^a U_j(x)\psi(x+\hat j)\rangle_{\mathrm{sto}} + \langle\bar\psi(x+\hat j)\gamma^j U^\dagger_j(x)\sigma^a\psi(x)\rangle_{\mathrm{sto}} \\ &+ \langle\bar\psi(x)\gamma^5\sigma^a U_j(x)\psi(x+\hat j)\rangle_{\mathrm{sto}} - \langle\bar\psi(x+\hat j)\gamma^5 U^\dagger_j(x)\sigma^a\psi(x)\rangle_{\mathrm{sto}}\Big] . \end{aligned} \tag{6.82}$$

Here we already included the stochastic average over an ensemble of male/female pairs for the backreaction of fermions onto gauge fields. Similarly, a variation w.r.t. temporal links produces the so-called Gauss constraint:

$$\tfrac{a_s^2}{g} \quad \sum_j \left[E^a_j(x) + \frac{2i}{ga_t a_s}\mathrm{Tr}(\sigma^a U^\dagger_j(x-\hat j) U_{0j}(x-\hat j) U_j(x-\hat j))\right] + \tag{6.83}$$

$$\tfrac{a_s^3}{4} \quad \left[\langle\bar\psi(x)\gamma^0\sigma^a\psi(x+\hat t)\rangle_{\mathrm{sto}} + \langle\bar\psi(x+\hat t)\gamma^0\sigma^a\psi(x)\rangle_{\mathrm{sto}}\right] = 0 . \tag{6.84}$$

As long as this constraint is fulfilled by initial conditions it remains conserved by the time evolution, up to numerical rounding errors. In our simulations with male/female fermions, we fix the Gauss law numerically with an iterative method and monitor its violation during runtime. Having derived equations of motion for chromoelectric fields and quarks, we need to find an equation for the spatial link variables $U_j(x)$ in order to complete the set of equations of motion for our system. To achieve this we reverse Eq. (6.76) and construct the temporal plaquette $U_{0j}(x)$ from $E_j^a(x)$. In this and all other situations in which a $SU(2)$ object is constructed, we take advantage of an exact formula for this gauge group:

$$U = \cos\left(\frac{\sqrt{c_a c^a}}{2}\right)\mathbb{I} + \frac{2i}{\sqrt{c_a c^a}}\sin\left(\frac{\sqrt{c_a c^a}}{2}\right)c_a\sigma^a\,, \tag{6.85}$$

with c_a being the coefficients for all $N_c^2 - 1$ gluon components. In temporal axial gauge $U_{0j}(x)$ can be used to determine the spatial link $U_j(x)$ at the next timestep

$$U_j(x+\hat{t}) = U_{0j}(x)U_j(x)\,, \tag{6.86}$$

so that we have a closed system of equations for link variables and chromoelectric fields acting as their conjugate momenta. To calculate bosonic expectation values in this framework, we apply classical-statistical sampling as described in 2.1.2. In order to define physically relevant particle numbers we will have to perform gauge transformations of the lattice fields. Local gauge transformations of link variables are defined by

$$U'_\mu(x) = G(x)U_\mu(x)G^\dagger(x+\hat{\mu})\,, \tag{6.87}$$

where $G(x)$ is a $SU(2)$ transformation matrix. Fermions are transformed by a group rotation with $G(x)$:

$$\psi'(x) = G(x)\psi(x)\,. \tag{6.88}$$

Initial conditions and particle numbers

We perform simulations of quark production starting from three distinct initial scenarios. The common property of all of them is the absence of any quarks in the initial state. We also assume the perturbative quark vacuum to be diagonal in colour and flavour. Another similarity is that we explicitly take initial conditions which guarantee large field amplitudes or large fluctuations of the gluon fields, a necessity dictated by our use of classical-statistical aproximation for bosonic dynamics.

The quantities which define a Gaussian initial condition in the gluonic sector are chromomagnetic and chromoelectric one-point functions, $\langle B_j^a(\mathbf{x},t_0)\rangle$ and $\langle E_j^a(\mathbf{x},t_0)\rangle$, as well as their two-point correlators $\langle B_j^a(\mathbf{x},t_0)B_k^c(\mathbf{y},t_0)\rangle$ and $\langle E_j^a(\mathbf{x},t_0)E_k^c(\mathbf{y},t_0)\rangle$. Note that in temporal axial gauge the chromomagnetic fields are completely determined by the spatial gauge fields $A_j^a(\mathbf{x},t)$ via $B_j^a(\mathbf{x},t) = \nabla_{\mathbf{x}} \times A_j^a(\mathbf{x},t)$. We initialize the gauge field fluctuations such that they represent a gas of spatially transversal particles in Coulomb gauge, very similar to a non-interacting photon gas in QED with additional internal group indices. The form of the corresponding correlators is set by a proper choice of chromoelectric and gauge fields in spatial momentum space for homogeneous and isotropic gluonic fluctuations at initial time:

$$A^a_j(\mathbf{k}, t_0) = \sqrt{\frac{n^a_g(|\mathbf{k}|, t_0) + \frac{1}{2}}{|\mathbf{k}|}} \sum_{\lambda}^{1,2} \left[b^a_{\lambda,\mathbf{k}} \epsilon_{\lambda,j,\mathbf{k}} + b^{a,*}_{\lambda,-\mathbf{k}} \epsilon^*_{\lambda,j,-\mathbf{k}} \right] \tag{6.89}$$

$$E^a_j(\mathbf{k}, t_0) = i \sqrt{|\mathbf{k}| \left(n^a_g(|\mathbf{k}|, t_0) + \frac{1}{2} \right)} \sum_{\lambda}^{1,2} \left[b^a_{\lambda,\mathbf{k}} \epsilon_{\lambda,j,\mathbf{k}} - b^{a,*}_{\lambda,-\mathbf{k}} \epsilon^*_{\lambda,j,-\mathbf{k}} \right] . \tag{6.90}$$

Here λ is the polarization index and $\epsilon_{\lambda,j,\mathbf{k}}$ are the components of normalized polarization vectors orthogonal to the propagation momentum $\mathbf{k}$. We choose this vectors to be real valued and construct them numerically for each spatial momentum by first taking cross product of a random vector with the incoming momentum and then building a second cross product between the normalized resulting vector and the particle momentum. The complex stochastical random numbers $b^a_{\lambda,\mathbf{k}}$ are drawn in the same fashion as in 5.1.2 such that the only non-vanishing connected (denoted by $\langle ... \rangle_{\text{con}}$) correlators between $A^a_j(\mathbf{k}, t_0)$ and $E^a_j(\mathbf{k}, t_0)$ read

$$\langle A^a_j(\mathbf{p}, t_0) A^b_k(\mathbf{q}, t_0) \rangle_{\text{con}} = \frac{1}{|\mathbf{p}|} \left(n^a_g(|\mathbf{p}|, t_0) + \frac{1}{2} \right) \left(\delta_{jk} - \frac{p_j p_k}{|\mathbf{p}|^2} \right) \delta(\mathbf{p} + \mathbf{q}) \delta^{ab} \tag{6.91}$$

$$\langle E^a_j(\mathbf{p}, t_0) E^b_k(\mathbf{q}, t_0) \rangle_{\text{con}} = |\mathbf{p}| \left(n^a_g(|\mathbf{p}|, t_0) + \frac{1}{2} \right) \left(\delta_{jk} - \frac{p_j p_k}{|\mathbf{p}|^2} \right) \delta(\mathbf{p} + \mathbf{q}) \delta^{ab} . \tag{6.92}$$

The disconnected parts have been omitted here, but they are initialized as macroscopic classical fields in some of our scenarios. More precisely, we start our computations either from a saturated state of overpopulated gluons or from anisotropic classical fields undergoing a rapid decay due to instabilities and particle production. The overpopulation scenario is realized by an initial distribution for gluonic occupation numbers

$$n_g(|\mathbf{p}|, t_0) = \frac{1}{g^2} \Theta(|\mathbf{p}| - Q_s) , \tag{6.93}$$

where the Heavyside function ensures that gluons populate all infrared modes up to the saturation scale Q_s with a parametrically high occupancy of $1/g^2$. Because of the typical form of the initial spectrum we will refer to this scenario as "Fluctuation" IC (initial condition). Note that this gluon distribution is isotropic in momentum space and in all colour indices. The approach to thermal equilibrium from such kind of initial conditions is marked by the transport of energy and particles to short length scales and by an overall reduction in the total number of gluons. The latter assumption can be justified by a short parametric estimate valid in the limit of $g^2 \ll 1$. Simple integration over $n_g(|\mathbf{p}|, t_0)$ yields the total quasi-particle energy of the initial state, $\varepsilon \sim Q_s^4/g^2$ and the total particle number $N_g \sim Q_s^3/g^2$. Energy conservation determines the final temperature of the thermal gluon gas to be $T \sim Q_s/\sqrt{g}$, meaning that the number of particles in the thermal ensemble should be $N_g^{\text{th}} \sim T^3 \sim Q_s^3/g^{3/2}$. As a consequence we see that $N_g > N_g^{\text{th}}$ for small gauge couplings.

In the next section, the evolution of the overpopulated initial state will be compared to a system where overpopulation is dynamically generated by a Nielsen-Olesen magnetic plasma instability. This instability is triggered by an initial chromomagnetic field in longitudinal direction, $\langle B_i^a \rangle = \delta^{1a}\delta_{zi}B$, where B is the classical field strength. To realize such a configuration we initialize our simulations with macroscopic gauge fields

$$\langle A_x^2 \rangle = \langle A_y^3 \rangle = \sqrt{\frac{B}{g}}\,. \tag{6.94}$$

These initial fields cause the longitudinal field $B(t)$ to perform damped oscillations in time, with the damping being provided by interactions with exponentially growing gluon fluctuations. The momentum dependent growth rate of these fluctuations in the linear regime is $\gamma_p = \sqrt{g\bar{B} - p_z^2}$, with $\bar{B}$ being the time averaged absolute value of the chromomagnetic field[2]. In our figures this type of initial conditions is refered to as ”Condensate” IC (initial conditions).

In the color glass condensate description of the early phase of heavy-ion collisions [46] the initial coherent colour fields form so-called flux-tubes. These are regions of space in which both chromoelectric and chromomagnetic fields are aligned in the longitudinal direction. It turns out that a single flux-tube resembles the initial conditions for Nielsen-Olesen instabilities with an additional macroscopic field $\langle E_i^a \rangle = \delta^{1a}\delta_{zi}E$. This macroscopic chromoelectric field also exhibits damped plasma oscillations and simultaneously creates gluons and quarks via Schwinger mechanism. In a certain sense a flux-tube is a combination of Nielsen-Olesen instability with Schwinger effect in QCD. We will show in the following section how the longitudinal flux-tubes dissipate into fluctuations and discuss the emergent quark and gluon spectra.

To consider particle spectra in a theory with local gauge symmetry, we first need to define appropriate occupation numbers. Since our initial conditions are transversal in spatial momentum space, we choose to enforce this property also in the readout procedure. For this purpose we transform the gluonic and fermionic correlators by a unitary gauge transformation $G_t(x)$ onto a Coulomb-like spatially transversal gauge. In short, we impose

---

[2] As has been shown in [71], for these initial conditions the Nielsen-Olesen instability is accompanied by parametric resonance. But because the latter contributes much less to the total particle yield, we skip the discussion of its specifics and refer the reader to the original publication and our discussion of parametric resonance in 2.2.1.

two independent gauge conditions, $A_0 = 0$ and

$$\nabla_{\mathbf{x}} \cdot \mathbf{A}(\mathbf{x}, t) = 0\,. \tag{6.95}$$

These conditions eliminate two of the four gluonic degrees of freedom, so that we are left with only two transversal polarizations per gluon, in accordance with our initial fluctuations. However, in contrast to standard Coulomb gauge, our transformation is time dependent, since we need to calculate the transformation matrices every time when we measure particle spectra. Numerically it is done by a stochastic overrelaxation algorithm described in [127]. The transformation matrices $G_t(x)$ computed with this algorithm are then used to transform link variables, temporal plaquettes (which represent local chromoelectric fields) and male/female spinor fields

$$\begin{aligned} U_j^{\mathrm{CG}}(x) &= G_t(x) U_j(x) G_t^{\dagger}(x + \hat{j}) \qquad (6.96)\\ U_{0j}^{\mathrm{CG}}(x) &= G_t(x) U_{0j}(x) G_t^{\dagger}(x) \qquad (6.97)\\ \psi^{\mathrm{CG}}(x) &= G_t(x) \psi(x)\,. \qquad (6.98) \end{aligned}$$

The abbreviation CG stands here for Coulomb-like gauge. The definition of the fermionic occupation number is essentially identical to the one employed in Eq. (5.26), the only differences being the usage of gauge transformed correlators averaged over colour and flavour indices[3]. Gluonic particle numbers are defined as following

$$n_g(|\mathbf{p}|, t) = \frac{\sqrt{\mathrm{Tr}\left[\langle A_i^b(|\mathbf{p}|, t) A_j^c(| - \mathbf{p}|, t)\rangle_{\mathrm{CG}}\right] \mathrm{Tr}\left[\langle E_i^b(|\mathbf{p}|, t) E_j^c(-|\mathbf{p}|, t)\rangle_{\mathrm{CG}}\right]}}{(N_c^2 - 1)(d - 1)} - \frac{1}{2}\,. \tag{6.99}$$

The trace acts here in both colour and polarization space, the resulting particle number is an average over all internal degrees of freedom.

6.3.2. Isotropization and quark production

In the previous part we presented the types of initial conditions relevant for early-time dynamics in heavy-ion collisions that we decided to study using our lattice methods. A clear distinction between initial gluonic overpopulation and flux-tube or Nielsen-Olesen instabilities is the difference between isotropic and anisotropic states. Plasma instabilities and Schwinger pair production drive an initially highly anisotropic system towards isotropy and then further to thermal equilibrium, while the overpopulation scenario is isotropic from the very beginning. It is a priori not clear if any connection can be made between these very different scenarios and if each of them should be treated separately.

---

[3] So far we have not discussed different flavours in QCD, for our purposes the flavour is an internal degree of freedom. In this work we simulate two flavours of quarks with equal masses, which should represent the two light quarks in real QCD.

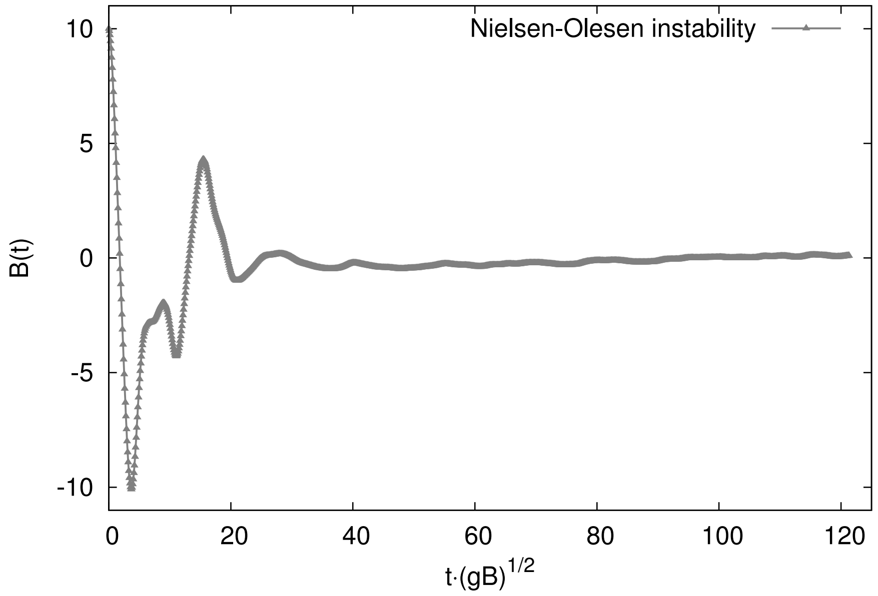

Figure 6.15.: Time evolution of the chromomagnetic field $B(t)$ during the Nielsen-Olesen instability.

To measure the evolution of the anisotropy with time we first present here results from Nielsen-Olesen and flux-tube simulations focusing on quantities which either determine the anisotropy of a system or are clear measures of it.

In the following we consider results for weakly coupled ($g^2 = 10^{-2}$), two colour QCD with two degenerate light quark flavours. The numerical results have been obtained on a 64^3 spatial lattice. Simulating at weak coupling guarantees that we are well inside the region of validity of classical-statistical approximation. Our main focus lies on gluon dynamics and its impact on quark production as well as on the properties of quark particle distributions. The backreaction of quarks onto the dynamics of gluons is parametrically $O(g^2)$ and is expected to become more important only at stronger couplings. We nevertheless include the backreaction for the reasons of consistency and have checked that the total energy is conserved during our simulations.

We begin our discussion with the time evolution of the chromomagnetic field $B(t)$. This field can be easily calculated from the rescaled macroscopic gauge field $\bar{A}(t)$ defined by inverting Eq. (6.94):

$$\bar{A}(t) = \frac{1}{2}\left(\langle A^2_x(t)\rangle + \langle A^3_y(t)\rangle\right) . \tag{6.100}$$

Initially $\bar{A}(t = 0) = \sqrt{B/g}$ according to 6.94. To get rid of the explicit coupling dependence we plot not $\bar{A}(t)$ but rather $B(t) = \sqrt{gB}\bar{A}(t)$. Note that B is an input parameter

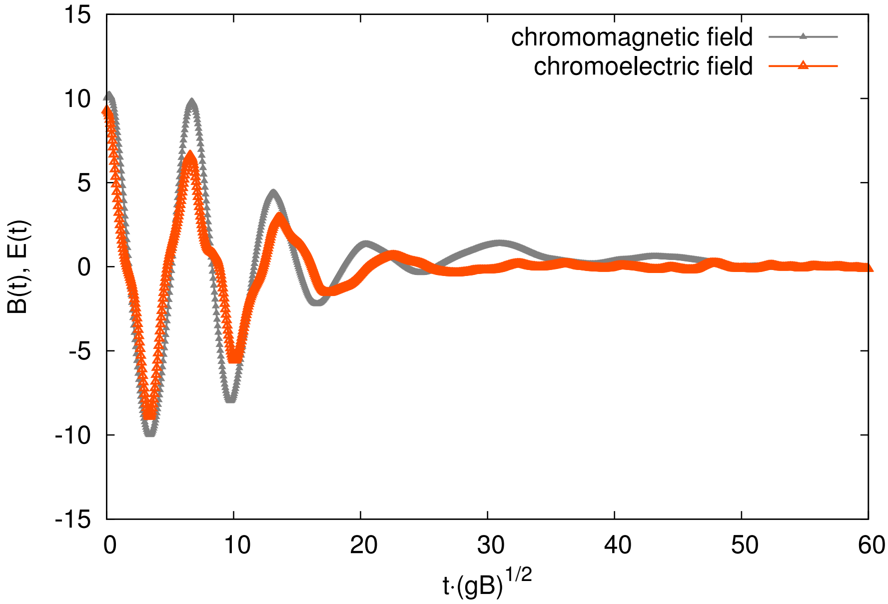

Figure 6.16.: Oscillations of longitudinal gauge fields in a flux-tube and their subsequent decay.

quantifying our energy density while $B(t)$ is a dynamically measured quantity. In Fig. 6.15 we see that the field, which starts at a high amplitude, exhibits damped oscillations and finally goes down to zero. At this point all of the energy originally contained in the one-point function has been transformed into higher correlation functions in the gluonic and fermionic sectors. This picture of initially oscillating but later vanishing macroscopic fields repeats itself in the simulations of a decaying flux-tube as presented in Fig. 6.16, where, additionally to the chromomagnetic field, a macroscopic chromoelectric field is initialized.

Here we plot the longitudinal chromoelectric field $\langle E_z^1 \rangle$ together with the chromomagnetic field $B(t)$. Both macroscopic fields undergo damped oscillations and are reduced by non-linear interactions and particle production. While the magnetic field destabilizes gauge fluctuations and causes exponentially rising solutions for infrared modes [71, 72], the electric component directly produces quarks and gluons [128] and accelerates them via the non-Abelian Lorentz force. For both scenarios we observe that the initial configuration dominated by the anisotropic fields is almost completely depleted after $t \simeq 50/\sqrt{gB}$. During the flux-tube decay (in Fig. 6.16), the chromoelectric field vanishes even earlier, around $t \simeq 30/\sqrt{gB}$, suggesting that the energy transfer from the electric sector to particles is more efficient. This observation may be interpreted analogous to the Lorentz force in classical electrodynamics, where electric fields are capable to change the absolute value of a point particle's momentum. Magnetic fields on the other hand only influence the direction of the total momentum.

A natural question arising from this observation is whether the anisotropy is maintained by two- and higher n-point correlators or whether the decay of either the flux-tube or the chromomagnetic field alone coincides with the isotropization of the system. To answer this question, we choose to measure the anisotropy as a function of time with gauge-invariant diagonal elements of the energy-momentum tensor. We define transversal and longitudinal pressure components on the lattice as

$$\begin{aligned}
\langle P_T\rangle(t) &= \frac{1}{N^3}\sum_x \Big[E^a_z(x)E^a_z(x) + B^a_z(x)B^a_z(x) \\
&\quad -\frac{i}{4a_s}\sum_j^{1,2}\langle\bar{\psi}(x)\gamma_j U_j(x)\psi(x+\hat{j})\rangle_{\text{sto}} - \langle\bar{\psi}(x)\gamma_j U_j^\dagger(x-\hat{j})\psi(x-\hat{j})\rangle_{\text{sto}}\Big] \\
\langle P_L\rangle(t) &= \frac{1}{N^3}\sum_x \Big[E^a_x(x)E^a_x(x) + B^a_x(x)B^a_x(x) + E^a_y(x)E^a_y(x) + B^a_y(x)B^a_y(x) \\
&\quad -\frac{i}{2a_s}\langle\bar{\psi}(x)\gamma_3 U_3(x)\psi(x+\hat{z})\rangle_{\text{sto}} - \langle\bar{\psi}(x)\gamma_3 U_3^\dagger(x-\hat{z})\psi(x-\hat{z})\rangle_{\text{sto}}\Big] .
\end{aligned} \tag{6.101}$$

Note that in thermal equilibrium pressure is an isotropic quantity related to the energy density by the equation of state, e.g. for a massless gas $\varepsilon = 3P$ where $P = P_L = P_T$. In Fig. 6.17 the ratio of longitudinal and transversal pressure components, P_L/P_T, is measured for different initial conditions as a function of time. At early stages of the time evolution this ratios are strongly oscillating but parallel to the vanishing of the macroscopic fields (in Figs. 6.15 and 6.16), the ratios reach the isotropic fixed point at $P_L/P_T = 1$. The isotropization proceeds faster in a decaying flux-tube, which we attribute to the more rapid decay of the longitudinal chromoelectric field. Our conclusion is that both flux-tube and Nielsen-Olesen initial conditions ultimately lead to isotropization on times scales easily accessible in lattice simulations.

This observation allows us to compare total particle yields and spectra obtained after plasma instabilities with those evolved from initial gluonic overpopulation, since in both cases we are dealing with largely isotropic states at later times. To make a proper comparison, we simulated both Nielsen-Olesen and overpopulation scenarios with an almost identical energy density, the same gauge coupling and same lattice parameters like the simulated volume, time discretization, lattice spacing etc. Instead of measuring bulk properties or homogeneous macroscopic fields, we are now interested in the details of particle distributions both for gluons and quarks. To get a better understanding of the dynamical changes in gluon distributions we present in Fig. 6.18 particle spectra at an early, intermediate and late time for Nielsen-Olesen and fluctuation dominated (overpopulation) initial conditions.

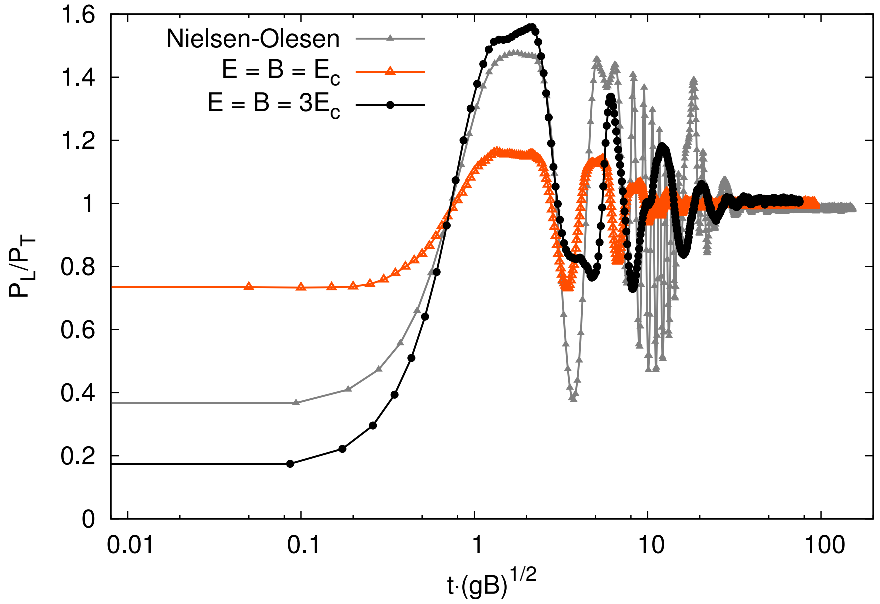

Figure 6.17.: Dynamics of pressure isotropization after Nielsen-Olesen instability and flux-tube decay.

At early times ($t = 3/Q_s$) the two spectra are clearly distinct. Nielsen-Olesen instability is unfolding, raising infrared occupancies at a considerably higher rate than in the ultraviolet. The original form of the fluctuation dominated initial condition with its ”knee” at $|\mathbf{p}| = Q_s$ is still recognizable, although occupancy at somewhat higher momenta are beginning to rise. At intermediate times ($t = 30/Q_s$) the Nielsen-Olesen instability has dramatically increased the typical occupation numbers, especially for low momenta. On the other side overpopulation of modes with $|\mathbf{p} \leq Q_s$ in the ”Fluctuation IC” scenario has decreased while particles and energy have been transported to short length scales (high momentum modes). This process holds on even at late times ($t = 210/Q_s$), the particle spectrum is now exhibiting a power-law distribution with exponent $\kappa = 3/2$. This particular value of the exponent has been already found in [58] at comparable time scales. For much later times the power-law exponent should slightly decrease and approach first $\kappa = 4/3$ [56, 59] and even later become indistinguishable from the classical thermal exponent $\kappa_{\text{th}} = 1$ [75].

Astonishingly, at the latest times shown here, the Nielsen-Olesen spectrum has become almost identical to the spectrum of the initially overpopulated state. Both distributions share the turbulent power-law exponent κ, the remaining differences between them may be explained by a small variation in the total energy density or significant variations in the particle yields for quarks. A direct consequence of these observations is that at later

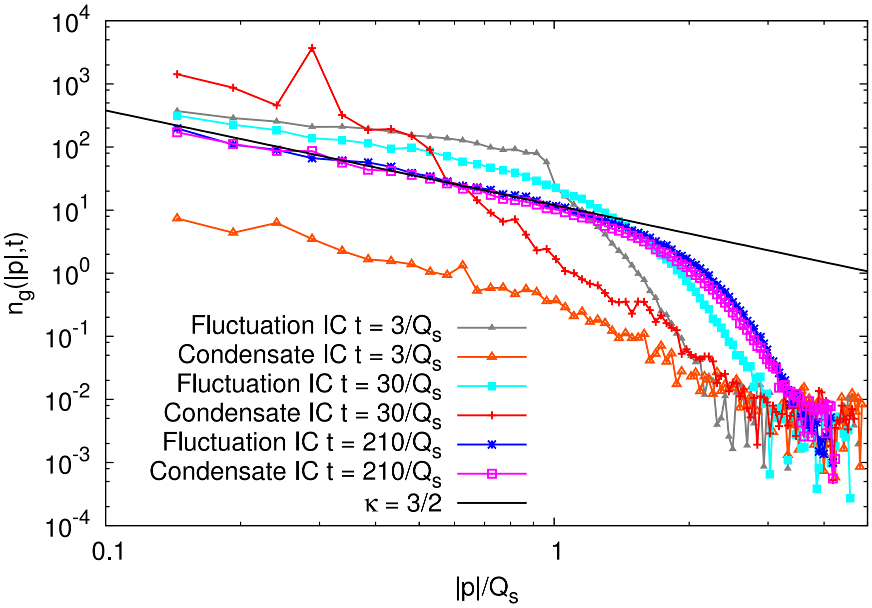

Figure 6.18.: Universal isotropic turbulent attractor for gluons. Two different initial conditions (gluonic overpopulation and a Nielsen-Olesen instability) independently converge to the same scaling regime.

times the gluon dynamics becomes apparently universal and follows the trajectory of an isotropic and overpopulated turbulent regime.

Can the same universality be found in properties of fermions or is the pattern of quark production during Nielsen-Olesen instability entirely distinct from the production driven by initial overpopulation? This issue is addressed in Fig. 6.19, where the total number of quarks [4] is plotted as a function of time for both types of initial conditions. We observe that in both cases the quark number jumps at very early times. For the Nielsen-Olesen instability this is an effect caused by the sudden switching-on of the macroscopic gauge field, which is not contained in the fermionic vacuum state. In the case of overpopulated initial conditions this fast increase proceeds smoothly. We interpret this as fast production of low momentum quarks from gluonic scattering and decay. The rapidity of initial production is most probably due to an almost vanishing quark mass (here $m_\psi \leq 10^{-2} Q_s$) and the effective absence of Pauli suppression at very early times.

From early on Nielsen-Olesen instability has lead to a higher total particle number of quarks. This is also recovered in the corresponding particle spectra at early times, depicted in Fig. 6.20. The Nielsen-Olesen spectrum overshoots the one resulting from ini-

---

[4] Defined by $N_\psi(t) = \int \frac{d^3p}{(2\pi)^3}\, n_\psi(\mathbf{p},t)$

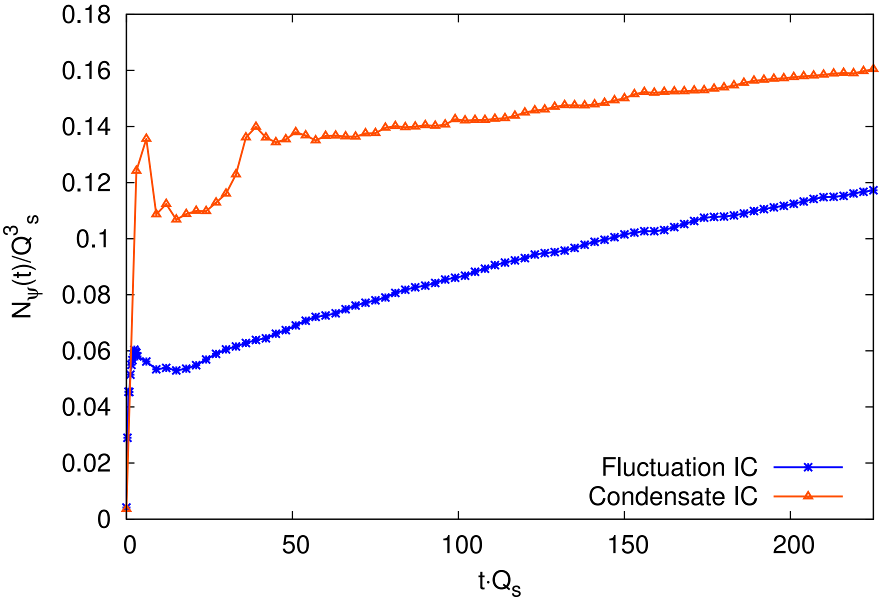

Figure 6.19.: Time evolution of the total quark particle number starting from gluonic overpopulation and a Nielsen-Olesen instability.

tial overpopulation for the whole available momentum range, confirming our conclusions from Fig. 6.19 for early time dynamics. However, the subsequent time evolution marked by steady fermion production tends to narrow the gap between the two scenarios. How does this difference in the total number of quarks translate into the momentum dependent particle spectra? In Fig. 6.21 quark spectra at late times ($t = 210/Q_s$) are compared to each other. Although there are obviously more quarks present after the Nielsen-Olesen instability, the spectra are remarkably similar. The most distinctive feature of both distributions is a power-law in the middle and high momentum range. The measured exponents are very close to each other, suggesting that both trajectories are following a similar path in their time evolution. What is the nature of this power-law? It could be for instance an example of quantum turbulence caused by energy transport to the ultraviolet via the emergence of quarks with higher momenta or a phenomenon completely determined by the gluonic sector. The latter explanation is supported by the fact that the value of the fermionic power-law exponent, $\kappa_\psi \simeq 1.7 - 1.75$, is close to $\kappa = 3/2$, found for the gluon turbulent attractor on same time scales.

This similarity also holds for the quark content produced in the flux-tube scenario. In Fig. 6.22 we combined gluonic and quark spectra at intermediate times. For both species a power-law regime is established on these timescales. Astonishingly, quarks seem to continue the gluonic power-law to higher momenta albeit at much lower amplitude. The

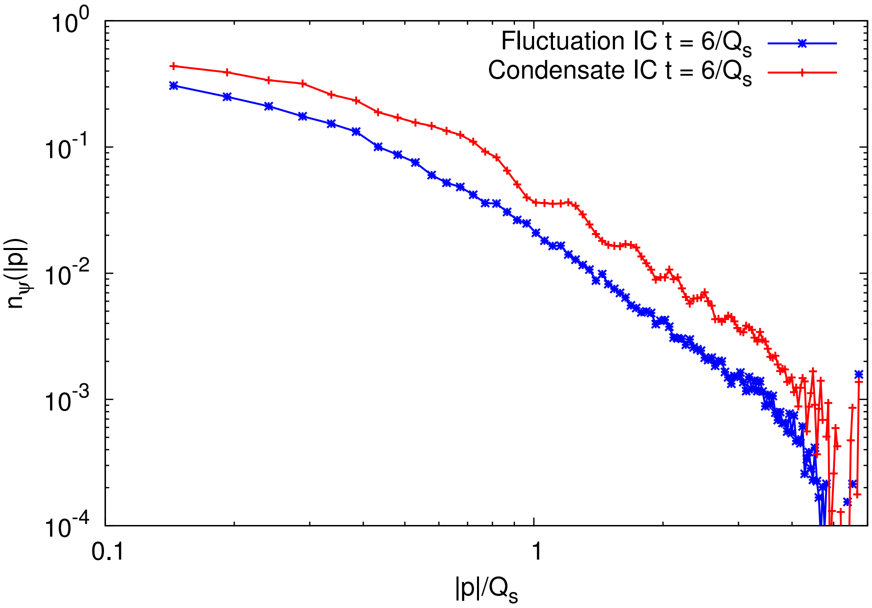

Figure 6.20.: Quark particle spectra at early times for gluonic overpopulation and a Nielsen-Olesen instability.

agreement between exponents for bosons and fermions suggests that there is a causal connection between them. Since the energy content of the whole system at these small values of the gauge coupling and for not too late times is dominated by gluonic fluctuations, it is plausible to assume that the specific features of the quark distribution, particularly the power-law shape at higher momenta, are determined by gluonic decay and scattering processes. In a sense quarks are inheriting the spectral properties of bosonic particle distributions, an effect we already observed for scalar fields in Sec. 5.1.

6.3.3. Conclusions

We have studied gluon dynamics and quark production in two colour QCD with two light quark flavours. We limited our discussion to the weakly coupled regime in order to guarantee the applicability of the classical-statistical approximation for the gluon sector, while we simulated the quark dynamics in a stochastic approach without further approximations. In future studies we plan to increase the gauge coupling and to explore the range of applicability of our lattice methods at stronger couplings. Having considered three types of initial conditions, we confirmed the universality of the non-thermal fixed point existing in overpopulated gluonic systems and demonstrated how the turbulent regime is approached by trajectories of time evolution, although all of them start from very different

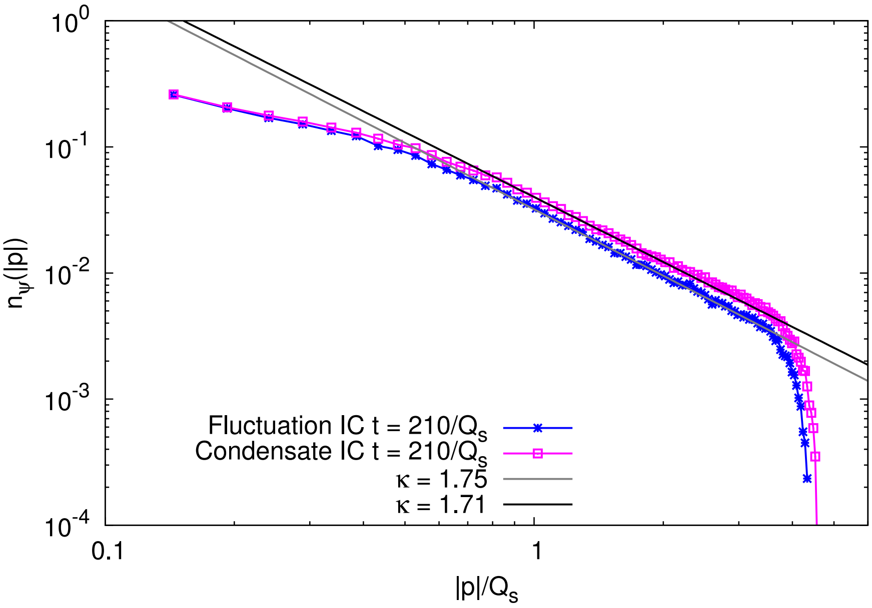

Figure 6.21.: Emergence of a power-law in the quark sector from two different initial conditions (gluonic overpopulation and a Nielsen-Olesen instability).

initial states. The power-law exponents we found in the gluonic sector are in agreement with earlier investigations of turbulence in classical-statistical Yang-Mills simulations.

Most importantly for the gluon dynamics, we showed that anisotropic initial conditions leading to chromomagnetic plasma instabilities and Schwinger pair production in QCD isotropize rather quickly and that their subsequent approach to thermal equilibrium via energy cascade to short length scales can be described in an entirely isotropic framework.

The mentioned universality of the gluon dynamics has a profound effect on quark production. Although very different at early stages, the total numbers of quarks produced from magnetic instabilities and gluonic overpopulation tend to approach each other at later times. The corresponding spectral distributions of quark particle numbers for all three types of initial conditions acquire a universal shape marked by an unsuspected power-law at intermediate momenta. Surprisingly, the values of the fermionic power-law exponent turn out to be very close to the ones appearing in the gluonic sector via the energy cascade. This observation suggests that the spectral properties of the quark particle distribution at the coupling strengths considered here are to a large degree determined by the behaviour of the non-thermal turbulent fixed point existing in the gluon sector.

We believe that our observations will complete the prevailing picture of turbulence in the non-Abelian gauge theory [56, 59, 57, 58] by adding information about dynamics of quark production in overoccupied QCD matter.

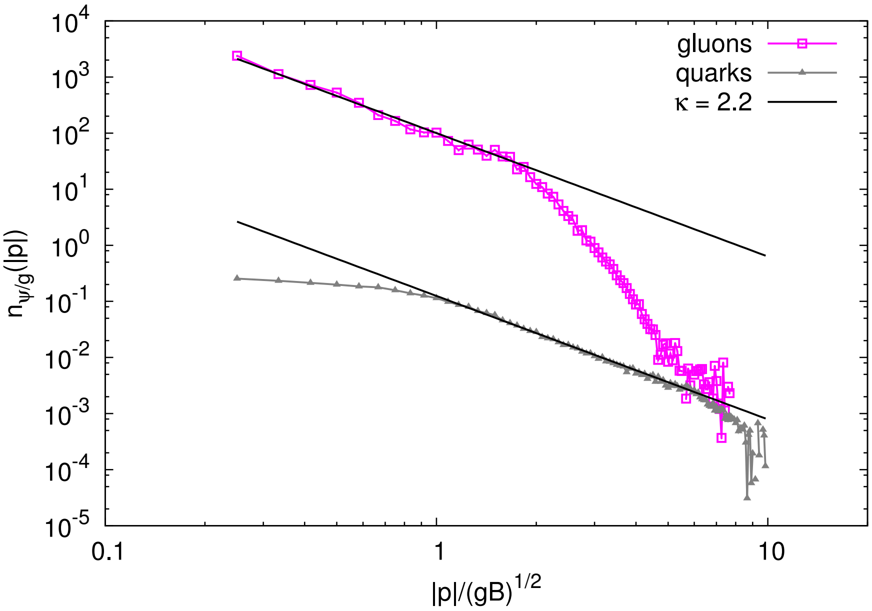

Figure 6.22.: Shape and typical features of gluon and quark particle spectra emerging from flux-tube decay at $t = 17.3/\sqrt{gB}$.

Chapter 7.

Conclusions and Outlook

The purpose of this thesis was to study fermion production for three different applications across the wide area of non-equilibrium phenomena in quantum field theory: the post-inflationary epoch, in the early stages of heavy-ion collisions and from ultra-intense laser beams. This goal was accomplished by applying modern computational lattice techniques, which have been advanced and tested in the course of this work. In this chapter we intend to recapture the essential results and conclusions drawn from our studies and give an outlook for directions of future research in these and adjacent areas.

In Chap. 5 we continued the line of investigations of fermion production during preheating after inflation building on our earlier work which began in [7]. Having coupled a 3 + 1 dimensional linear-sigma model undergoing parametric resonance to fermions in Sec. 5.1, we confirmed our previous findings of the strong enhancement of fermion production occurring in presence of highly occupied bosonic fields. We were able to improve our analytic understanding of this phenomenon based on kinetic Boltzmann equations, with matrix elements evaluated at leading order in perturbation theory. To check the reliability of these findings, we compared the well established two-particle irreducible (2PI) effective action approach and two different real-time lattice methods (mode functions and male/female fermions). We observed a high degree of agreement between 2PI and classical-statistical lattice simulations with fermions at weak effective couplings. In this regime we also found an unpredicted ultraviolet power-law distribution of fermions, which builds up when the bosonic sector is trapped in a nonthermal fixed-point marked by turbulent cascades.

Before investigating stronger coupled scenarios, we tested the stochastic low-cost approach of simulating fermions on a real-time lattice (male/female fermions, Sec. 4.2) against a more rigorous but also computationally far more expensive methd, the mode functions expansion (Sec. 4.1). We showed that the stochastic lattice computations successfully converge to the exact results for a realistically achievable number of male/female pairs. By using lattice simulations with male/female fermions for parametric resonance at stronger effective couplings, we observed that fermions tend to take on a quasi-thermal Fermi-Dirac distribution. From this we were able to extract the time-dependent temperature parameter and register the heating of the fermion sector.

A different preheating scenario, marked by a tachyonic instability, was investigated in Sec. 5.2. There we utilized a simple scalar model with fermions which become and remain massive during the instability. Our choice of a particular model of tachyonic preheating was motivated by the availability of analytic predictions for the total fermion output during this type of initial dynamics after inflation. However, our numerical computations indicate that the mentioned leading-order results underestimate the number of produced fermions for a wide range of couplings by several orders of magnitude. In particular, the enhancement w.r.t. to the leading-order approximations is much more pronounced than in the case of parametric resonance. Another consequence of the increased total fermion number is that, contrary to existing analytical expectations, the emergent fermionic distribution is far from the non-relativistic limit.

Both of our studies of preheating with fermions have shown that existing expectations for the magnitude of fermion production have to be significantly raised. This finding could become crucial for calculations of baryogenesis and generation of gravitational waves during preheating. The steady improvement of lattice techniques may soon allow us to directly compute the reheating temperature for a given model of inflation. This would be a great contribution to the quest for the microscopic foundations of inflation.

In Chap. 6 we turned our attention to fermion production in gauge theories. At first we investigated in Sec. 6.1 the Schwinger pair production of fermion/anti-fermion pairs in a 1 + 1 dimensional Abelian gauge theory (massive Schwinger model). Applying our lattice techniques and concentrating on gauge-invariant observables we successfully reproduced the analytically known pair production rate predicted by the famous Schwinger formula. After this first test we went beyond the linear regime and included the backreaction of the produced fermions onto the homogeneous electric field. Thus we were able to numerically describe plasma oscillations and damping of the field due to interaction with fermions. Considering external field profiles resembling single laser pulses which are inhomogeneous in space and time, we were able to consistently solve the initial value problem for such a system for the first time including backreaction effects. Most remarkably, we observed the creation of oppositely charged bunches of particles flying apart after the duration of the pulse and converting their kinetic energy into a constant electric field between them. This emergence of a constant field strength between separated charges is analogous to the formation of a string between fundamental colour charges in QCD.

We devoted Sec. 6.2 to a detailed study of this exciting phenomenon resembling the confinement property of strong interactions. Therefore we initialized our simulations with two separated external charges of opposite sign and increased the distance between them until pair production became efficient enough to break the string. Our real-time lattice approach allowed us to resolve this process in time and distinguish its two stages. In the first stage, spontaneous pair production slightly reduces the original field strength in the string and places both positively and negativity charged fermions on top of each other. As it happens their total charge at every point along the string remains zero and is unable to screen the field of the external charges. The second stage, which depletes the energy content of the string, sets in when the produced particles and anti-particles are accelerated into opposite directions. This process of charge separation, which lasts much longer than the first stage, screens the external charges from each other and is ultimately responsible for the string breaking.

These findings imply that the traditional picture of instantaneous string breaking neglects the energy needed for screening of the charges and has to be revised. Additionally, we provided a simple model for estimations of the critical string length. The insight into the time resolved string breaking process that we gained might be used to improve our understanding of the decay and dynamical properties of quarkonia.

Finally, in Sec. 6.3 we simulated two colour QCD with light quarks for three different types of initial conditions (overpopulation, Nielsen-Olesen instability and flux-tube decay), all of them expected to be relevant for the early stages of heavy-ion collisions at sufficiently high energies. Our studies have been conducted in the regime of weak gauge couplings and large occupancies, ensuring the validity of the classical-statistical approximation in this non-perturbative regime. For anisotropic initial states we observed a fast isotropization accompanied by the decay of initial macroscopic fields, allowing us a direct comparison with isotropic initial conditions. Such a comparison was made by keeping the energy density fixed for both Nielsen-Olesen and overpopulated states. Both trajectories converged to the same non-thermal fixed point, characterized by a turbulent energy cascade towards short length scales with an intermediate value of the scaling exponent $\kappa = 3/2$. Remarkably, the quark sector was found to exhibit universality as well. This was detected by realizing that fermion spectra from these two types of initial conditions, being very diverse at initial times, approach each other in the long time limit. Even more surprising was the appearance of power-laws in the quark particle spectra at intermediate momenta, reminding us of the similar effect that we found in Sec. 5.1. The measured exponents for the simulated periods of time agreed rather well with those occurring in the gluonic sector, suggesting a connection between these two phenomena.

Our first results for quark production in the early phase of heavy-ion collisions exhibit once again the universality of the isotropic turbulent attractor at weak gauge couplings. The properties of this non-thermal fixed-point have been extended to incorporate the behaviour of the quark sector. The peculiar copying of bosonic scaling solutions by fermions needs further investigations, it could be a universal phenomenon detectable e.g. in experiments with ultra cold quantum gases.

For both heavy-ion experiments and early Universe cosmology an extension of the available lattice fermion techniques towards isotropically and anisotropically expanding geometries seems desirable. For cosmological applications we envision to apply our methods to models of preheating most compatible with recent experimental observations [101]. Concerning the appearance of fermionic power-law distributions in scalar and gauge theories, we intend to make analytic progress in understanding the nature of this effect. In QCD there are many possible directions of further research, one of them would be to increase the values of the gauge coupling in our simulations in order to come closer to the realistically expected values at the energy scales of modern heavy-ion colliders.

However, on this path we are limited by the classical-statistical approximation, which is prone to fail at strong coupling. To cure this problem an inclusion of quantum fluctuations into existing lattice methods would be required, which may be approximately achieved by using inhomogeneous 2PI techniques described in [129].

Appendix A.

Marginal distributions for Schwinger model

The definition of the lattice Wigner function (6.54) is such that we reproduce the continuum expressions for its marginal distributions:

$$\begin{aligned} \mathcal{W}_{\mathcal{X}}(x,t) &= -F(x,x;t)\,, && \text{(A.1a)} \\ \mathcal{W}_{\mathcal{P}}(p,t) &= -\int dx_1 dx_2 e^{-ip(x_1-x_2)} \tilde{F}(x_1,x_2;t)\,. && \text{(A.1b)} \end{aligned}$$

Regarding the position space marginal distribution on the lattice, we consider:

$$\mathcal{W}_{\mathcal{X}}(l,j) = \frac{1}{2L} \sum_{q\in\tilde{\Lambda}_{\mathcal{W}}} \mathcal{W}(l,q,j)\,. \tag{A.2}$$

Upon performing the summation over q, we encounter:

$$\sum_{q\in\tilde{\Lambda}_{\mathcal{W}}} e^{\pi i(l-2k)q/N} = 2N\delta_{2k,l}\,. \tag{A.3}$$

The Kronecker delta indicates that $\mathcal{W}(l,j)$ is only non-vanishing for even l:

$$\mathcal{W}_{\mathcal{X}}(l,j) = -F(l,l;j)\,, \tag{A.4}$$

with $l \in \Lambda$.

Regarding the momentum space marginal distribution on the lattice, we consider:

$$\mathcal{W}_{\mathcal{P}}(q,j) = \frac{a_s}{2} \sum_{l\in\Lambda_{\mathcal{W}}} \mathcal{W}(l,q,j)\,. \tag{A.5}$$

Due to the fact that we used the module operation in (6.54), we obtain:

$$\begin{aligned} &\sum_{l=0}^{2N-1} e^{\pi ilq/N} \tilde{F}(k,[l-k]_N;j) = \\ &\qquad (1+e^{i\pi q}) \sum_{l=0}^{N-1} e^{\pi ilq/N} \tilde{F}(k,[l-k]_N;j)\,. \end{aligned} \tag{A.6}$$

The factor $(1 + e^{i\pi q})$ shows that $\mathcal{W}(q, j)$ is only non-vanishing for even q. Accordingly, if we redefine the summation indices:

$$l_1 = l \in \Lambda \qquad \text{and} \qquad l_2 = [l - k]_N \in \Lambda \,, \tag{A.7}$$

we reproduce the analogue of (A.1b):

$$\mathcal{W}_{\mathcal{P}}(q, j) = -a_s^2 \sum_{l_1 \in \Lambda} \sum_{l_2 \in \Lambda} e^{-2\pi i q (l_1 - l_2)/N} \tilde{F}(l_1, l_2; j) \,, \tag{A.8}$$

with $q \in \tilde{\Lambda}$.

Appendix B.

Analytic results for pair production in electric fields

We briefly review some analytic results for the static background field [112]. As a matter of fact, the Dirac equation is analytically solvable for $E(x,t) = E_0$ in terms of parabolic cylinder functions $D_\nu(z)$. Accordingly, it is also possible to compute $\mathcal{W}(x,p,t)$ explicitly.

The pseudo-distributions $m(x,p,t)$, which have been introduced in Sec. 6.1.1.2, are then given by:

$$\begin{aligned} \varrho(x,p,t) &= 0\,, && \text{(B.1a)}\\ \epsilon(x,p,t) &= [2f(p)-1]\omega\,, && \text{(B.1b)}\\ n^{\pm}(x,p,t) &= f(p)\,. && \text{(B.1c)} \end{aligned}$$

The function $f(p)$ is usually denotes as the single-particle momentum distribution:

$$f(p) = \frac{1}{2}e^{-\pi/4\epsilon}\left[\frac{1}{2\epsilon}\left(1-\frac{p}{\omega}\right)\mathcal{D}_1(p) + \left(1+\frac{p}{\omega}\right)\mathcal{D}_2(p) - \frac{m}{\sqrt{2\epsilon}\,\omega}\mathcal{D}_3(p)\right]\,, \tag{B.2}$$

with

$$\begin{aligned} \mathcal{D}_1(p) &= \left|D_{-1+i/2\epsilon}(\hat{p})\right|^2\,, && \text{(B.3a)}\\ \mathcal{D}_2(p) &= \left|D_{i/2\epsilon}(\hat{p})\right|^2\,, && \text{(B.3b)}\\ \mathcal{D}_3(p) &= e^{i\pi/4}D_{i/2\epsilon}(\hat{p})D_{-1-i/2\epsilon}(\hat{p}^*) + c.c.\,, && \text{(B.3c)} \end{aligned}$$

and

$$\hat{p} = -\sqrt{\frac{2}{\epsilon}}\frac{p}{m}e^{-i\pi/4}\,. \tag{B.4}$$

We note that $f(p)$ is independent of the time variable t. It can be shown that $f(p)$ vanishes for small momenta and approaches a non-vanishing constant for large momenta:

$$\begin{aligned} \lim_{p\to-\infty} f(p) &= 0\,, && \text{(B.5a)}\\ \lim_{p\to\infty} f(p) &= \exp\left(-\frac{\pi}{\epsilon}\right)\,. && \text{(B.5b)} \end{aligned}$$

As the expressions (B.1) are spatially homogeneous, they are trivially related to the momentum space marginal distributions $m_{\mathcal{P}}(p,t)$:

$$m(x,p,t) = \frac{m_{\mathcal{P}}(p,t)}{L} \,, \tag{B.6}$$

in the infinite volume $L \to \infty$. Most notably, the rate at which particles and anti-particles are created is a constant, so that the total number of particles and anti-particles, respectively, which are created per volume L and time T is given by:

$$\frac{\Delta n^{\pm}}{LT} = \frac{eE_0}{2\pi} \exp\left(-\frac{\pi m^2}{eE_0}\right) = \frac{m^2 \epsilon}{2\pi} \exp\left(-\frac{\pi}{\epsilon}\right) \,. \tag{B.7}$$

Appendix C.

Gamma matrices and lattice definitions of Dirac eigenspinors

The use of a pseudoscalar Wilson term determines the explicit form of the Dirac eigenspinors on the lattice:

$$
u_1(\mathbf{p}) = \sqrt{\frac{E+m}{2E}} \begin{pmatrix} 1 \\ 0 \\ \frac{p_z - \frac{ira_s}{2}(\mathbf{p})^2_{lat}}{E+m} \\ \frac{p_x+ip_y}{E+m} \end{pmatrix} \quad u_2(\mathbf{p}) = \sqrt{\frac{E+m}{2E}} \begin{pmatrix} 0 \\ 1 \\ \frac{p_x-ip_y}{E+m} \\ \frac{-p_z - \frac{ira_s}{2}(\mathbf{p})^2_{lat}}{E+m} \end{pmatrix}
$$

$$
v_1(\mathbf{p}) = \sqrt{\frac{E+m}{2E}} \begin{pmatrix} \frac{-p_z - \frac{ira_s}{2}(\mathbf{p})^2_{lat}}{E+m} \\ \frac{-p_x-ip_y}{E+m} \\ 1 \\ 0 \end{pmatrix} \quad v_2(\mathbf{p}) = \sqrt{\frac{E+m}{2E}} \begin{pmatrix} \frac{-p_x+ip_y}{E+m} \\ \frac{p_z - \frac{ira_s}{2}(\mathbf{p})^2_{lat}}{E+m} \\ 0 \\ 1 \end{pmatrix} \tag{C.1}
$$

The standard definition of Gamma matrices is:

$$
\gamma_0 = \begin{pmatrix} 1 & 0 & 0 & 0 \\ 0 & 1 & 0 & 0 \\ 0 & 0 & -1 & 0 \\ 0 & 0 & 0 & -1 \end{pmatrix} \quad \gamma_1 = \begin{pmatrix} 0 & 0 & 0 & 1 \\ 0 & 0 & 1 & 0 \\ 0 & -1 & 0 & 0 \\ -1 & 0 & 0 & 0 \end{pmatrix} \quad \gamma_2 = \begin{pmatrix} 0 & 0 & 0 & -i \\ 0 & 0 & i & 0 \\ 0 & i & 0 & 0 \\ -i & 0 & 0 & 0 \end{pmatrix}
$$

$$
\gamma_3 = \begin{pmatrix} 0 & 0 & 1 & 0 \\ 0 & 0 & 0 & -1 \\ -1 & 0 & 0 & 0 \\ 0 & 1 & 0 & 0 \end{pmatrix} \quad \gamma_5 = \begin{pmatrix} 0 & 0 & 1 & 0 \\ 0 & 0 & 0 & 1 \\ 1 & 0 & 0 & 0 \\ 0 & 1 & 0 & 0 \end{pmatrix} \tag{C.2}
$$

Acknowledgement

At this point I would like to thank all the people who supported me during the years of my PhD studies and without whom this work could never be written.

First of all, I would like to thank my supervisor Jürgen Berges for giving me this exciting research topic and for bringing me to the wonderful city of Heidelberg. I have enjoyed and benefited from the atmosphere of cooperation and mutual support which he so strongly encourages in his work group. I am deeply grateful for our fruitful conversations, for enabling me to participate in many conferences and workshops and for his invaluable career advice.

I thank my collaborator Florian Hebenstreit for many insightful discussions about pair production and string breaking and especially for his patience and help during my struggles with gauge theories. I owe my gratitude to Dénes Sexty for sharing his numerical expertise and for always giving a profound and refreshing feedback.

I would like to thank all my present and former colleagues from Heidelberg and Darmstadt, namely Kirill Boguslavski, David Mesterhazy, Sören Schlichting, Valentin Kasper, Jean-Sebastian Gagnon, Thorsten Zöller, Jan Stockemer, Leticia Palhares, Alexander Rothkopf, Benjamin Wallisch, Asier Piniero Orioli, Niklas Müller, Onirban Islam, Sebastian Scheffler and Sebastian Ohmer for their friendliness, encouragement and cooperation. It was a great experience to learn from you and share our ideas!

I will also keep the memory of my former colleague Stefan Roth, who passed away so tragically.

Special thanks go to Kirill Boguslavski, Valentin Kasper and Benjamin Wallisch for proof-reading of major parts of this thesis. Of course, every remaining typo is completely my fault.

I would like to thank my parents, grandparents and my entire family for their support and encouragement. You have been my backbone through all these years.

I thank the HGS-HIRe graduate school for its unbureaucratic financial support and for organizing so many exciting events. I am also grateful to Luca Amendola, Kurt Roth and Norbert Christlieb for their agreement to take part in my examination.

I deeply apologise to everyone whom I might have forgotten here!

Heidelberg, 12. May 2014

Bibliography

[1] U. W. Heinz, J. Phys. Conf. Ser. **455** (2013) 012044.

[2] J. Berges, Nucl. Phys. A **820** (2009) 65C.

[3] D. Tytler, J. M. O'Meara, N. Suzuki, and D. Lubin, Phys. Scrip. T **85** (2000) 12.

[4] B. D. Fields, Ann. Rev. Nucl. Part. Sci. **61** (2011) 47-68.

[5] P. Romatschke, Int. J. Mod. Phys. E **19** (2010) 1.

[6] J. Berges, AIP Conf. Proc. **739** (2005) 3; arXiv:hep-ph/0409233.

[7] J. Berges, D. Gelfand and J. Pruschke, Phys. Rev. Lett. **107** (2011) 061301.

[8] A. H. Guth, Phys. Rev. D **23** (1981) 347.

[9] A. D. Linde, Phys. Lett. B **108** (1982) 389-393.

[10] B. Ryden, "Introduction to Cosmology", Benjamin Cummings (2002).

[11] D. H. Lyth and A. R. Liddle, "Primordial Density Perturbations", Cambridge University Press (2009).

[12] D. N. Schramm and M. S. Turner, Rev. Mod. Phys. **70** (1998) 303-318.

[13] A. D. Dolgov, Phys. Rept. **222** (1992) 309.

[14] L. Kofman, A. D. Linde and A. A. Starobinsky, Phys. Rev. Lett. **73** (1994) 3195.

[15] J. H. Traschen and R. H. Brandenberger, Phys. Rev. D **42** (1990) 2491.

[16] S. Y. Khlebnikov and I. I. Tkachev, Phys. Rev. Lett. **77** (1996) 219.

[17] J. Berges and J. Serreau, Phys. Rev. Lett. **91** (2003) 111601.

[18] T. Prokopec and T. G. Roos, Phys. Rev. D **55** (1997) 3768.

[19] J. Berges, A. Rothkopf and J. Schmidt, Phys. Rev. Lett. **101** (2008) 041603.

[20] R. Micha and I. I. Tkachev, Phys. Rev. Lett. **90** (2003) 121301.

[21] J. Baacke, K. Heitmann and C. Patzold, Phys. Rev. D **58** (1998) 125013; P. B. Greene and L. Kofman, Phys. Lett. B **448** (1999) 6; G. F. Giudice et al., JHEP **9908** (1999) 014; J. Garcia-Bellido, S. Mollerach and E. Roulet, JHEP **0002** (2000) 034; M. Peloso and L. Sorbo, JHEP **0005** (2000) 016; J. Baacke, N. Kevlishvili and J. Pruschke, JCAP **0706** (2007) 004.

[22] G. Aarts and J. Smit, Nucl. Phys. B **555** (1999) 355.

[23] S. Borsanyi and M. Hindmarsh, Phys. Rev. D **79** (2009) 065010.

[24] K. Nakamura, Nucl. Part. Phys. **37** (2010) 075021.

[25] R. Devenish and A. Cooper-Sarkar, ”Deep inelastic scattering”, Oxford University Press (2004).

[26] W. Bock et al., Z. Phys. **C45**, 597 (1990)

[27] F. Knechtli and R. Sommer, Phys. Lett. **B440** (1998) 345; Nucl. Phys. **B590** (2000) 309.

[28] O. Philipsen and H. Wittig, Phys. Rev. Lett. **81** (1998) 4056.

[29] F. Gliozzi and A. Rago, Nucl. Phys. **B714** (2005) 91.

[30] G. S. Bali *et al.* [SESAM Collaboration], Phys. Rev. D **71** (2005) 114513.

[31] M. Pepe and U. -J. Wiese, Phys. Rev. Lett. **102** (2009) 191601.

[32] D. Banerjee, M. Dalmonte, M. Muller, E. Rico, P. Stebler, U.-J. Wiese and P. Zoller, Phys. Rev. Lett. **109** (2012) 175302.

[33] E. Zohar, J. I. Cirac and B. Reznik, Phys. Rev. A **88** (2013) 023617.

[34] L. Tagliacozzo, A. Celi, A. Zamora, and M. Lewenstein, Ann. Phys. **330** (2013) 160.

[35] D. Marcos, P. Rabl, E. Rico and P. Zoller, Phys. Rev. Lett. **111** (2013) 110504.

[36] D. J. Gross and F. Wilczek, Phys. Rev. Lett. **30** (1973) 1343; H. D. Politzer, Phys. Rev. Lett. **30** (1973) 1346.

[37] A. Bazavov *et al.*, Phys. Rev. D **85** (2012) 054503; Y. Aoki, Z. Fodor, S. D. Katz and K. K. Szabo, JHEP **0601** (2006) 089.

[38] B-J. Schaefer, M. Wagner and J. Wambach, Phys. Rev. D **81** (2010) 074013.

[39] C. S. Fischer and J. Luecker, Phys. Lett. B **718** (2013) 1036-1043.

[40] J. Braun, L. M. Haas, F. Marhauser and J. M. Pawlowski, Phys. Rev. Lett. **106** (2011) 022002.

[41] P. de Forcrand, PoS LAT **2009** (2009) 010. arXiv:1005.0539 [hep-lat].

[42] Y. Akiba, Prog. Theor. Phys. Supplement **187** (2011) 55-67.

[43] J. Adams et. al., Nucl. Phys. A **757** (2005) 102; K. Adcox et. al., *ibid.* 757 (2005) 184; I. Arsene et. al., *ibid.* **757** (2005) 1; B. B. Back et. al., *ibid.* 757 (2005) 28.

[44] M. M. Aggarwal *et al.* (STAR Collaboration), Phys. Rev. Lett. **105** (2010) 022302.

[45] P. Romatschke and U. Romatschke, Phys. Rev. Lett. **99** (2007) 172301.

[46] F. Gelis, E. Iancu, J. Jalilian-Marian and R. Venugopalan, Ann. Rev .Nucl .Part. Sci. **60** (2010) 463-489.

[47] J. Berges, and S. Schlichting, Phys. Rev. D **87** (2013) 014026.

[48] J. Berges, K. Boguslavski, S. Schlichting and R. Venugopalan, Phys. Rev. D **89** (2014) 074011.

[49] J. Berges, K. Boguslavski, S. Schlichting and R. Venugopalan, arXiv:1311.3005 [hep-ph].

[50] A. Kurkela and G. D. Moore, Phys. Rev. D **86** (2012) 056008.

[51] A. Kurkela and G. D. Moore, JHEP **1111** (2011) 120; A. Kurkela and G. D. Moore, JHEP **1112** (2011) 044.

[52] M. Attems, A. Rebhan and M. Strickland, Phys. Rev. D **87** (2013) 025010; A. Ipp, A. Rebhan and M. Strickland, Phys. Rev. D **84** (2011) 056003; P. Romatschke and A. Rebhan, Phys. Rev. Lett. **97** (2006) 252301.

[53] T. Epelbaum and F. Gelis, Phys. Rev. Lett. **111** (2013) 232301.

[54] K. Fukushima and F. Gelis, Nucl. Phys. A **874** (2012) 108-129.

[55] J. Berges, S. Scheffler, and D. Sexty, Phys. Rev. D **77** (2008) 034504.

[56] J. Berges, S. Scheffler, and D. Sexty, Phys. Lett. B **681** (2009) 362.

[57] J. Berges, D. Gelfand, S. Scheffler, and D. Sexty, Phys. Lett. B **677** (2009) 210.

[58] J. Berges, S. Schlichting, and D. Sexty, Phys. Rev. D **86** (2012) 074006.

[59] S. Schlichting, Phys. Rev. D **86** (2012) 065008.

[60] F. Gelis, K. Kajantie and T. Lappi, Phys. Rev. C **71** (2005) 024904.

[61] F. Gelis, K. Kajantie and T. Lappi, Phys. Rev. Lett. **96** (2006) 032304.

[62] Y. V. Kovchegov, Rept. Phys. **75** (2012) 124301.

[63] W. Florkowski, R. Ryblewski and M. Strickland, Nucl. Phys. A **916** (2013) 249; D. Bazow, U. W. Heinz and M. Strickland, arXiv:1311.6720 [nucl-th].

[64] G. Aarts and J. Berges, Phys. Rev. Lett. **88** (2002) 041603.

[65] J. Berges and T. Gasenzer, Phys. Rev. A **76** (2007) 033604.

[66] V. Kasper, F. Hebenstreit and J. Berges, arXiv:1403.4849 [hep-ph].

[67] A. Arrizabalaga, J. Smit and A. Tranberg, JHEP **0410** (2004) 017.

[68] F. Sauter, Z. Phys. **69** (1931) 742.

[69] W. Heisenberg and H. Euler, Z. Phys. **98** (1936) 714.

[70] J. S. Schwinger, Phys. Rev. **82** (1951) 664.

[71] J. Berges, S. Scheffler, S. Schlichting and D. Sexty, Phys. Rev. D **85** (2012) 034507.

[72] H. Fujii, K. Itakura, A. Iwazaki, Nucl. Phys. **A828** (2009) 178.

[73] J. Berges and G. Hoffmeister, Nucl. Phys. B **813** (2009) 383-407.

[74] J. Berges, A. Rothkopf, and J. Schmidt, Phys. Rev. Lett. **101** (2008) 041603.

[75] M. C. A. York, A. Kurkela, E. Lu and G. D. Moore, arXiv:1401.3751 [hep-ph].

[76] R. Micha and I. I. Tkachev, Phys. Rev. D **70** (2004) 043538.

[77] G. Aarts, G. F. Bonini, and C. Wetterich, Phys. Rev. D **63** (2001) 025012.

[78] J. Berges, Nucl. Phys. A **699** (2002) 847; G. Aarts, D. Ahrensmeier, R. Baier, J. Berges and J. Serreau, Phys. Rev. D **66** (2002) 045008.

[79] J. Berges and D. Sexty, Phys. Rev. D **83** (2011) 085004.

[80] J. Berges and D. Sexty, Phys. Rev. Lett. **108** (2012) 161601.

[81] B. Nowak, D. Sexty and T. Gasenzer, Phys. Rev. B **84** (2011) 020506.

[82] T. Gasenzer, L. McLerran, J. M. Pawlowski and D. Sexty, arXiv:1307.5301 [hep-ph].

[83] M. Garny and M. M. Muller, Phys. Rev. D **80** (2009) 085011.

[84] J. Berges, J. Cox, Phys. Lett. B **514** (2001) 369-374.

[85] J. Berges, S. Borsanyi and J. Serreau, Nucl. Phys. B **660** (2003) 51.

[86] S. Borsanyi, U. Reinosa, Phys. Lett. B **661** (2008) 88-94.

[87] A. A. Vlasov, J. Exp. Theor. Phys. **8** (3)(1938) 291.

[88] M. Lindner and M. M. Muller, Phys. Rev. D **73** (2006) 125002.

[89] P. M. Saffin and A. Tranberg, JHEP **1107** (2011) 066.

[90] P. M. Saffin and A. Tranberg, JHEP **1202** (2012) 102.

[91] Z. -G. Mou, P. M. Saffin, and A. Tranberg, JHEP **1311** (2013) 097.

[92] I. Montvay and G. Münster, *Quantum Fields on a Lattice* (Cambridge University Press, Cambridge, England, 1997); C. Gattringer and C. B. Lang, *Quantum Chromodynamics on the Lattice* (Springer, Berlin, 2010).

[93] W. Bietenholz *et al.* (XLF Collaboration), JHEP D **0412** (2004) 044.

[94] F. Hebenstreit, J. Berges, and D. Gelfand, Phys. Rev. D **87** (2013) 105006.

[95] F. Hebenstreit, J. Berges, and D. Gelfand, Phys. Rev. Lett. **111** (2013) 201601.

[96] J. Berges, J. Pruschke and A. Rothkopf, Phys. Rev. D **80** (2009) 023522.

[97] J. Berges and S. Borsanyi, Phys. Rev. D **74** (2006) 045022.

[98] M. Lindner and M. M. Muller, Phys. Rev. D **77** (2008) 025027.

[99] G. Aarts and J. Smit, Phys. Rev. D **61** (2000) 025002.

[100] J. Garcia-Bellido and E. Ruiz Morales, Phys. Lett. B **536** (2002) 193.

[101] P. A. R. Ade *et al.* (BICEP2 Collaboration), arXiv:1403.3985 [astro-ph.CO]. P. A. R. Ade *et al.* (BICEP2 Collaboration), arXiv:1403.4302 [astro-ph.CO].

[102] E. Brezin and C. Itzykson, Phys. Rev. D **2** (1970) 1191.

[103] V. S. Popov, Sov. Phys. JETP **34** (1972) 709.

[104] Y. Kluger, J. M. Eisenberg, B. Svetitsky, F. Cooper and E. Mottola, Phys. Rev. D **45** (1992) 4659.

[105] S. M. Schmidt, D. Blaschke, G. Ropke, S. A. Smolyansky, A. V. Prozorkevich and V. D. Toneev, Int. J. Mod. Phys. E **7** (1998) 709.

[106] R. Alkofer, M. B. Hecht, C. D. Roberts, S. M. Schmidt and D. V. Vinnik, Phys. Rev. Lett. **87** (2001) 193902.

[107] D. B. Blaschke, A. V. Prozorkevich, C. D. Roberts, S. M. Schmidt and S. A. Smolyansky, Phys. Rev. Lett. **96** (2006) 140402.

[108] N. Tanji, Annals Phys. **324** (2009) 1691.

[109] F. Hebenstreit, R. Alkofer, G. V. Dunne and H. Gies, Phys. Rev. Lett. **102** (2009) 150404.

[110] G. V. Dunne and Q. -h. Wang, Phys. Rev. D **74** (2006) 065015.

[111] I. Bialynicki-Birula, P. Gornicki and J. Rafelski, Phys. Rev. D **44** (1991) 1825.

[112] F. Hebenstreit, R. Alkofer and H. Gies, Phys. Rev. D **82** (2010) 105026.

[113] S. R. Coleman, R. Jackiw and L. Susskind, Annals Phys. **93** (1975) 267.

[114] S. R. Coleman, Annals Phys. **101** (1976) 239.

[115] J. Ambjorn, T. Askgaard, H. Porter and M. E. Shaposhnikov, Nucl. Phys. B **353** (1991) 346.

[116] V. V. Skokov and P. Levai, Phys. Rev. D **78** (2008) 054004.

[117] F. Hebenstreit, A. Ilderton, M. Marklund and J. Zamanian, Phys. Rev. D **83** (2011) 065007.

[118] I. Bialynicki-Birula and L. Rudnicki, Phys. Rev. D **83** (2011) 065020.

[119] F. Hebenstreit, R. Alkofer and H. Gies, Phys. Rev. Lett. **107** (2011) 180403.

[120] F. Hebenstreit, A. Ilderton and M. Marklund, Phys. Rev. D **84** (2011) 125022.

[121] F. Peyrin and R. Prost, IEEE Trans. Acoust., Speech, Signal Processing **34** (1986) 858.

[122] F. Hebenstreit, *PhD thesis*, arXiv:1106.5965 [hep-ph].

[123] A. I. Nikishov, Nucl. Phys. B **21** (1970) 346.

[124] H. Gies and K. Klingmuller, Phys. Rev. D **72** (2005) 065001.

[125] Y.-Z. Chu, and T. Vachaspati, Phys. Rev. D **81** (2010) 085020.

[126] S. Iso and H. Murayama, Prog. Theor. Phys. **84** (1990) 142.

[127] A. Cucchieri and T. Mendes, Comput. Phys. Commun. **154** (2003) 1-48.

[128] N. Tanji and K. Itakura, Phys. Lett. B **713** (2012) 117-121; N. Tanji, Annals Phys. **325** (2010) 2018-2040.

[129] J. Berges and S. Roth, Nucl. Phys. B **847** (2011) 197-219.